

2014

## DEVELOPMENT OF CONFOCAL IMAGING TECHNIQUES FOR PROBING INTERFACIAL DYNAMICS IN MICROSCALE, GAS-LIQUID, TWO-PHASE FLOW

Joseph E. Hernandez  
*Michigan Technological University*

Follow this and additional works at: <https://digitalcommons.mtu.edu/etds>

 Part of the [Mechanical Engineering Commons](#)


Copyright 2014 Joseph E. Hernandez

---

### Recommended Citation

Hernandez, Joseph E., "DEVELOPMENT OF CONFOCAL IMAGING TECHNIQUES FOR PROBING INTERFACIAL DYNAMICS IN MICROSCALE, GAS-LIQUID, TWO-PHASE FLOW", Dissertation, Michigan Technological University, 2014.  
<https://digitalcommons.mtu.edu/etds/738>

Follow this and additional works at: <https://digitalcommons.mtu.edu/etds>

 Part of the [Mechanical Engineering Commons](#)

DEVELOPMENT OF CONFOCAL IMAGING TECHNIQUES FOR  
PROBING INTERFACIAL DYNAMICS IN MICROSCALE,  
GAS-LIQUID, TWO-PHASE FLOW

By

Joseph E. Hernandez

A DISSERTATION

Submitted in partial fulfillment of the requirements for the degree of

DOCTOR OF PHILOSOPHY

In Mechanical Engineering – Engineering Mechanics

MICHIGAN TECHNOLOGICAL UNIVERSITY

2014

Copyright © 2014 Joseph E. Hernandez



This dissertation has been approved in partial fulfillment of the requirements for the Degree of DOCTOR OF PHILOSOPHY in Mechanical Engineering – Engineering Mechanics.

Department of Mechanical Engineering – Engineering Mechanics

Advisor: *Dr. Jeffrey S. Allen*

Committee Member: *Dr. C.K. Choi*

Committee Member: *Dr. Kazuya Tajiri*

Committee Member: *Dr. Adrienne Minerick*

Department Chair: *Professor William W. Predebon*



To my loving family who has supported me during my Ph.D. candidacy. Thank you,  
I couldn't have done this without you.



# CONTENTS

<i>List of Figures</i> . . . . .	xiv
<i>List of Tables</i> . . . . .	xv
<i>Preface</i> . . . . .	xvii
<i>Acknowledgments</i> . . . . .	xix
<i>Abstract</i> . . . . .	xxi
1. <i>Introduction and Motivation</i> . . . . .	1
2. <i>Confocal Microscopy</i> . . . . .	5
2.1 Confocal Image Formation . . . . .	6
2.1.1 Optical Slice Thickness . . . . .	8
2.2 Common Confocal Microscopes . . . . .	10
3. <i>Confocal Characterization</i> . . . . .	13
3.1 Optical Path . . . . .	14
3.1.1 Confocal Optical Components . . . . .	15
3.1.1.1 Solid Stage Diode Lasers . . . . .	15
3.1.1.2 Aperture Plate . . . . .	17
3.1.1.3 Emission/Excitation Filtering . . . . .	17
3.1.1.4 Filter Wheel . . . . .	19
3.1.1.5 QuarterWaveplate . . . . .	19
3.1.1.6 Mirror Galvanometer . . . . .	20
3.2 Swept-Field Confocal Microscope Device Properties . . . . .	20
3.2.1 Objective Lens . . . . .	20
3.2.2 Field of View . . . . .	21
3.2.3 Measured Optical Slice Thickness . . . . .	23
3.2.4 Objective Offsets . . . . .	25
3.2.5 Chromatic Aberrations . . . . .	26



3.2.6	Spherical Aberration . . . . .	27
3.3	General Confocal Microscopy Research Setup . . . . .	31
3.3.1	Confocal Microscope Control . . . . .	32
3.3.2	Prior Proscan Stage . . . . .	34
3.3.2.1	Stage Movement . . . . .	34
3.3.2.2	Stage Scale . . . . .	35
3.3.2.3	Stage Speed . . . . .	36
3.3.3	Cameras . . . . .	38
3.3.3.1	Photron Ultima APX-RS Fastcam . . . . .	38
3.3.3.2	JAI . . . . .	38
3.3.4	Hardware Synchronization . . . . .	39
4.	<i>Measurement of Dynamic, Thin, Liquid Films in Microchannels Using Reflectance, Swept-Field Confocal Microscopy</i> . . . . .	41
4.1	Introduction . . . . .	41
4.1.1	Liquid Film Deposition in Capillary-Scale Channels . . . . .	42
4.1.2	Measuring Liquid Film Thickness in a Microchannel . . . . .	43
4.2	Reflectance Swept-Field Confocal (RSFC) Microscopy Measurements in Microchannels . . . . .	46
4.2.1	Segmented Flow Experiments . . . . .	47
4.2.2	Film Deposition Experiments . . . . .	48
4.2.3	Determining Interface Location . . . . .	48
4.2.4	Depth Correction . . . . .	49
4.2.5	Measurement Uncertainty . . . . .	53
4.3	Discussion . . . . .	58
4.4	Conclusion . . . . .	60
5.	<i>Reflectance, Swept-Field Confocal Particle Tracking Velocimetry Near a Moving Contact Line</i> . . . . .	61
5.1	Introduction . . . . .	61
5.2	Background . . . . .	63
5.2.1	Flow Visualization . . . . .	64
5.3	Experimental Setup . . . . .	71
5.3.1	Method of Particle Tracking . . . . .	72
5.4	Flow Fields at the Centerline . . . . .	74
5.5	Flow Fields at Three Focal Depths . . . . .	77
5.6	Combined Image Information . . . . .	80
5.7	Conclusions . . . . .	82

6. <i>Interfacial Morphology Measurement with Reflectance, Swept-Field Confocal Interferograms</i> . . . . .	83
6.1 Introduction . . . . .	83
6.2 Segmented Flow . . . . .	85
6.3 Sloped Interface . . . . .	90
6.4 Monochromatic Imaging of Droplet Evaporation . . . . .	94
6.4.1 Two-Color Droplet Evaporation . . . . .	97
6.5 Conclusion . . . . .	103
7. <i>Conclusions</i> . . . . .	105
<i>References</i> . . . . .	108
 <i>Appendices</i>	123
A. <i>Copyright Agreements</i> . . . . .	125
A.1 Prairie Technologies . . . . .	126
A.2 PIV11 . . . . .	128
A.3 Taylor1961 . . . . .	130
B. <i>Included MATLAB Code</i> . . . . .	133
B.1 Confocal Design . . . . .	133
B.2 Confocal Axial Resolution . . . . .	138
B.3 Confocal Axial Resolution - FWHM . . . . .	141
B.4 Liquid Film Thickness Detection . . . . .	159
B.5 Intensity Check . . . . .	183
B.6 RS-232 Focus Control . . . . .	186
B.7 Particle Tracking . . . . .	191
B.8 RS-232 PTV . . . . .	202



# LIST OF FIGURES

2.1	Image formation with and without the confocal aperture. Light passing through the confocal aperture is filtered, removing out-of-focus light from the beam path. . . . .	7
2.2	Depiction of camera sensor exposure for common, commercially available confocal microscopes . . . . .	11
3.1	(a) and (b) Light path of the swept-field confocal unit manufactured by Prairie-Technologies, Inc. Blue and green lines represent laser excitation (blue) and emission (green) following standard Stokes shift for fluorescence imaging. The blue box highlights the scanning mirror assembly and the red box highlights the interchangeable filter. Used with permission, agreement in Section A.1 . . . . .	14
3.2	Images of the Prairie Technologies, Inc. swept-field confocal setup. (a) Confocal unit with the Photron FASTCAM Ultima APX-RS attached. (b) Rack containing the laser housing and the controllers for the swept-field confocal and Prior Stage. . . . .	16
3.3	Photo (a) and schematic (b) of the aperture plate consisting on circular and slit apertures. The two sets of apertures are optically aligned for simultaneous, spatial filtering of excitation and emission light. . . . .	17
3.4	Beam path of a dichroic mirror and 50/50 beam splitter. . . . .	18
3.5	Linear polarizer blocks light which is oscillating perpendicular to the transmission polarization. . . . .	19
3.6	Sample images of wide field images (Port 4) and confocal images (Port 5) used to calculate field of view. Images are of an epi-illuminated Edmunds Cross Stage Micrometer, Part #: 58608. . . . .	23
3.7	Chromatic aberration occurs when shifting from the blue to the red laser. The positive number in the table represents movement of the objectives away from the sample (down) . . . . .	27
3.8	Transmitted light path transitioning from air to glass to air again. The refractive index change bends the light path. . . . .	28

3.9	A change in refractive index between the objective medium and test section creates a spherical aberration which must be corrected to accurately measure the test section thickness. . . . .	30
3.10	Schematic of the reflectance, swept-field confocal (RSFC) microscopy experimental setup. . . . .	33
3.11	(a) Schematic of stage with inner opening for experimental plates and (b) coordinate system for referencing stage movement. . . . .	34
4.1	Light returning from the liquid film requires correction from the radial channel shape ( $X$ - $Z$ ) and along the channel length ( $Y$ - $Z$ ). Corrections relate the apparent depth of the liquid film with the actual interface location. Cover slip, channel, and glycerol are refractive index matched. An average of the radial and lengthwise correction factors determines the interface location. . . . .	50
4.2	Normalized intensity profiles of the image intensity across the radius of the channel, taken at the center of the evaluation AOI. . . . .	56
4.3	Averaged image intensities measured across the channel wall and liquid film. Gaussian fits, combined with peak analysis, detected the wall and liquid film surface in this excessively noise intensity plot. The dashed lines represent the individual Gaussian curving fitting functions, and the solid line is the combination of the two fits. . . . .	57
4.4	Comparison of experimental film thickness measurements (square symbols) with Bretherton film thickness approximation (solid line), Equation 4.1. The gray band represents the confidence interval of 20% for the film thickness approximation. . . . .	59
4.5	Image of the reflective response from a dynamic liquid film with flow from right to left. The decrease in interference wavelength from left to right indicate an increasing film thickness and increasing interface curvature. . . . .	60
5.1	Image of gas-liquid interface of a liquid plug in a microchannel. The interface acts as a lens that bends the light away from the optical path creating the dark region near the meniscus. . . . .	62
5.2	Schematic of the microscale, gas-liquid, segmented, two-phase flow. Segmented flow is defined by separate phases, a bubble and liquid slug, which may or may not have a continuous liquid film (pictured). . . . .	63
5.3	Centerline images of a moving gas-liquid interface at different $Ca$ numbers. The gas-liquid interface distorts at $Ca=10^{-2}$ , determined by the increase in liquid film and blurred interface. Images are formed with transmitted light and an index matched test section. . . . .	65

5.4	Predicted flow profiles within the liquid phase of microscale, gas-liquid two-phase flow, $m$ is the square root of the Ca number. Originally published in Taylor [1], used with permission, agreement in Appendix A.3 . . . . .	66
5.5	Sample images depicting the difference in particle density between PIV and PTV measurement techniques . . . . .	68
5.6	Individual particle locations of the first frame (hollow particles) are statistically linked to particles in the second image(solid). Particle displacement should be less than the mean distance between particles to reduce the number of linking combinations. . . . .	70
5.7	A plug within a microchannel is under a constant flow rate condition when the stage is moved relative to a stationary plunger. . . . .	72
5.8	Confocal microscopy images particles with a finite optical slice thickness. Standard illumination is larger than the area-of-interest, increasing noise and decreasing velocity measurement accuracy. Horizontal lines represent depth that images were imaged. . . . .	73
5.9	Trace of a $4\ \mu\text{m}$ reflective particles in a $490\ \mu\text{m}$ round channel, under constant displacement advancing meniscus. The Ca number of the ethylene glycol is $4.5 \times 10^{-4}$ . The raw image has been cropped, filtered, and inverted for better particle visualization. Images are $490\ \mu\text{m}$ wide.	75
5.10	Trace of a $4\ \mu\text{m}$ reflective particles in a $490\ \mu\text{m}$ round channel, under constant displacement advancing meniscus. The Ca number of the ethylene glycol is $9.1 \times 10^{-5}$ . The raw image has been cropped, filtered, and inverted for better particle visualization. Images are $490\ \mu\text{m}$ wide	76
5.11	Flow fields measured at different optical slice depths (a) $75\ \mu\text{m}$ (b) $150\ \mu\text{m}$ (c) $225\ \mu\text{m}$ relative to the bottom channel surface. Glycerol plug within a $490\ \mu\text{m}$ diameter channel being withdrawn at $\text{Ca}=5.379 \times 10^{-3}$ .	79
5.12	Single image from the Figure 5.11a data set. A plug of glycerol with $4\ \mu\text{m}$ reflective particles near a moving meniscus imaged at $75\ \mu\text{m}$ relative to the channel wall. The image contains particle reflections in the liquid phase and interference patterns caused by the change in liquid film thickness. Interference patterns are formed near the transition from flat film to meniscus and near a cluster of trapped particles. . .	81
6.1	Simple schematic representing the three regions of an advancing gas-liquid interface; Meniscus, Transition and flat. Film thickness change between flat and meniscus was detected as interference patterns using the RSFC imaging technique. . . . .	86
6.2	Interference pattern captured at the transition between flat film and liquid meniscus. An intensity profile along the white line is presented in Figure 6.3 . . . . .	86

6.3	Image intensity across the length of the white line in Figure 6.2. Distances between peaks approximated the change in film thickness from the flat film to the meniscus. . . . .	87
6.4	Change in film thickness from the flat film to the transition region in segmented flow. . . . .	89
6.5	Light paths for interference patterns created by a sloped interface. Interference patterns were formed from light reflections at the Glass-Air and Air-Glass interfaces. The slope of the top coverslip is controlled by the thickness and location of the shim. . . . .	91
6.6	Interference patterns formed by a sloped Air-Glass interface using the experimental setup depicted in Figure 6.5. Slopes were created with shims having thicknesses of (a) Clear 190 $\mu\text{m}$ and (b) Green 80 $\mu\text{m}$ . Images were formed using the RSFC imaging technique, 2 $\times$ objective NA 0.06, and 643 nm laser. The slopes of the lines are 9E-3 and 7E-3 $\mu\text{m}/\mu\text{m}$ for the Clear and Green shims, respectively. . . . .	92
6.7	Film thickness measurement of the distance between a flat and sloped cover slip depicted in Figure 6.5. Coverslip slopes are related to the thickness of the shim. Red circles represent a Clear 190 $\mu\text{m}$ shim and a Green boxes represent Green 80 $\mu\text{m}$ shim . . . . .	93
6.8	Droplet images representing different stages of evaporation. Images were taken with a 2 $\times$ , 0.06NA objective lens and 643 nm laser. Drop diameters are approximately 2.8 mm. . . . .	94
6.9	(a) Interference pattern formed in an evaporating droplet of distilled water on a borosilicate coverslip. (b) Pixel intensity profile across the centerline of the droplet. . . . .	96
6.10	Shape of the evaporating droplet. . . . .	97
6.11	Sets represent images taken 1 frame apart, at a frame rate of 1 frame per second, total exposure of 2 fps. Droplets were distilled water on a borosilicate glass slide, imaged with a 20X objective and RSFC microscopy. . . . .	99
6.12	Intensity profile across a line segment perpendicular to the interference bands. . . . .	100
6.13	(a) Film thickness calculations for the red images in Figure 6.11 (b) Comparison of film thicknesses for third set blue and red images . . .	102

## LIST OF TABLES

3.1	Basic properties of objectives used for confocal imaging. . . . .	21
3.2	Field of views:Port 2-Widefield, Port 5-Confocal, and Port 4-Widefield. Scale (px/ $\mu\text{m}$ ), Width/Height ( $\mu\text{m}$ ) . . . . .	22
3.3	Properties of the objectives used for confocal imaging. The optical slices assume an imaging medium of Air . . . . .	24
3.4	Comparison of theoretical and experimentally measured optical slice thicknesses using slit apertures with blue(488 nm) and red (643 nm) illumination. . . . .	25
3.5	Table of physical optical offsets for three objectives, 10x, 20x, and 40x. The shifts are relative to the 10 $\times$ objective. For the z-axis the negative motion implies a movement of the objective closer to the stage, (up).	26
3.6	Table of the stage velocities found for different sms settings of the stage for the X and Y directions . Stage settings are comp 0 and ss of 25 .	37





# PREFACE

This dissertation consists of material prepared independently by Joseph Hernandez and collaboratively with other researchers. All written material was prepared under the guidance of Dr. Jeffrey Allen. Chapters 1, 2, 3, 5 and 7 are the original work of Joseph Hernandez. Portions of Chapter 5 were previously published and presented at PIV 11. Content was produced by Joseph Hernandez and Dr. Jeffrey Allen and used with permission, Appendix A.2. Chapter 4 was written in collaboration with David Deisenroth and Dr. Jeffrey Allen. Joseph Hernandez prepared the majority of the Chapter 4, designed and developed the experimental procedure and performed the data analysis. David Deisenroth collected experimental data, provided additional material and edited rough drafts. Dr. Jeffrey Allen advised the project, provided written material, and edited the manuscript. Images of interference patterns for segmented flow presented in Chapter 6 were collected by David Deisenroth and Joseph Hernandez, evaporating droplets were captured during experimental investigations with Joseph Hernandez, Dong Hwan Shin, and Dr. C.K. Choi during. Data analysis and discussion in Chapter 6 are original work of Joseph Hernandez.



## ACKNOWLEDGMENTS

I am forever grateful for the support given to me by my loving wife, Adrienne, and our wonderful children, Kylie, Mason, Cullen and Easton. Thank you for your continued patience and understanding. I would like to thank my parents for the years of encouragement and love. Cyberia Cafe, for letting me buy a coffee and spend all day writing.

I'd like to thank my advisor Dr. Jeffrey Allen for guiding and most importantly supporting me throughout my graduate education. I would like to acknowledge the researchers, past and present, in the Microfluidics and Interfacial Transport Laboratory, Russel Stacy, Ezequiel Medici, David Deisenroth, Vinaykumar Konduru, Aneet Narendranath, Stephen Stacy, Mark Nettel, and Chelsey Smith. We had fun. I would like to thank the staff of the Mechanical Engineering - Engineering Mechanics Department at Michigan Tech Graduate School, especially Marty Toth and the wonderful office staff.

This research was financially supported by the U.S. National Science Foundation (Grant No. CBET-078049), the King-Chavez-Parks Future Faculty Fellowship and Michigan Technological University's Department of Mechanical Engineering Alumni Fellowship. I would also like to acknowledge Prairie Technologies, Inc. for providing technical assistance.



# ABSTRACT

DEVELOPMENT OF CONFOCAL IMAGING TECHNIQUES FOR PROBING INTERFACIAL DYNAMICS IN MICROSCALE, GAS-LIQUID, TWO-PHASE FLOW

Joseph E. Hernandez

Michigan Technological University, 2014

Advisor: *Dr. Jeffrey S. Allen*

Micro-scale, two-phase flow is found in a variety of devices such as Lab-on-a-chip, bio-chips, micro-heat exchangers, and fuel cells. Knowledge of the fluid behavior near the dynamic gas-liquid interface is required for developing accurate predictive models. Light is distorted near a curved gas-liquid interface preventing accurate measurement of interfacial shape and internal liquid velocities. This research focused on the development of experimental methods designed to isolate and probe dynamic liquid films and measure velocity fields near a moving gas-liquid interface. A high-speed, reflectance, swept-field confocal (RSFC) imaging system was developed for imaging near curved surfaces.

Experimental studies of dynamic gas-liquid interface of micro-scale, two-phase flow were conducted in three phases. Dynamic liquid film thicknesses of segmented, two-

phase flow were measured using the RSFC and compared to a classic film thickness deposition model. Flow fields near a steadily moving meniscus were measured using RSFC and particle tracking velocimetry. The RSFC provided high speed imaging near the menisci without distortion caused the gas-liquid interface. Finally, interfacial morphology for internal two-phase flow and droplet evaporation were measured using interferograms produced by the RSFC imaging technique. Each technique can be used independently or simultaneously when .

# 1. INTRODUCTION AND MOTIVATION

Microscale, gas-liquid, two-phase flow occurs over a variety of flow morphologies. These flow morphologies, classified as regimes, categorize two-phase flow based on physical appearance of the phases. In this work flow regimes will be categorized using the definitions define by Hassan et al. [2]; surface tension and inertia dominated. Surface tension dominated regimes:

1. *Bubbly* : Liquid encompasses the bulk of the channel with gas bubbles having diameters smaller than the channel's.
2. *Intermittent* : Plugs and elongated bubbles alternate in the channel, a thin liquid film may be present. The length of the bubble/plug is dependent on the flow rates. This regime is typically referred to as slug/plug flow, bubble train, and segmented.

Inertia dominated:

1. *Dispersed* : Unstable flow regime containing elements of annular and intermittent flow. Plugs/slugs may collapse into the film or the film may coalesce in plug/slugs. High gas flow rates may shear liquid out of the film, which form droplets and travel in the gas phase. This regime includes the wispy annular and churn flow regimes.



2. *Annular* : An annular film of liquid is present on the walls surrounding a gas core, some instabilities may be present on the film surface.

Similar regimes exist in microscale liquid-liquid flows.[3]

Interactions between phases of macroscale two-phase flow are primarily controlled by inertial effects, characterized by large Reynolds and Weber numbers. Surface tension and viscosity have a minimal role in the response of the deformable gas-liquid interface and bulk liquid motion. Local effects, such as instabilities in the liquid film, are neglected in macroscale flow because the size of instability is saturated by the bulk fluid motion.

Phases interact differently at the microscale. Surface tension and viscous forces are closer in magnitude to inertial forces. A layer of liquid deposited on a channel wall in a micro-channel can dictate the entire flow behavior, including transitions to the different flow regimes.

Current methods of predicting microscale, two-phase flow have been unsuccessful. Traditional methods for predicting macroscale two-phase flow, phase diagrams, Lockhart-Martinelli parameters, and predictions based on pressure differentials, do not scale appropriately. [4] Local behavior, which is an integral part of microscale, flow morphology, is not captured with bulk property measurements. Dissipation events located between measurement points increase measured pressure differentials and increase the use of phase diagrams. Events that occur up or down stream of the current location affect the behavior of the microscale two-phase flow.

Morphological effects of the meniscus and liquid film in microscale, segmented gas-liquid two-phase flow have a strong influence on the internal flow behavior of the liquid phase. For examples, surface tension driven pressure gradients can induce

secondary flows within the liquid phase of the two-phase flow. This increases the complexity of modeling the flow profiles near the deformable gas-liquid interface. Motivated to better understand the complex fluid physics of microscale, two-phase flow, this research project focused on the development of experimental measurement techniques to locally measure

1. the thickness and response of dynamic thin liquid films
2. flow fields near a steadily moving meniscus

A reflectance, swept-field confocal imaging technique was developed for imaging dynamic gas-liquid interfaces and reflecting particles near a moving meniscus. Confocal microscopy improves imaging resolution and contrast when applied to microscale, two-phase flow. Optical sections tend to be at least an order of magnitude less than the size of the capillary scale test section. Thin optical slices make it possible to accurately detect reflections from gas-liquid films, Chapter 4. Measured film thicknesses are compared to a classic film thickness approximation. Signal to noise ratios for particle detection is improved by spatially filtering light originating from out-of-focus particles. Confocal particle tracking velocimetry (CPTV) results near a steadily moving meniscus are presented in Chapter 5. Images of the gas-liquid interface contain interference patterns which, not fully analyzed in this work, provide information on the curvature of the liquid surface, Chapter 6.



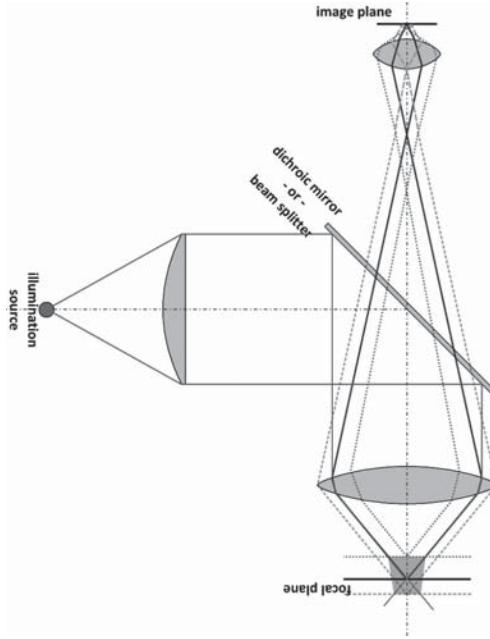
## 2. CONFOCAL MICROSCOPY

Confocal microscopy was developed in 1955 by Dr. Marvin Minsky, officially patented in 1957, to image the connections between brain cells in three dimensions. [5, 6] Dr. Minsky discovered that a “pinhole” at the focal point, near the imaging plane, would block out-of-focus light, increasing the resolution of the imaging device. The pinhole aperture is the primary optical principle of the confocal microscope. Differing from today’s commercially available confocal microscopes, Dr. Minsky’s version scanned the sample by physically moving the stage laterally and vertically, used a white light source and displayed images on a radar screen, a raster style display similar to an oscilloscope. A major disadvantage of the original version was the inability to permanently expose imaging media. Without the production of permanent photographs, the confocal was not widely adopted, even with the major improvements to imaging resolution. Dr. Minsky has acknowledged that incorporating photography would have greatly increased the adoption of the confocal microscope, “In retrospect it occurs to me that this concern for real-time speed may have been what delayed the use of this scheme for almost thirty years.” [6] Thirty years later, a comparison of the contrast and resolution improvements with confocal microscopy over standard wide-field imaging solidified the confocal microscope as an invaluable imaging tool for biological research.[7, 8]

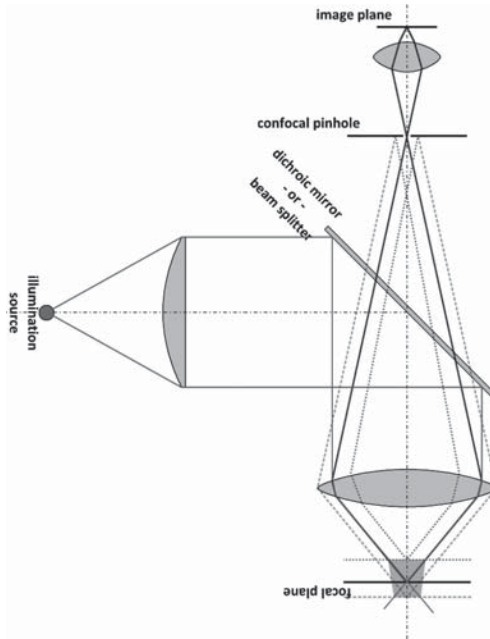
Researchers have made major advancements to confocal microscopy since the first demonstration of one in 1955.[9] Stage scanning replaced sample scanning, which has led to increase in imaging speed and sample location accuracy.[10, 11] High numerical aperture objectives increased the resolution of the confocal microscope close to the maximum Abbe diffraction limit.[12] Image capture using photographic and videography techniques provide permanent records of the imaged sample.[13]. Exposing photographic material also removes the requirement to match scanning rates with external displays, thus, increasing the versatility of the confocal microscope. A more complete description of confocal development is found in “Handbook of Biological Confocal Microscopy.”[14]

## 2.1 Confocal Image Formation

Figure 2.1 illustrates the difference between standard wide-field (2.1a) and confocal imaging (2.1b). Following a standard microscope light path, light originates from the illumination source traveling through the internal optics (simplified for discussion) until it reaches a dichroic mirror or beam splitter. Light is reflected to the objective lens assembly and focused onto the sample. Light returns from the sample, passing through the dichroic mirror and focused onto the image plane. For confocal microscopy, an aperture is placed at the focal point before the formation of the image plane. This aperture physically blocks the out-of-focus light, seen as the dashed and dotted lines in the figures. The resulting confocal image is referred to as an “optical slice” due to the absence of the fore/background information.



(a) Light path of the standard wide field microscope



(b) Light path of a simple confocal microscope

**Figure 2.1.** Image formation with and without the confocal aperture. Light passing through the confocal aperture is filtered, removing out-of-focus light from the beam path.

### 2.1.1 Optical Slice Thickness

A confocal microscope is chosen over standard widefield imaging techniques due to an increase in contrast and resolution produced by filtering out-of-focus light. The performance of the confocal microscope is characterized by the optical slice thickness, often referred to as axial resolution. Axial resolution is controlled by the size of the confocal aperture, which is ideally a function of the optical properties of the microscope and objective. Modern microscopes are telecentric, designed to maintain constant magnification throughout the beam path.[15] Therefore, the objective, which controls magnification, is the primary factor in determining the imaging properties of a confocal microscope.

Resolution of a confocal microscope is defined by the radius of the Airy disk, the center bright point of the Airy pattern. An Airy pattern is formed as light diffracts through a circular aperture, producing a bright center spot followed alternating dark and bright bands. The radius of an Airy disk is approximated by the Abbe equation, defined as the distance from the center bright spot to the center of the first dark ring.[16]

$$R_{Airy} = 0.61 \frac{\lambda}{NA} \quad (2.1)$$

The size of the Airy disk is dependent on the wavelength of light,  $\lambda$ , and numerical aperture, NA, of the objective. The smallest Airy disk is formed with short wavelength light and high NA objectives. From a practical standpoint, the smallest Airy disk for visible light is achieved with 400 nm (Violet) light, and an immersion objective lens with a NA of 1.49, generating an Airy disk with a radius of 164 nm.

Lateral resolution of a microscope is a function of the Airy disk. Rayleigh resolution criteria defines lateral resolution as the distance that two equally bright points

are still discernible, which is the radius of an Airy disk. Airy disk or lateral resolution is simplified to  $d = .5\lambda/\text{NA}$ . Using this definition, the maximum resolution for visible light is 134 nm, a slight improvement over the Abbe definition of an Airy disk. Actual lateral resolution is dependent on the optical path of the confocal microscope, imaging device and response of the sample.

Confocal axial resolution is dependent on the point spread function (PSF) of the Airy disk. The PSF is the three dimensional response of a point source in the imaging plane. Axial resolution is defined by the full width half maximum (FWHM) of the PSF. For small confocal apertures, 25% or less of the Airy disk, the axial resolution is equivalent to the optical slice thickness

$$d_{axial} = K \frac{\lambda}{n \left[ 1 - \sqrt{1 - \left(\frac{\text{NA}}{n}\right)^2} \right]}, \quad (2.2)$$

where K is 0.95 and 0.67 for a slit and circular aperture, respectively.[16, 17] The coefficient K demonstrates the effect of geometry on the optical slice thickness. A slit, with a value of 0.95, increases the optical slice thickness by 41.8%. Depending on the applications, a thicker optical slice would offer an increase frame rate and improved light sensitivity.

Confocal optical slice thicknesses can be measured using one of two standard techniques. Fluorescence bead imaging measures the intensity of single fluorescence bead mounted to a glass cover slip. A reflectance mirror test measures the intensity of reflected light of a first surface mirror. [18] The FWHM of the axial intensity profile determines the thickness of the optical slice. Optical slice thicknesses for the reflectance, swept-field confocal microscope were measured using the mirror test, the



results are discussed in Chapter 3

Apertures are chosen based on objective characteristics and lighting requirements. The optimal diameter for a circular aperture, defined as 1 Airy disk, is

$$D_{opt} = .5 \frac{\lambda M}{NA} \quad (2.3)$$

where  $\lambda$  is the wavelength of light,  $M$  and  $NA$  are the magnification factor and numerical aperture of the objective lens, respectively.[16] Equation 2.3 is related to the Rayleigh resolution equation but includes the affects of the objective lens magnification. Objective lens  $NA$  and magnification are loosely coupled, with one property increasing when the other does. This produces a competition between properties. For example, using a laser of 488 nm and the objectives used in this research,  $10\times .25 NA$ ,  $20\times 0.45 NA$ ,  $40\times 0.60 NA$  the optimal diameters are,  $9.8 \mu\text{m}$ ,  $10.8 \mu\text{m}$ , and  $16.3 \mu\text{m}$ , respectively. A higher magnification lens, such as a  $100X 1.49 NA$  total internal reflection fluorescence (TIRF) lens, would have an optimal diameter of  $16.4 \mu\text{m}$ . Actual confocal microscopes have additional magnification optics inline, which introduces a device specific multiplier to the calculation.

## 2.2 Common Confocal Microscopes

Early improvements to confocal microscopy, such as sample scanning and laser illumination, yielded the Confocal Laser Scanning Microscope (CLSM) or Laser Scan Confocal Microscope (LSCM).[7–9, 12, 19] CLSM uses a single point source for illumination, created by a circular aperture diffraction, to expose the sample. Emitted light is spatially filtered using an equivalent circular aperture. CLSM images are

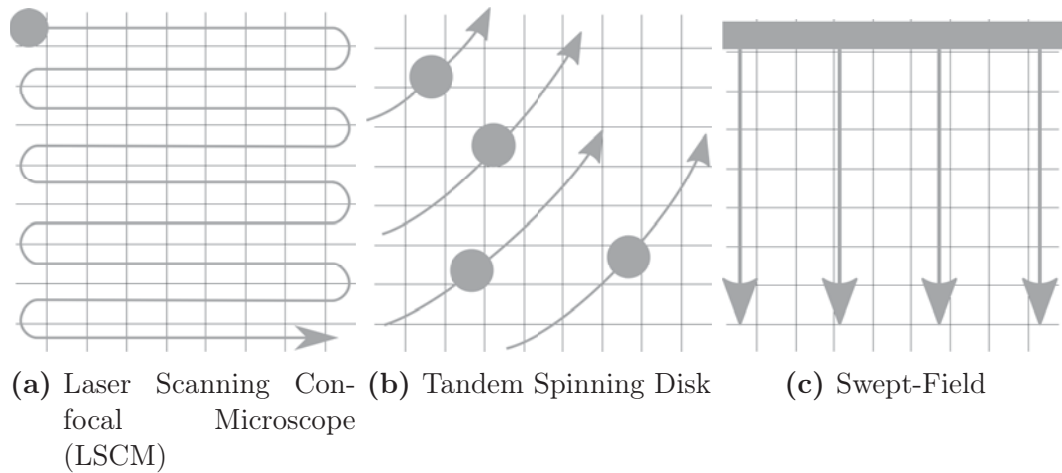


**Figure 2.2.** Depiction of camera sensor exposure for common, commercially available confocal microscopes

formed by raster scanning the point source over the sample; Figure 2.2a depicts the formation of the image. Image capture frame rates are on the order of a second due to the raster scanning. Increased frame rates are achieved by dividing the beam, and scanning the sample with multiple points. The CLSM is the most widely available confocal microscope and is suitable for biological studies.[9] A variable aperture can accommodate a large range of objectives, precisely matching the opening to the ideal imaging performance.

A tandem spinning disk microscope uses platters with holes, referred to as a Nipkow disk, Farrfor improved imaging speeds.[20, 21] Excitation light is passed through the confocal apertures on the spinning platters, the fluorescent light from the object is returned through the same holes where a dichroic mirror separates the two wavelengths. Images are formed by striping multiple holes across the camera sensor, depicted in Figure 2.2b. Two major versions of the tandem spinning disks are currently commercially available. A basic version has two disks in parallel. Light is focused on multiple holes, spatially filtered to form multiple point sources for il-

lumination. A majority of light is physically blocked and never reaches the sample producing poor illumination. An improved tandem spinning disk microscope integrates microlenses into the disks. Light is still focused onto multiple lens but a much larger percentage of light makes it to the sample.[22] Tandem spinning disk confocal microscopes are designed with only single circular aperture size. This requires the matching of objective NA for the optimal imaging performance. This is a severe restriction because lens manufacturers offer limited combinations of magnification and NA.

A swept-field confocal microscope uses a slit for the confocal aperture.[10] Using a slit increases the scanning speed over the traditional CLSM by scanning the sample in only direction instead of both x and y. The confocal unit which is used in this research is designed with four different slit aperture sizes and three arrays of circular apertures. Multiple apertures provide flexibility for balancing the confocal slice thickness with imaging performance. This is an improvement over tandem spinning disk confocal microscopes which are designed with a single pinhole size. As discussed above, a slit aperture blocks less light than a circular aperture, which decreases the confocality of the system. The optical slice thickness is increased by approximately 42% when using a slit instead of a circular aperture. [18] Increases in optical slice thickness is offset by the ability to scan at higher frame rates and increase in light sensitivity a requirement for high speed imaging.

A Prairie Technologies, Inc. swept-field confocal microscope was chosen for imaging high-speed gas-liquid, two-phase flow. Faster scan rates and multiple apertures provided the greatest balance between confocality and imaging speeds. Chapter 3 discusses the characteristics swept-field confocal microscope.

### 3. CONFOCAL CHARACTERIZATION

A swept-field confocal (SFC) microscope from Prairie-Technologies\* was chosen for visualization experiments designed to probe the flow fields and interface dynamics of gas-liquid, microscale two-phase flow, see Chapter 1. The SFC met or exceeded the selection criteria when compared with other commercially available confocal microscopes. Selection criteria included the system's overall cost, availability, scanning rate, light sensitivity, imaging flexibility, and customer support. Prairie Technologies, Inc. worked within design parameters to produce a confocal microscope that has the potential to scan at rates of up to 2000 FPS and had considerably more light sensitivity when compared with confocal microscopes with similar scanning speeds. As part of the purchasing agreement, Prairie Technologies, Inc. produced an additional removable light filter module made with a 50/50 beam splitter. The standard filter module is a dichroic mirror, used primarily for fluorescent imaging. Since the mirror module is not part of the internal optics of SFC, the confocal unit is easily converted between fluorescence and reflectance imaging by substituting. In this work, the confocal microscope is referenced as the reflectance, swept-field confocal (RSFC) microscope when using the 50/50 beam splitter.

---

\* <http://prairie-technologies.com/products/confocal/sfc.html>

### 3.1 Optical Path

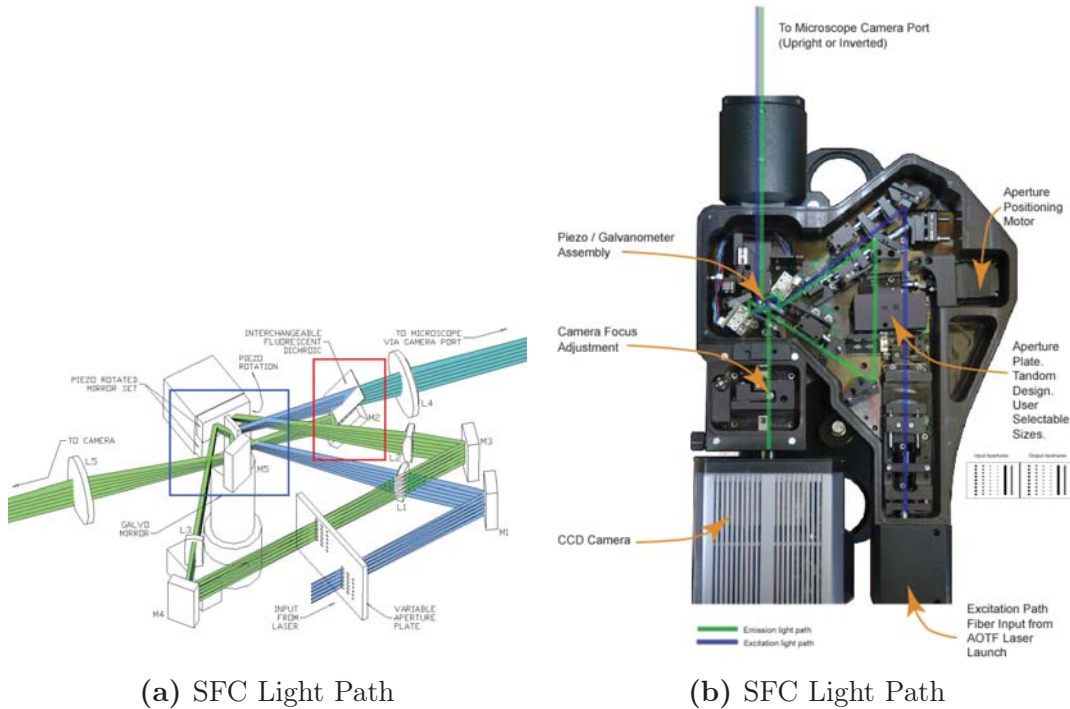


**Figure 3.1.** (a) and (b) Light path of the swept-field confocal unit manufactured by Pairie-Technologies, Inc. Blue and green lines represent laser excitation (blue) and emission (green) following standard Stokes shift for fluorescence imaging. The blue box highlights the scanning mirror assembly and the red box highlights the interchangeable filter. Used with permission, agreement in Section A.1

Images are formed with the swept-field confocal microscope following the standard illumination/emission of traditional confocal microscopy. The swept-field confocal light path is illustrated in Figure 3.2a. Excitation and emission light paths are referenced as blue and green, respectively. Light path colors represent a standard Stoke’s shift of fluorescence, short wave excitation stimulate the fluorescence molecule which emit a photon of a longer wavelength. This color scheme is assumes a standard stokes shift which occurs from exciting a green fluorescing particle with blue light. An ac-

tual confocal microscope with light paths superimposed on the image is presented in Figure 3.1b. Excitation light (Blue), provided by the Aurora - Solid State Diode Laser Launch, enters the confocal microscope through a fiber optic cable, as seen in the bottom right of Figure 3.2b. The light is focused onto the slit/hole aperture plate, then redirected onto the galvanometric mirror (Blue Box), Figure 3.2a. Light reflected from the galvanometric mirror travels through the dichroic mirror/beam splitter (Red Box) into the left port of the inverted microscope, through the objective, and focused onto the sample. Emission light (Green) returning from the objective lens is redirected by the mirror galvanometer back to the slit/hole aperture plate and through a wavelength filter onto the image plane. The filter wheel contains a band pass filter, which matches the frequencies of the dichroic mirror, a polarizer, and additional blank positions. In addition to the filter wheel, a quarter wave plate is installed in the microscope filter turret for modifying the polarization of the excitation/emission light. Images are formed by scanning the excitation/emission light with mirror galvanometer, without the mirror deflection the image would be a solid laser light comparable in size with the confocal aperture opening.

### **3.1.1 Confocal Optical Components**

#### *3.1.1.1 Solid Stage Diode Lasers*

Two diode pumped solid state (DPSS) lasers, 488nm (blue) and 643 nm (red) are installed in a Prairie Technologies, Inc, Aurora - Solid State Diode Laser Launch.\* A diode pumped solid state (DPSS) laser emits monochromatic light produced by exciting a solid crystalline structure with a diode. Generated laser light may require

---

\* <http://www.prairie-technologies.com/products/laser/Aurora.html>

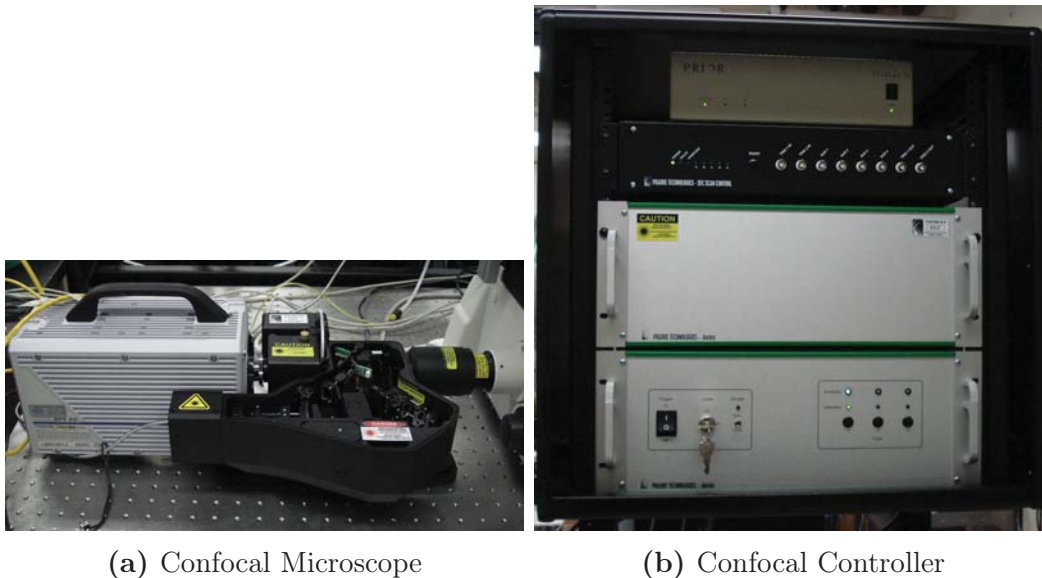


**Figure 3.2.** Images of the Prairie Technologies, Inc. swept-field confocal setup. (a) Confocal unit with the Photron FASTCAM Ultima APX-RS attached. (b) Rack containing the laser housing and the controllers for the swept-field confocal and Prior Stage.

frequency doubling to produce shorter wavelength line. The blue and red lasers were chosen because they are close the maximum visible light frequencies in the visible spectrum. A maximum output power of approximately 15 mw is available at the objective. A combination of filters, aperture size and additional inline optics will reduce the excitation laser power. Laser light intensity is controlled using software provided by Prairie Technologies, Inc. The output is linearly adjusted between 0-100 to provide the optimal amount of sample excitation. Equation ?? demonstrates that a smaller confocal optical slice is created with shorter wavelength light. In general for this research, the blue (488 nm) laser was preferred.

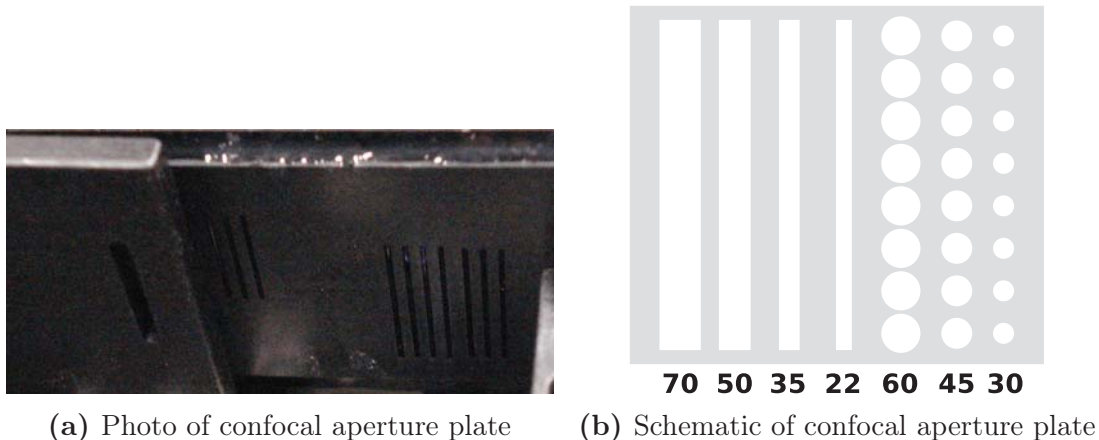


**Figure 3.3.** Photo (a) and schematic (b) of the aperture plate consisting on circular and slit apertures. The two sets of apertures are optically aligned for simultaneous, spatial filtering of excitation and emission light.

### 3.1.1.2 Aperture Plate

The RSFC microscope is equipped with an aperture plate having two identical sets of three circular and four slit apertures. Confocal apertures are optically aligned to create identical excitation and emission point sources. Holes are 30, 45, and 60  $\mu\text{m}$  in diameter aligned in column with a series of 32 holes. Light is divided into 32 individual point sources similar to a multi-point source CLSM. Slit apertures have widths of 22, 35, 50, 70  $\mu\text{m}$ , which produces a single line of slit diffraction. Ideal aperture dimensions are calculated using the RSFC control software and objective properties. Calculated diameters are not equivalent to the approximation of Equation 2.3 due to inline magnification factors which are know provided by the manufacture.

### 3.1.1.3 Emission/Excitation Filtering

Excitation and emission light in the swept-field confocal is filtered using either a dichroic mirror or 50/50 beam splitter. A dichroic mirror is tuned to 488 and 643



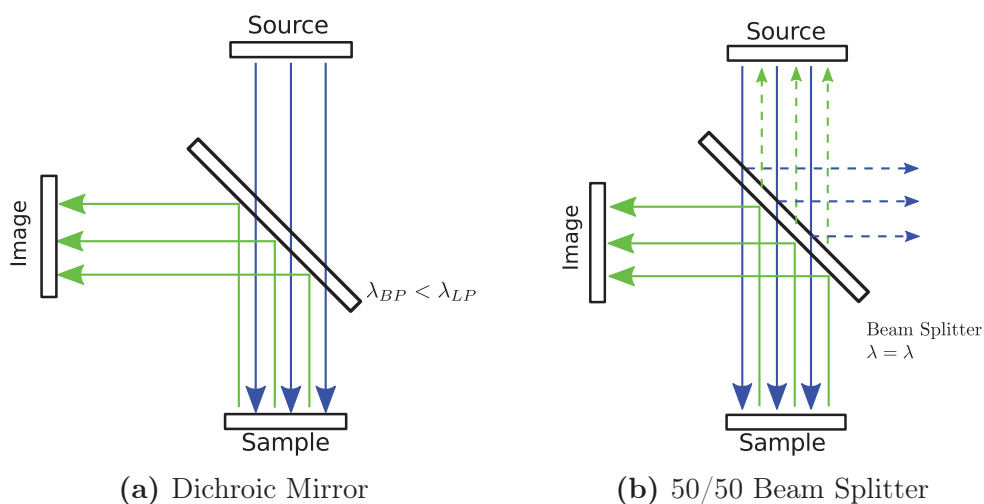


**Figure 3.4.** Beam path of a dichroic mirror and 50/50 beam splitter.

nm wavelengths for fluorescence imaging. The dichroic filter selectively reflects and transmits light based on wavelength. For example, 488 nm (blue) light is transmitted while longer wavelength light, 510 nm (green), is reflected. Figure 3.4a represents the light path of blue excitation/green emission of a standard green fluorescence process. A dichroic mirror is essential for fluorescence imaging, removing the excitation light from the beam path.

A 50/50 beam splitter is used for reflectance imaging because the excitation and emissions wavelengths are the same would result in 100% loss of emission light. A beam splitter is a half-silvered mirror which reflects and transmits half of the available light. The mirror allows 50% of the excitation light to reach the sample and 25% of the emission light for the image plane. Fluorescence emission intensity is limited by the fluorescence molecule, and with a finite level available for imaging. Reflectance image intensity is limited only by the maximum power of the excitation source and power rating of the optical components.

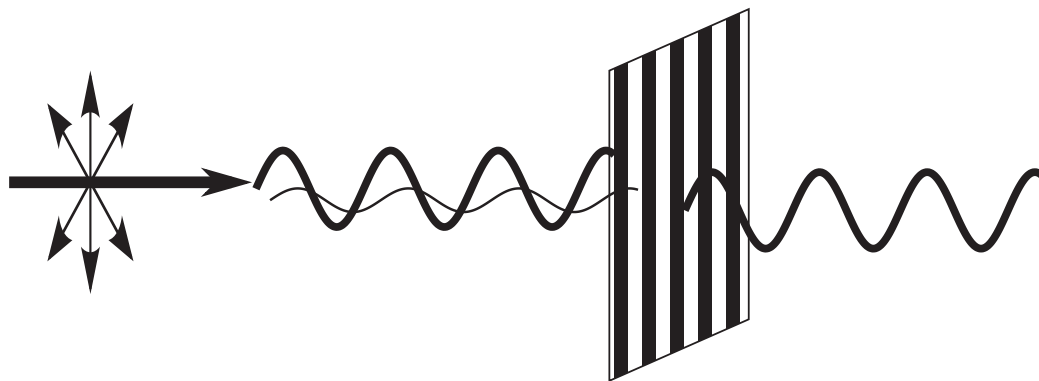


**Figure 3.5.** Linear polarizer blocks light which is oscillating perpendicular to the transmission polarization.

#### *3.1.1.4 Filter Wheel*

The filter wheel of the swept-field confocal has a linear polarizer and a multiple wavelength band pass barrier filter. A linear polarizer filters light by physically blocking light which oscillates in the perpendicular direction not transmittable by the filter. A schematic of the a simple linear polarizer is presented in Figure 3.5. The polarizing filter is optional when imaging in reflectance mode and is used to enhance the contrast of an image by removing background reflection or reducing laser intensity. The bulk of imaging reflected light is done without a filter to increase the signal reaching the camera sensor. The band pass filter is used only for fluorescence imaging and filters light which that is not within narrow gap of wavelengths.

#### *3.1.1.5 QuarterWaveplate*

In addition to the linear polarizing filter, a quarter wave plate is used to reduce internal reflections within the confocal assembly. Internal reflections, caused by light interacting with non-optical structures, produce spurious signals which interfere with

image capture. A quarter wave plate converts the polarization of light from linear to circular polarization. Emission light is converted back from circular to linear polarization. Any stray light having a different polarization is filtered by the linear polarizer.

#### *3.1.1.6 Mirror Galvanometer*

A galvanometer rotates a first surface mirror for scanning the sample. The galvanometer was originally designed to measure electric current. The magnitude of electric field is proportional to the amperage in the detection coils. Confocal sample scanning deflects a mirror mounted to the galvanometer by applying a known amperage. In the SFC, linear and sinusoidal deflection patterns create two different imaging modes. The flatness of the image plane is a function of the deflection pattern. For high speed imaging, a sinusoidal deflection pattern is used to increase the scanning rate. Illumination uniformity near the frame edges is sacrificed.

## **3.2 Swept-Field Confocal Microscope Device Properties**

### **3.2.1 Objective Lens**

Three microscope objective lenses were selected for confocal imaging; Nikon 10 $\times$ , 20 $\times$  and 40 $\times$  long working distance objectives (LWD). Table 3.3 contains the magnification, numerical aperture (NA) and working distance (WD) for the three objectives. Long working distance (LWD) objectives decrease limitations on test section thickness. Lower magnification objectives were chosen for larger field of views and the

objectives are designed for air. Longer working distances translate into smaller NAs compared to standard air immersion objectives. Lower objective lens NA values increase the optical slice thickness but the ability to image thicker test sections the thicker optical slices.

Mag.	NA	WD(mm)
10×	0.25	10.5
20×	0.45	8.2-6.9
40×	0.60	3.6-2.8

**Table 3.1.** Basic properties of objectives used for confocal imaging.

### 3.2.2 Field of View

Field of views of the imaging ports for the TE-2000 microscope were measured. The right port is used for C-mount cameras and the front port is used for F-mount cameras. Field of views for the front port are measured using a Nikon D1X. FOV measurements for the Left (confocal) and right port (widefield) use a Pulnix TM1325-CL C-mount camera. Measurements are taken using a Edmunds Cross Stage Micrometer (Part #: 58608). Field of view values in Table 3.2 are referenced to a camera with the same view as the eyepieces. Internal optics rotate the images in each port. The right port has a 90° clockwise rotation and the left port is rotated 90° counter clockwise. Images taken with the front port are mirrored along the X-axis. FOV measurements for the three ports are consistent in magnitude. The aspect ratio for the Nikon D1X imaging chip does not match C-mount camera and the width and heights differ. This difference only needs to be accounted for when comparing images taken with the Pulnix cameras and the D1X. FOVs for ports 2 and 5 are averaged between the confocal and widefield measurements. Reflection intensity variations for confocal

images were averaged using a range of laser excitation. Distances were measured between the center of the graduations for the stage micrometer.

Mag	Ports 2 & 5			Port 4		
	Scale	Width	Height	Scale	Width	Height
10X	1.5536	895.98	669.41	3.2358	928.5	604.5
20X	3.0530	453.57	338.87	6.3384	473.9	308.6
40X	6.3000	220.95	165.08	12.6001	238.4	155.2

**Table 3.2.** Field of views:Port 2-Widefield, Port 5-Confocal, and Port 4-Widefield. Scale (px/ $\mu\text{m}$ ), Width/Height ( $\mu\text{m}$ )

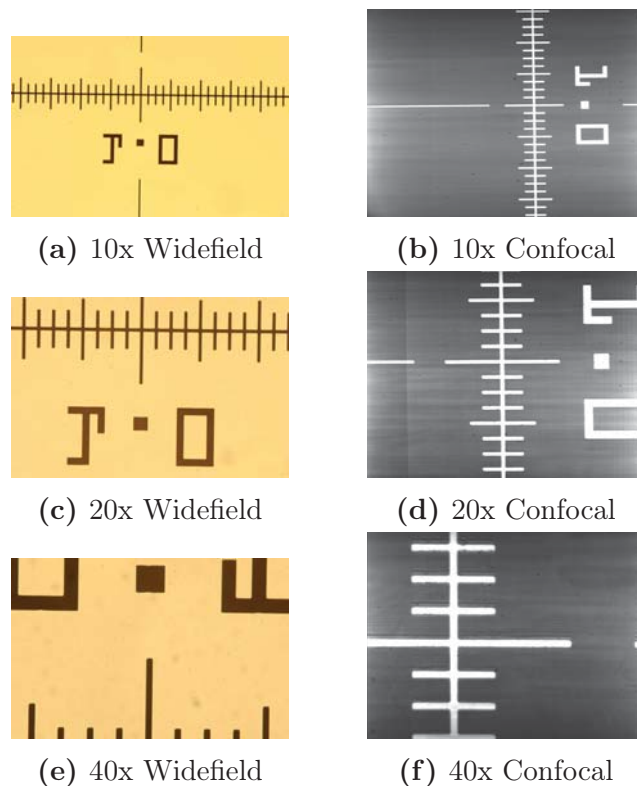


**Figure 3.6.** Sample images of wide field images (Port 4) and confocal images (Port 5) used to calculate field of view. Images are of an epi-illuminated Edmunds Cross Stage Micrometer, Part #: 58608.

### 3.2.3 Measured Optical Slice Thickness

Optical slice thickness is related to the size of the confocal aperture or “pinhole diameter” (PD), objective lens numerical aperture, and wavelength of the excitation light. This prediction is valid for only the light exciting the objective and does not account for optical distortions created by additional optics within the microscope and confocal lens assembly. Optical slice thicknesses were measured using a standard mirror reflection test.[18, 23]. Intensity profiles were generated by using the average intensity of the reflectance response of the first surface mirror. As described in Chapter 2, the full width half maximum FWHM of the intensity profile defines the optical slice

Mag.	NA	Working	Ideal Optical Slice ( $\mu\text{m}$ )			
		Distance (mm)	488 nm		643 nm	
			slit	hole	slit	hole
20 $\times$	.45	8.2-6.9	4.43	3.06	5.83	4.03
40 $\times$	.60	3.6-2.8	2.37	1.63	3.12	2.15

**Table 3.3.** Properties of the objectives used for confocal imaging. The optical slices assume an imaging medium of Air

thickness.

When plotted the intensity profile has a shape similar to a Cauchy-Lorentz function. The function is defined <sup>†</sup> as:

$$y = y_0 + \frac{2A}{\pi} \frac{w}{[4(x - x_c)^2 + w^2]}, \quad (3.1)$$

where A is the scale for the area beneath the curve, w is the FWHM,  $x_c$  is the center position, which corresponds of the maximum value of the function and  $y_0$  is the y offset relative to the function starting at zero. The location of half maximum is found by subtracting the background noise and dividing the peak intensity.

For each of the 20 $\times$  and 40 $\times$  microscope objectives, the measured optical slice thickness is larger than the theoretical thicknesses [16, 17]. For example, the 20 $\times$  objective with an NA of 0.45, with air as the medium, has a theoretical optical slice thickness of 5.83  $\mu\text{m}$  and a measured optical slice of 7.91 $\mu\text{m}$ , which is a 35% increase. However, the theoretical axial resolution does not account for additional aberrations in the optical path. Sources of the additional aberrations include internal focusing lenses, galvanometer mirror, and camera optics.

---

<sup>†</sup> <http://www.originlab.com/www/helponline/Origin/en/UserGuide/Lorentz.html>

Mag	Laser	Slit Opening $\mu\text{m}$	Actual $\mu\text{m}$	Lorentz $\mu\text{m}$	
20 $\times$	Red	22	11.34	11.25	
		35	9.84	13.98	
	Blue	22	12.33	13.99	
		35	10.17	redo	
	40 $\times$	Red	22	8.56	10.31
			35	9.77	10.26
Blue		50	9.41	9.98	
		22	11.30	12.04	
	Blue	35	8.65	9.71	
		50	8.9	12.36	

**Table 3.4.** Comparison of theoretical and experimentally measured optical slice thicknesses using slit apertures with blue(488 nm) and red (643 nm) illumination.

### 3.2.4 Objective Offsets

There exists two independent focal location offsets that must be accounted for when using the microscope and confocal unit regardless of the light source. First, objects are shimmed to increase the working distance of objectives with respect to the samples on the stage. Originally, the maximum height of the objective turret was too small to image through a microfluidic test section. This is primarily do to the design of the stage, which added a centimeter to top of the stage. The shims are not perfectly parallel and alter the center of the FOV and focal depth, the latter is the desired effect. Lateral misalignment was measured using the change position of a reference point. Objects are designed to maintain focal location and FOV when switching between objectives lens on the microscope turret. The axial offsets are not equivalent. The focal depth error was measured by focusing a reference and switching to another objective and refocusing. Physical offsets for the three axes are presented in Table 3.5. Moving objectives or replacing shims will alter the offsets.

Internal focusing optics within the confocal assembly produces a second focal



	Z - Axis ( $\mu m$ )	X - Axis ( $\mu m$ )	Y - Axis ( $\mu m$ )
10x $\rightarrow$ 20x	-76.95	-176	114
10x $\rightarrow$ 40x	-207.60	273	124
20x $\rightarrow$ 40x	-130.65	-97	10

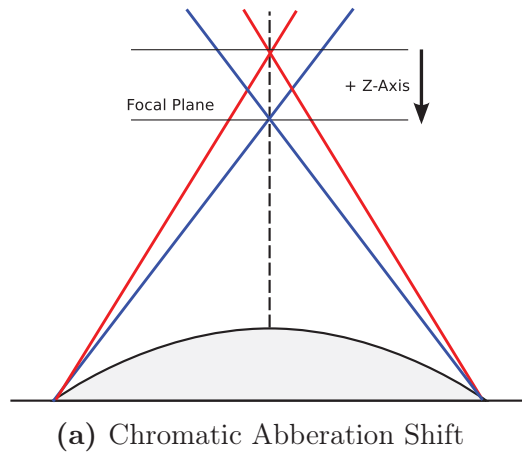
**Table 3.5.** Table of physical optical offsets for three objectives, 10x, 20x, and 40x. The shifts are relative to the 10 $\times$  objective. For the z-axis the negative motion implies a movement of the objective closer to the stage, (up).

depth offset which manifests when switching from widefield (eyepieces) to confocal imaging. The confocal microscope was adjusted to decrease the Z-axis offset and care should be taken when using cameras with different sensor sizes and locations.

### 3.2.5 Chromatic Aberrations

Chromatic aberrations are formed when light of different wavelengths are focused to different depths through the same lens. The amount of shift is determined by the properties of the objective lens. Fluorite is commonly used to correct chromatic aberrations because it has a low dispersion constant which produces a relatively flat response with respect to different wavelengths of light. More advanced techniques use of additional lens components, such as an achromatic doublet. An achromatic doublet is an assembly of two lenses, a convex and concave, which are in contact and have different dispersion coefficients. Different color light is focused to approximately the same location, usually the correction is based on shifting the location of the red and blue beams to the green.

Chromatic aberrations requires additional depth calibration for increased depth measurement accuracy. Figure 3.7a depicts the difference in focal depths between the blue and red laser beams used for excitation in the RSFC. Focus offsets were measured by focusing on a reference with the blue laser and then refocusing with the red. The



(b) Values of Chromatic Abberation Shift

	$\Delta Z$ ( $\mu\text{m}$ )
10x	10.20
20x	1.70
40x	1.95

**Figure 3.7.** Chromatic aberration occurs when shifting from the blue to the red laser. The positive number in the table represents movement of the objectives away from the sample (down)

change in depth is equivalent to the chromatic aberration. The reference was a first surface stage micrometer which removed any error from changes in refractive index.

### 3.2.6 Spherical Aberration

A spherical aberration is create when light passes through a mismatch of refractive indexes. Light passing through a step change in refractive index will bend either towards or away from the the optical axis. A transition from low to high RI bends the light towards the optical axis, away for a high to low transition. A simple light path is depicted in Figure 3.8. Changes in light angles as it passes between changes in RI are related using Snell's law

$$n_1 \sin(\theta_1) = n_2 \sin(\theta_2) \quad (3.2)$$

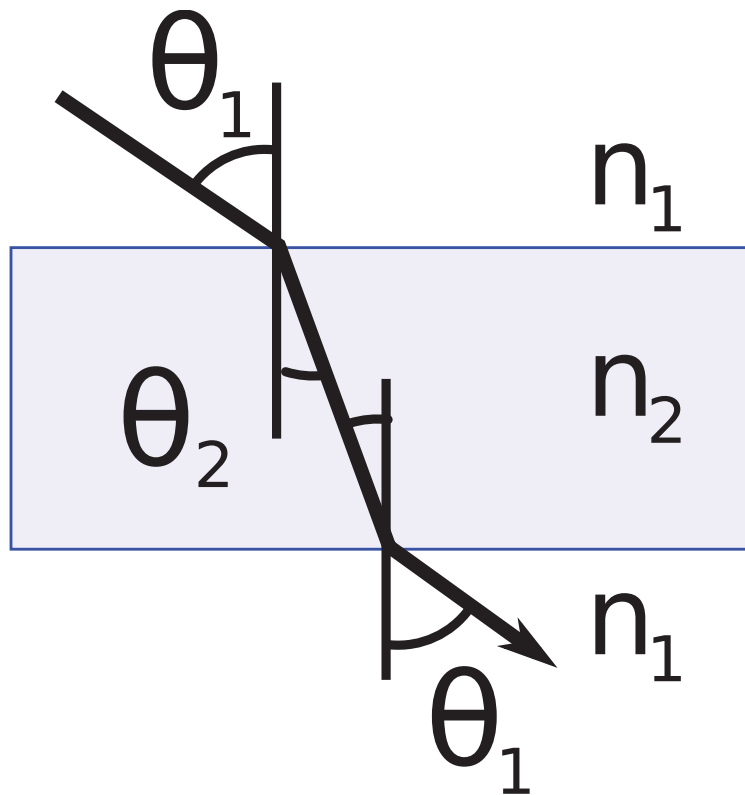


**Figure 3.8.** Transmitted light path transitioning from air to glass to air again. The refractive index change bends the light path.

where  $n_*$  is the RI for the medium and  $\theta_*$  represent the angles light relative to the optical axis.

Light returning from a epi-illuminated sample experiences a spherical aberration caused by the RI difference between the glass slide/cover slip and objective medium. Two methods are commonly used to remove the spherical aberration without the user being aware of the correction. First, immersion objective lens use a liquid with a RI matched to the RI of the test section to buffer the gap between the sample and the lens. This creates a continuous optical path for the returning light. Second, a correction collar is integrated into modern air immersion objective lens designed for imaging biological samples. The correction collar is adjusted until the sharpest image is obtained. Corrections for common glass cover slips and slides are normally identified on the correction collar.

A correction factor is required when measuring the depth within a sample that has a RI that is different than the immersion RI of the objective lens. The depth measurement will inaccurately report a depth that is closer than the actual sample when using an air immersion lens, depicted in Figure 3.9. This shallow measurement is referred to as the apparent depth,  $d_{app}$ . A classic correction for the spherical aberration relates the actual depth,  $d_{act}$  to the apparent depth using Snell's law and the small angle approximation. The correction factor is the ratio of the refractive indexes. [24–26]

$$d_{act} = \frac{n_{sample}}{n_{air}} d_{app} \quad (3.3)$$

This simple correction does not accurately determine the actual depth when the objective lens have acceptance angles larger than 20 degrees. The acceptance angle is found knowing the RI of the objective lens immersion medium and the NA. The

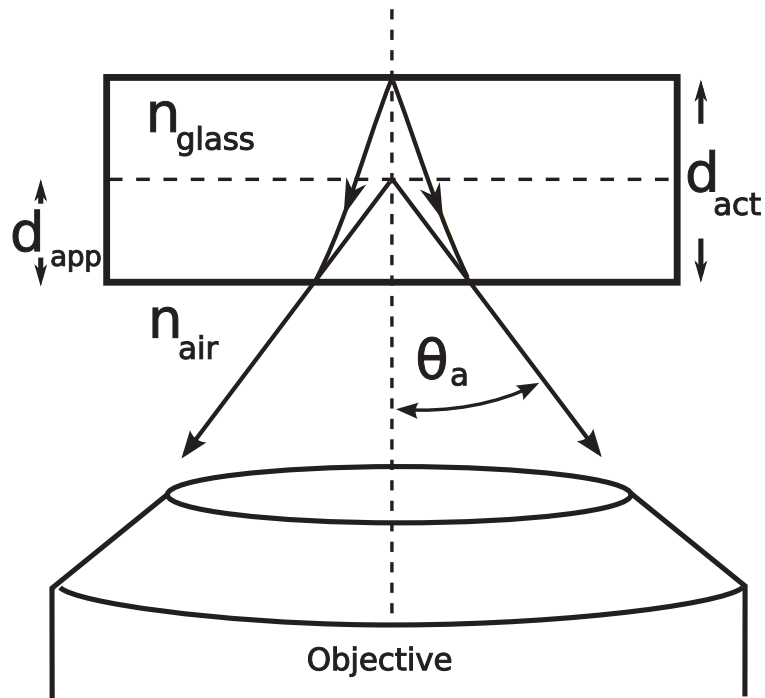


**Figure 3.9.** A change in refractive index between the objective medium and test section creates a spherical aberration which must be corrected to accurately measure the test section thickness.

numerical aperture is defined as

$$\text{NA} = n \sin(\theta_A) \quad (3.4)$$

The three objectives used for this research, 10, 20 and 40 $\times$ , have acceptance angles of 14.48, 26.74, and 36.87 degrees, respectively. For low magnification, low NA objectives, Equation 3.3 will provide the actual depth with an error of less than 4%. But as the NA increases, so does the error, which is close to 10% for the 40 $\times$  objective lens. The depth correction is expanded to include the actual angles using geometric optics.

$$d_{\text{act}} = \frac{\tan(\theta_G)}{\tan(\theta_A)} d_{\text{app}} \quad (3.5)$$

the glass angle,  $\theta_G$  is found using Equation 3.2. The combined correction is

$$d_{\text{act}} = \frac{\tan(\theta_A)}{\tan \left[ \sin^{-1} \left( \frac{n_{\text{air}}}{n_{\text{glass}}} \sin(\theta_A) \right) \right]} d_{\text{app}} \quad (3.6)$$

This is the solution for light originating from a planar test section with a single step in index of refraction. Chapter 4 has expanded this correction for two RI steps and a non-planar test section.

### 3.3 General Confocal Microscopy Research Setup

A schematic of the general RSFC experimental setup is presented in Figure 3.10. The RSFC unit was installed on a Nikon TE-2000 inverted microscope. A floating, vibration isolation table minimized external disturbances. Four imaging ports

(3 accessible) are available for imaging on the TE-2000 inverted microscope. Port 5 (left) is reserved for the confocal microscope, while ports 2 (Right) and 4 (front) are used for wide field imaging, and port 1 is the eyepieces. The stock microscope stage was replaced with a Prior Scientific Proscan II precision stage. A Prior Scientific fine focus motor was installed on the right-hand-side course focusing knob. Rack-mounted controllers interface with the confocal microscope and Prior Scientific hardware. Images were recorded using one of three cameras, a Pulnix TM-1325CL, JAI CM-141MCL, and Photron APX RS high speed camera. Frame rates between the RSFC and imaging devices were synchronized using National Instruments hardware and LabView. During most experimental test runs, four pieces of independent software were required to accurately synchronize the hardware.

### **3.3.1 Confocal Microscope Control**

RSFC hardware control was interfaced with custom software provided by Prairie Technologies. Original software required a supported camera for imaging but the software was patched which removed the integrated camera requirements for imaging. The patched version of the software is capable of imaging with supported and unsupported cameras. The software controls the confocal apertures, filter, laser power and scan rates. A maximum scan rate of 250 FPS was available from the gui interface. Command line access can increase the frame rates as high as 2000 FPS. Two ttl input and output bnc connections are available for synchronizing scan rates with external hardware.

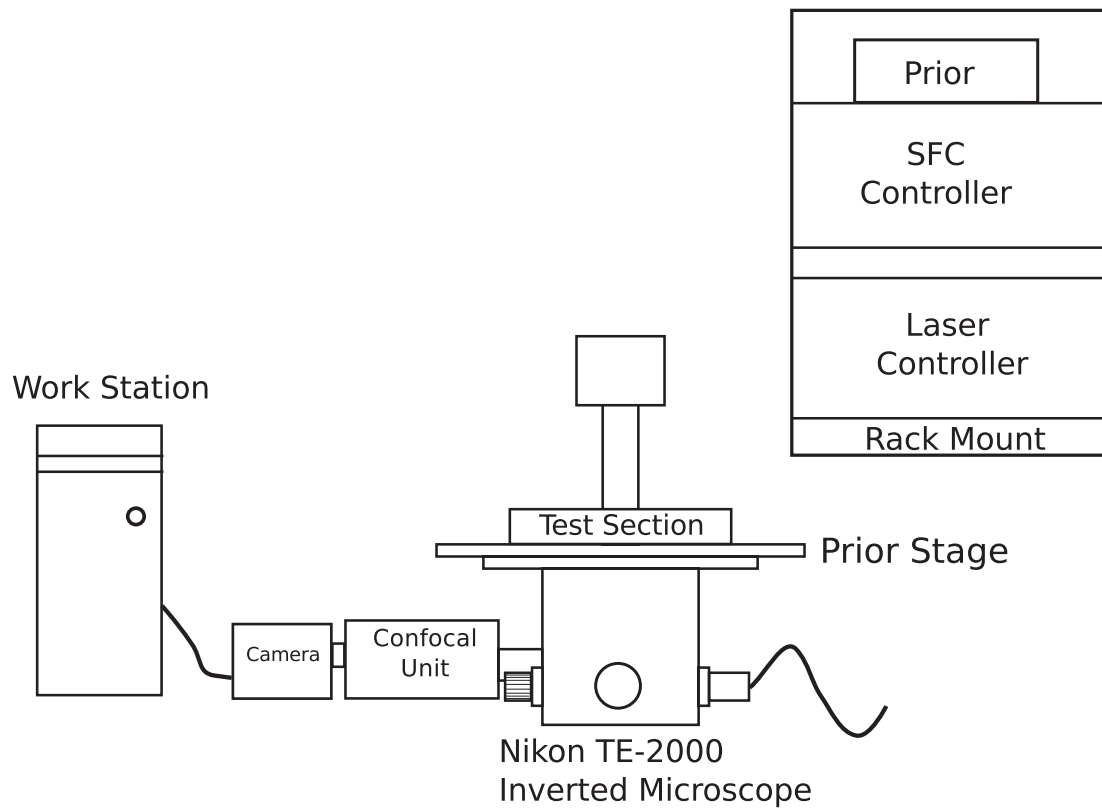


**Figure 3.10.** Schematic of the reflectance, swept-field confocal (RSFC) microscopy experimental setup.



### 3.3.2 Prior Proscan Stage

The Nikon inverted microscope was equipped with a Prior Scientific Proscan II Model H117 stage and a motorized focus drive model “PS3H122”. The stage had a maximum resolution of  $0.040\ \mu\text{m}$  for the X and Y-axes and  $0.002\ \mu\text{m}$  for the Z-axis. Linear encoders were equipped for each axis to provide closed loop feedback control for increased accuracy. Movement of the stage and fine focus was controlled by manually with a joystick or with a software interface. Controller properties were accessed by software control. For example, setting the stage speed, resolution and querying the current position. In practice, the joystick is used for bulk stage movement, while the software provides the highest accuracy of stage positioning. The stage has a RS-232 interface for custom programming. Matlab code for Z-axis scanning is presented in Appendix B

#### 3.3.2.1 Stage Movement

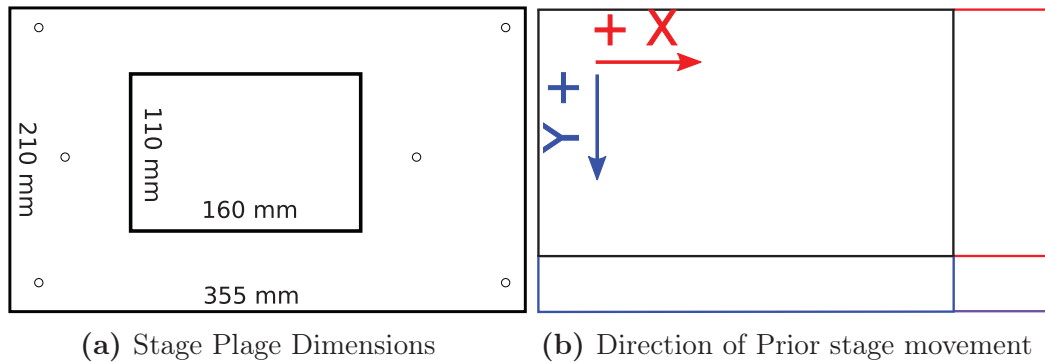


**Figure 3.11.** (a) Schematic of stage with inner opening for experimental plates and (b) coordinate system for referencing stage movement.

The stage uses the right-hand-rule for axis orientation. X-axis was positive when traveling “right” and the Y-axis was positive when displacing towards the front of

the microscope. Z-axis is positive when the objective moves away from the stage or down. The stage orientation is presented in Figure 3.11b. Positive Z-axis motion is counter intuitive, objective motion towards the sample is generally assumed positive. Care must be taken when programming a position in the control software to prevent accidental crashing of the objective into the sample or misreading the objective displacement.

Minimum resolution of the stage was calculated from the pitch of the screw and maximum microsteps of the stepper motor. The stage is equipped with 2mm/rev pitch machine screws and the fine focus had a 100 $\mu\text{m}$ /rev pitch. Each stepper motor had 200 steps per revolution and 250 microsteps per step, a maximum of 50,000 microsteps/rev. The combined system had a maximum resolution of 0.040  $\mu\text{m}$  for the lateral stage movement and 0.002  $\mu\text{m}$  for the fine focusing. The repeatability of the system is limited to the accuracy of the linear encoders. The manufacturer reported a repeatability of 0.1  $\mu\text{m}$  for the X and Y-axes and 0.05  $\mu\text{m}$  for the Z-axis.

‡

### 3.3.2.2 Stage Scale

Position input and output settings for the stage controller requires the setting of the stage sensitivity (ss) and stage sensitivity Z-axis (ssz). This option determined the scale of the stage and focus movement. When SS and SSZ are set to 1, the stage position was controlled with raw step sizes of 0.040 and 0.002  $\mu\text{m}$ , respectively. This was not ideal for data recording and processing. The stage was set to a SS = 25 and SSZ = 5, corresponding to 1  $\mu\text{m}$  and 0.01  $\mu\text{m}$ , respectively. Using ss and ssz limited

---

‡ <http://www.prior.com/downloadcentre/documents/brochuresanddatasheets/H117%20Datasheet.pdf>

the sensitivity of the stage and focus assembly.

### 3.3.2.3 Stage Speed

Stage velocities were set by using the stage maximum speed (sms) command. Velocities are defined by a linear scale without a corresponding distance per time reading. Velocities were physically measured by recording images of a stage micrometer, an Edmunds Cross Stage Micrometer (58608), for different values of stage velocity. Positions were tracked using Spotlight. Linear regression of the position and time calculated the actual stage velocity for corresponding sms values. Calculated velocities are reported in Table 3.6. Linear regression on the stage speeds and the SMS value concluded that the stage had a linear response. The regression had a  $R^2$  values of 1 when rounded at the 5th decimal place. Though reported in the manual as being between 1-100, the stage speed has an upper limit of 250. Stage velocities are determined by multiplying the speed number by linear regression values. Values of 1 and 250 bound the system to a minimum of 239.75 and maximum 59,937.50 ( $\mu\text{m s}^{-1}$ ) for the X-axis and a minimum of 240.2 and a maximum of 60,050.00 ( $\mu\text{m s}^{-1}$ ) for the Y-axis. The decrease in velocity for the X-axis may be attributed to the additional mass of the Y component of the stage. The X-axis moves both the X and y plates while the Y axis only moves itself.

SMS	Velocities ( $\mu\text{m s}^{-1}$ )	
	X-Direction	Y-Direction
1	239.4286833	238.9582731
2	479.4164462	
3	720.2686536	
4	965.3694075	
5	1197.062731	997.1560279
6	1448.785441	
7	1653.019902	
8	1845.745508	
9	2191.692923	
10	2231.099977	2243.245504
20	4671.243383	
30	7214.628455	
40	9025.085611	9613.13889
50	12008.34282	12013.28106
60	13748.14996	
70		16813.91852
...		
100		23826.23367
110	26315.05812	23899.41224
120	28788.40571	25573.25409
140	33555.66013	3210.01984
150	36017.93835	18264.36222
Vel	239.75	240.20
R <sup>2</sup>	0.99975	0.99987
Min (SMS 1)	239.75	240.20
Max (SMS 250)	59,937.5	60,050

**Table 3.6.** Table of the stage velocities found for different sms settings of the stage for the X and Y directions . Stage settings are comp 0 and ss of 25

### 3.3.3 Cameras

#### 3.3.3.1 *Photron Ultima APX-RS Fastcam*

A Photron Ultima APX-RS Fastcam collected confocal images when scanning rates exceeded 60 frames per second (FPS). The camera was capable of recording images at 3000 FPS with 1 megapixel resolution (1024 x 1024 px) and 10,000 FPS at 512 x 512 pixel. Higher recording speeds were available at lower resolutions. The sensor is a 10-bit CMOS with 17  $\mu\text{m}$  pixels. Larger pixels increase the light sensitivity which is invaluable for high speed imaging. Integration of the camera with the confocal required an external trigger output from the SFC, which phase locked the camera frame rate with the confocal scanning. Additional inputs and outputs were available to arm and trigger the camera or other external hardware. The camera was attached to the confocal microscope using a C-mount spacer provided by Prairie Technologies. Images formed on the chip sensor did not completely fill the imaging sensor. This was due to a mismatch between the designed sensor area for the confocal microscope and the camera sensor size. Two options were available when imaging with the high speed camera. Under-filled images decreased the resolution of the images. While an additional internal optic degraded the image quality. A combination of techniques were used dependent on imaging requirements.

#### 3.3.3.2 *JAI*

Confocal images were captured using a Pulnix (JAI) 1325-cl 10-bit and a JAI CM-141MCL 12-bit ccd cameras when frame rates were 30FPS or below. Both cameras have maximum frame rate of 30 FPS, a 2/3 in sensor, 1392 X 1040 resolution and

pixel size of  $6.45 \mu\text{m}$ . The CM-141MCL was newer model that was produced after Pulnix was acquired by JAI. Major differences between camera model included an increase in bit depth, the integration of a mini-camera link connection, and a smaller body of the 141. These cameras were also used for wide field imaging during film thickness measurement tests.

### **3.3.4 Hardware Synchronization**

Clock rates and system start triggers were controlled with a series of transistor-transistor logic (TTL) connections. A National Instruments BNC-2110 connected each input or output of the individual pieces of experimental equipment. Camera and RSFC frame rates were synchronized by a generated square wave with a peak-peak voltage greater than 3.3 volts and less than 5.5. JAI and Pulnix scan rates were limited to 30 FPS and the Photron scan rates were a minimum of 60 FPS to the maximum of the 2000 FPS RSFC limit. Frames were acquired either in free recording, recording starts and finished when the frame buffers were full, or triggered independently. The prior controller has 4 TTL input and 4 output which triggered the beginning test runs involving stage and focus movements. TTL input and outputs were available on the RSFC controllers. RSFC TTL outputs primarily synchronized the frame rates of the camera. MatLab generated RS-232 commands for controlling the Prior Scientific stage and fine focus motor for automated Z-axis scanning.



# 4. MEASUREMENT OF DYNAMIC, THIN, LIQUID FILMS IN MICROCHANNELS USING REFLECTANCE, SWEEP-FIELD CONFOCAL MICROSCOPY

## 4.1 Introduction

Multiphase flow is commonly found in fluid based applications at the microscale. Devices such as Lab-on-a-chip, bio-chips, micro-heat exchangers, liquid delivery systems, monolithic reactors, liquid fuel tanks, and fuel cells [27–30]. Often, microscale multiphase flow involves gas and liquid phases and is referred to as two-phase flow. Microscale two-phase flow occurs over a variety of flow morphologies, or regimes. Flow regimes are used to categorize two-phase flow based on physical appearance of the phases. Common categorizations include bubbly and intermittent flows, which are strongly affected by capillarity; dispersed and annular flows are strongly affected by inertia [2]. A particularly useful flow regime for multiphase microscale applications is “segmented flow”, in which liquid slugs are separated by discrete bubbles of a gas or vapor, yet the liquid phase remains continuous through thin liquid films along the



channel walls. Segmented flow is used to enhance chemical reaction, mixing, and heat transfer.

The presence of an annular liquid film in microscale two-phase flow increases the complexity of predicting device performance [29, 30]. Gas-liquid phase interaction at the microscale necessarily includes capillary, viscous and inertial effects. In addition, instability of a liquid film deposited on a microchannel wall may result in channel-to-channel flow excursions or device level instability [31].

#### 4.1.1 Liquid Film Deposition in Capillary-Scale Channels

Gas-liquid flows in macro and microscale devices can be categorized based on the relative magnitude of surface tension and gravitational forces. A Bond number ( $Bo = \Delta\rho g L^2 / \sigma$ ) less than one indicates that surface tension is the primary force dictating static interface shape, where  $\Delta\rho$  is the fluid density difference across the interface,  $g$  is gravitational acceleration,  $\sigma$  is surface tension, and  $L$  is the characteristic length scale of the interface and is typically taken to be the channel width. Dynamic interfaces in low Bond number channels will remain surface tension dominated if the Capillary number ( $Ca = \mu V / \sigma$ ) remains small, where  $V$  is the interface or meniscus velocity and  $\mu$  is the liquid viscosity. The interface will begin to distort due to viscous forces when  $Ca > 10^{-3}$ , resulting in a non-spherical meniscus shape [25].

The thickness of liquid film deposition behind a receding meniscus depends upon the Capillary number ( $Ca$ ), channel geometry and wettability [25, 32]. At a critical Capillary number, a liquid film will be deposited behind a moving meniscus. Film thickness approximations are generally reported as a function of  $Ca$  for wetting fluids in round channels [1, 33–35]. The classical relationship for film thickness as a function

of  $Ca$  and channel radius is shown in equation 4.1.

$$\frac{h}{r} = 1.34 Ca^{2/3}, \quad (4.1)$$

where  $h$  represents the film thickness and  $r$  is the channel radius [34]. During derivation of equation 4.1 the bubble was divided into several transition regions beginning from the bubble nose until it reached a region of “flat film”. Equation 4.1 is only valid for the this “flat“ region.

Instabilities in the film can develop leading to secondary film structures for sufficiently long gas bubbles or along extended annular liquid film deposition having small capillary numbers [36, 37]. These structures create non-uniform pressure potentials in the liquid film which either “pinch off” to form plugs or collapse back into the wall. Channel geometry, wettability, and fluid properties alter the response of these thin liquid films.

At high Capillary and Weber numbers, the behavior of liquid films in microchannels is not well understood. As a result, pressure drop and flow morphology is difficult to predict and remains empirically defined. A more thorough understanding of liquid film behavior in microchannels is required for the development of microscale two-phase flow predictive models. The study of film dynamics at sub-millimeter length scales and millisecond dynamic response times requires new measurement techniques.

#### 4.1.2 Measuring Liquid Film Thickness in a Microchannel

Liquid film thickness measurement techniques can be divided into two general categories: local and bulk measurements. Bulk film thickness measurements assume a

uniform film thickness and infer the thickness using time averaged measures of mass flow. For example, a common technique for estimating film thicknesses uses the difference in weight of a microfluidic test section before and after liquid deposition. The film thickness is then calculated by dividing the deposited liquid volume by the test section surface area. This technique assumes that the film will be uniform along the entire channel length and the channel has a constant radius. These assumptions limit the application of this measurement technique to long test sections where the error associated with a non-uniform film and varying channel radius are minimized. Local measurements techniques measure liquid film thickness at a specific location in the test section. The thickness measurement may be a point or an area. Common techniques include optical, resistance, capacitance, and acoustic.[38]

Reflectance measurements are common in the study of gas-liquid interface disturbances in two-phase flow. Wave frequency was measured using reflected light [39]. Similarly, wave amplitude was measured using reflected light [40]. The mean film thickness had to be inferred from bulk measurements. Film thicknesses of gravity-driven macroscale two-phase flow were measured using a commercially available laser focus displacement meter [41]. This system records the peak intensity of a point source harmonically modulated through a liquid film. This technique was also used to measure film thickness in a microchannel and was applied to segmented flows [42]. Similarly, for liquid film deposition in which liquid was withdrawn from a capillary, film thickness was measured for vertical and horizontal flows in both circular and non-circular test sections [43, 44]. While successful, these methods use point-source illumination precluding field measurements of liquid film dynamics.

Interferometry techniques have been successfully employed to measure film thicknesses and surface dynamics over an area [45]. Interactions between the light reflected

from gas-liquid interface and inner channel wall contains information about the change in interfacial shape. Interferometry was used to measure the thickness of falling films in macroscale flow [46]. Sharp curvatures, such as near a moving meniscus, and channel wall surface variations limit the applicability of interferometry for microchannel two-phase flow.

Standard wide field microscopy is also hindered by optical properties of microchannel surfaces. For example, a cylindrical test section creates spherical aberrations due to index of refraction mismatches between the liquid and channel wall. Transmitted illumination with microscale two-phase flow results in light passing through multiple dynamic interfaces (top and bottom channel walls) and refractive index mismatches before reaching the imager. Minimizing the difference in refractive index between the fluid and channel wall and use of planar test sections reduce the optical distortions but cannot completely remove the error associated with refraction of transmitted light.

One method for minimizing extraneous information due to refraction is confocal microscopy. Confocal microscopy offers an advantage over traditional wide-field microscopy because a confocal aperture blocks out-of-focus light, resulting in an improved  $Z$ -axis (objective lens axis) resolution. In the absence of out-of-focus light, an “optical slice” is generated, which represents a volume of light that is thin in the  $Z$ -axis, but fills the camera view field. Objective lens numerical aperture, light wavelength, and confocal aperture determine optical slice thickness.

Application of confocal microscopy to microscale flow has been limited. The first reported use was with a laser scanning confocal microscope (LSCM) to perform confocal particle image velocimetry (CPIV) in single phase flow in a round test section [47]. Later, CPIV was adapted to image microscale two-phase, gas-liquid and liquid-liquid flows in the study of blood flow in capillaries [48–51]. Confocal laser induced fluo-

rescence (CLIF) was successfully used to determine film surface profiles in segmented flow, but absolute film thicknesses could not be obtained [52].

Motivated by the need to accurately measure dynamic liquid films in microscale channels, a technique has been developed that uses Fresnel reflections originating from the gas-liquid interface to accurately measure film thicknesses and surface profiles. Traditional confocal microscopy is fluorescence based. In order to measure liquid film thicknesses and surface profiles at high speeds, more light is required than afforded by fluorescence imaging. Epi-illumination can provide sufficient light for these measurements, but requires modification of fluorescence-based confocal microscopy to reflectance based. Reflectance confocal microscopy has been used for diagnosing cell abnormalities in dermatology with a Laser Scanning Confocal Microscope (LSCM) [53, 54] and a tandem spinning disk confocal microscope [21]. For this study, a swept-field confocal system was modified to function in a reflectance mode.

## 4.2 Reflectance Swept-Field Confocal (RSFC) Microscopy Measurements in Microchannels

Liquid film thicknesses in capillaries (circular microchannels) were measured using a reflectance swept-field confocal (RSFC) microscope in which a 50/50 beam splitter was substituted for the original dichroic mirror. The swept-field confocal unit is manufactured by Prairie-Technologies, Inc. Swept-field confocal microscopes use slits instead of pinholes for confocal apertures. Confocal images are formed by sweeping the slit illumination across the sample. Directional sweeping increases the maximum frame rate and light sensitivity of the confocal microscope, a requirement for high

speed imaging of interfacial dynamics.

Interface reflection intensity images are captured using a Photron APX RS high speed camera attached to a Nikon T2000 inverted microscope with the Prairie Technologies swept-field confocal unit. A Prior Proscan II precision stage and focus motor provide  $X$ ,  $Y$  positioning and  $Z$ -axis control, respectively. Macroview images of the two-phase flow are recorded using JAI CM-141MCL progressive scan camera. Camera exposures are controlled with a National Instruments BNC-2110 pulse generator, which synchronizes both cameras and the confocal galvanometer. Two workstations are required due to bandwidth and memory requirements of controlling each measurement device. Two microscope objective lenses were used: a Nikon 20 $\times$  and 40 $\times$ , providing optical slice thicknesses of approximately 20.7 and 9.2  $\mu\text{m}$ , respectively when using the 488 nm laser.

Reflective swept-field confocal (RSFC) film thickness measurements were conducted using two different types of experiments. The first measured liquid film thickness in segmented two-phase flow. The second measured liquid film thickness behind a liquid plug being withdrawn from a capillary using a plunger.

#### **4.2.1 Segmented Flow Experiments**

Segmented flow was generated using a meniscus tee injection technique that allows for selecting two-phase flow regimes by varying the flow rate of a single phase (gas or liquid) [55]. A 1 mm ID round Vitrocom borosilicate glass channel is inserted beyond the center portion of a plastic tee. Liquid water is injected into the cross port, where a meniscus forms at the channel entrance. Liquid is injected with a 50 ml Hamilton Glass syringe pushed at a precise linear speed with a Harvard Apparatus

syringe pump. The flow rate of pure nitrogen is controlled with precision Omega rotameters. Long lengths of tubing before and after the test section stabilize the segmented flow and decrease variation in bubble length and velocity. The Vitrocom borosilicate capillary (RI = 1.474) is adhered to a borosilicate Fisherbrand glass slide (RI = 1.474) and the channel is encapsulated with Sigma Aldrich glycerol (RI = 1.474). Each element is equivalent in refractive index to the third decimal place.

#### **4.2.2 Film Deposition Experiments**

Film deposition tests consisted of the same imaging setup and test section described above without the two-phase flow generator. A single liquid slug is pulled through the channel at a constant speed. A plunger was held stationary relative to the microscope objectives and the channel was moved using the Prior ProScan stage. Although the tests are limited to a single moving meniscus, the meniscus speed, and hence the Capillary number, can be better controlled in the film deposition experiments as compared to the segmented flow experiments.

#### **4.2.3 Determining Interface Location**

Film thickness measurements are broken into two primary steps: channel wall detection and film interface detection. The location of the interior channel wall is measured using a series of images captured at known  $Z$ -axis locations which span the exterior to the interior of the glass channel. Images are captured at approximately 20 locations along the  $Z$ -axis, with a  $Z$ -axis step size of approximately  $0.5 \mu\text{m}$ .

Liquid film thickness measurements require comparison of bubble velocities and lengths over a series of test runs. The  $Z$ -axis location of the optical slice is held

constant during each test run and the film thickness is determined by compiling multiple test runs at varying z-axis locations with similar bubble velocities. Reflection intensity as a function of objective position provides the method for determining film thickness. The objective lens is moved and another imaging sequence is captured, each test captures images of at least three bubbles. Step sizes along the  $Z$ -axis range from 0.1 - 1.0  $\mu\text{m}$ .

Meniscus velocities and liquid-gas segment length ratios (captured with macroscale imaging) are measured using Spotlight, an image analysis software developed by NASA [56]. Interfacial reflection intensity values are normalized and imported into OriginPro™, where a Gaussian distribution curve fitting routine locates the peak reflection intensity. A correction factor, discussed below, correlates apparent objective focal depth with actual focal depth.

RSFC images are limited to approximately 1.5 diameters (1.5 mm for the current test section) from the leading meniscus. This location is a representative thickness of the entire flat film region, and is only weakly influenced by long-wave instabilities that can occur at 7 to 10 diameters from the leading meniscus [1, 57]. The assumption of axisymmetric film geometry is well justified by the small Bond, Capillary, and Weber numbers.

#### 4.2.4 Depth Correction

Measured objective lens position coordinates must be corrected to account for the spherical aberration created by the change in refractive index along the beam path. The apparent depth of focus,  $\delta_{ap}$ , is the focal point of the objective lens with air as the only transmission medium. The actual depth,  $\delta_{ac}$ , of the focal point is dependent



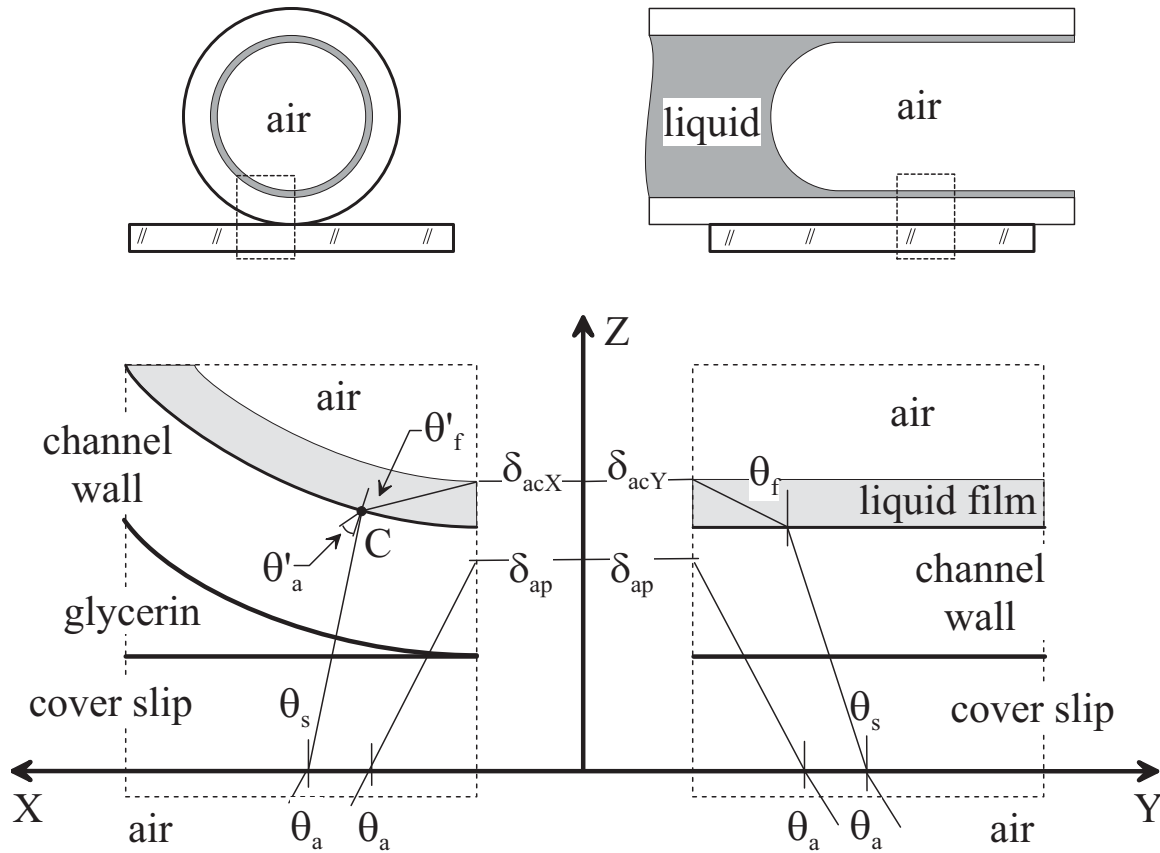


**Figure 4.1.** Light returning from the liquid film requires correction from the radial channel shape ( $X$ - $Z$ ) and along the channel length ( $Y$ - $Z$ ). Corrections relate the apparent depth of the liquid film with the actual interface location. Cover slip, channel, and glycerol are refractive index matched. An average of the radial and lengthwise correction factors determines the interface location.

on the index of refraction of the optical path and test section geometry. Due to the annular shape of the liquid film, depth correction in both the radial and lengthwise directions are needed. Two correction factors have been developed using the geometry defined in Figure 4.1.

Correction factors are based on acceptance angle of the objective  $\theta_A$ , which is found using the definition,  $NA = n \sin(\theta_a)$ . Using an index of refraction,  $n$ , of 1 for air, the acceptance angles are  $26.74^\circ$  and  $36.87^\circ$  for the  $20\times$  and  $40\times$  objective

lenses, respectively. The cover slip, channel, and glycerol are index matched to three decimal points ( $n_s = 1.474$ ); the angle of a light ray traveling through these three media is  $\theta_s$ . The angle of a light ray traveling through the liquid film is  $\theta_f$ . Angle measures denoted with a prime ( $\theta'_a$  and  $\theta'_f$ ) are referenced from the normal of the curved channel wall in the  $X$ - $Z$  plane. Similar correction factors were developed using geometric optics based on similar test section geometries [41, 43].

The lengthwise correction factor in the  $Y$ - $Z$  plane, shown in Figure 4.1, is only dependent on the linear geometry along the length of the channel. The ray angles at each linear interface are found with Snell's law,

$$n_a \sin(\theta_a) = n_s \sin(\theta_s) = n_f \sin(\theta_f) \quad (4.2)$$

where  $n_a = 1$ ,  $n_s = 1.474$ , and  $n_f = 1.33$  for water and  $n_f = 1.474$  for Cargille oil. The apparent depth is constant for both the radial and lengthwise corrections, and is found with equation 4.3.

$$\delta_{ap} = Z_c + \frac{X_c}{\tan(\theta_a)} \quad (4.3)$$

The actual depth of focus in the lengthwise channel plane  $X$ - $Z$  is found with equation 4.4.

$$\delta_{acY} = \frac{\tan(\theta_a)}{\tan(\theta_f)} \delta_{ap} \quad (4.4)$$

The correction in the  $X$ - $Z$  plane (radial direction), shown in Figure 4.1, is dependent on circular geometry at the refractive index step change. Light enters the film at point C, where it is refracted. The horizontal coordinate ( $X_c$ ) of light intersection

with the channel wall is found with equation 4.5.

$$X_c = \sin(\theta_a - \theta'_a)R \quad (4.5)$$

Where  $R$  is the channel radius. The vertical coordinate ( $Z_c$ ) of light intersection with the channel wall is found with equation 4.6.

$$(Z_c - R)^2 + X_c^2 = R^2 \quad (4.6)$$

Snells law determines the angle of refraction relative to the channel wall normal, shown in equation 4.7.

$$n_a \sin(\theta'_a) = n_f \sin(\theta'_f) \quad (4.7)$$

The actual depth of focus in the  $X$ - $Z$  plane is found with equation 4.8.

$$\delta_{acx} = Z_c + \frac{X_c}{\tan(\theta'_f + (\theta_a - \theta'_a))} \quad (4.8)$$

The average of the lengthwise and cross-sectional corrections determines the actual depth of the liquid film interface, shown in equation 4.9.

$$\delta_{ac} = \frac{\delta_{acx} + \delta_{acy}}{2} \quad (4.9)$$

The solution to equation 4.2 through equation 4.9 is iteratively solved using Engineering Equation Solver (EES). Average correction factors were determined using the ratio of measured and actual depths for the experimental range of Ca. Correction factors are equal to the third decimal point for the range of film thicknesses

predicted by Equation 4.1, 1.401 and 1.483 for 20× and 40× objectives, respectively. These correction factors are applied to the experimentally measured apparent depth to determine the actual film thickness.

#### 4.2.5 Measurement Uncertainty

Uncertainty in the RSFC film thickness measurement technique is primarily caused by Capillary number fluctuations, objective lens focal position, camera bit-depth resolution combined with laser beam waist and image intensity variations. Compressibility effects in the gas-phase cause non-steady bubble motion during segmented two-phase flow, resulting in variations of Ca. The uncertainty in capillary number varies in each test, and is taken as the difference in the range of Capillary numbers. Capillary number uncertainty is mitigated during the film deposition tests by precisely controlling the rate at which the plunger drives the liquid slug.

Focused laser light reaches a maximum intensity at the center of the optical slice, following the same optical path with or without the confocal aperture. Geometric optics portrays the focal point of a laser source as an infinitesimal point, crossing then expanding sharply. In reality, the beam close to the focal point follows a Gaussian profile, focusing to a finite “beam waist”. The radius of the beam is a function of axial ( $\zeta$ ) position, and is described by equation 4.10 [58].

$$w = \frac{\lambda}{\pi\theta} \left\{ 1 + (\zeta\theta)^2 \right\}^{1/2}, \quad (4.10)$$

where  $\lambda$  is the wavelength of light in water, the medium in which the the beam waist is produced when detecting interfacial film. The angle of beam convergence is  $\theta$ . The

minimum beam waist is  $w_0 = \lambda/\pi\theta$ .

The time-averaged normalized intensity distribution ( $I$ ) is described by equation 4.11. [59]

$$I(r, \zeta) = \frac{2}{\pi w^2} e^{2(r/w)^2} \quad (4.11)$$

The axial location in the beam is  $\zeta$  and  $r$  is in the radial location in the beam. The origin is positioned at the center of the beam waist and the profile of the beam along its axis is described by  $w$ . At  $r = 0$ , beam intensity reaches its radial maximum and at  $\zeta = 0$ , beam intensity reaches its axial maximum. With a 20 $\times$  objective lens, the maximum normalized intensity is 0.626. With a 40 $\times$  objective lens  $I(0, 0) = 1.129$ .

When reflecting a Gaussian beam off of an interface the maximum reflectance intensity occurs when the interface is located at  $\zeta = 0$ . If the interface is not located at  $\zeta = 0$ , there is a decrease in the reflectance intensity. The ability to distinguish two unique points in the  $Z$ -direction based on a change in reflectance intensity when illuminated with a Gaussian beam depends upon the beam waist and camera bit depth. There is a small intensity variation radially across the focal plane as described by equation 4.11 and that variation is averaged across at least one pixel. The minimum fraction of intensity detectable with 10-bits is 0.9990. Solving equations 4.10 and 4.11 for the variation in  $\zeta$  for the detectable limit in  $I$  yields the distance criterion for independent depth measurement. A 10-bit imager with  $\lambda = 488$  nm results in an interfacial reflection location uncertainty of  $\pm 0.35\mu\text{m}$  and  $\pm 0.15\mu\text{m}$  for the 20 $\times$  and 40 $\times$  objective lenses, respectively.

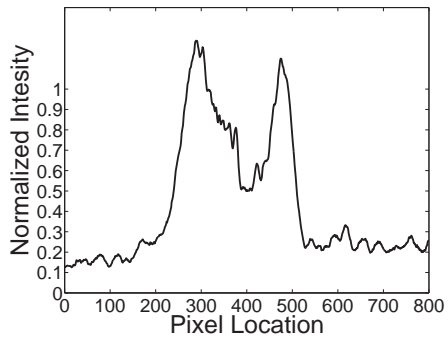
Uncertainty due to incremental optical slice position changes is one half the optical slice step size. Actual peak locations can be, at maximum, half way between measurement points. To minimize this error, the maximum intensity in the  $Z$ -axis is

determined using a Gaussian curve fit of the intensity profile. Step size error is more than an order of magnitude smaller than the minimum repeatable  $Z$ -axis step size of  $0.01\mu\text{m}$  for the focus motor and is therefore neglected.

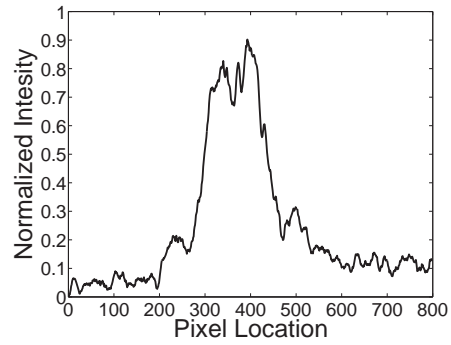
Light is reflected into the objective lens when an interface is nearly perpendicular to the  $Z$ -axis; light is scattered from surfaces sufficiently angled relative to the  $Z$ -axis. This spherical aberration causes the peak in the film interface reflection intensity profile shown in Figure 4.2b. The peak shows the area of the film surface reflecting light into the objective lens and the intensity of the reflected light. The intensity profile of an interfacial reflection is also influenced by the location of the optical slice relative to the interface. An optical slice located above the film interface intersects the curved surface at two points causing two peaks in reflection intensity, as shown in Figure 4.2a. Figure 4.2c shows a less intense reflection because the optical slice is located below the film interface.

Images are cropped to a film interface area that is nearly perpendicular to the  $Z$ -axis to reduce the effect of spherical aberration. Images captured with the optical slice located at the interface are used to determine the area of maximum reflection intensity for an image set. An area approximately 200 px by 200 px at the image center represents the highest 5% of reflection intensity for an image set. All images in a set are cropped to this area to determine reflection intensity as a function of optical slice location.

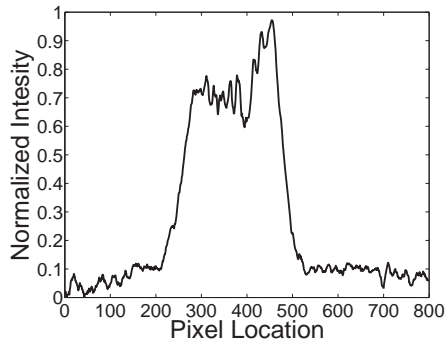
A representative intensity plot and the corresponding Gaussian peak fits are seen in Figure 4.3. Peak detection, using a routine within Origin Pro, provides the  $Z$ -axis locations needed for the fitting functions. Image intensity profiles consists of two peaks; the peak at  $Z \approx 1$  represents the channel wall and the peak at  $Z \approx 2$  is the gas-liquid interface. The apparent film thickness is found by taking the difference



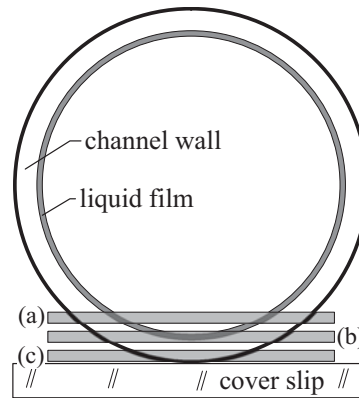
(a) Confocal slice above liquid surface.



(b) Liquid surface detection.



(c) Confocal slice below liquid surface.



(d) Relative position of optical slices.

**Figure 4.2.** Normalized intensity profiles of the image intensity across the radius of the channel, taken at the center of the evaluation AOI.

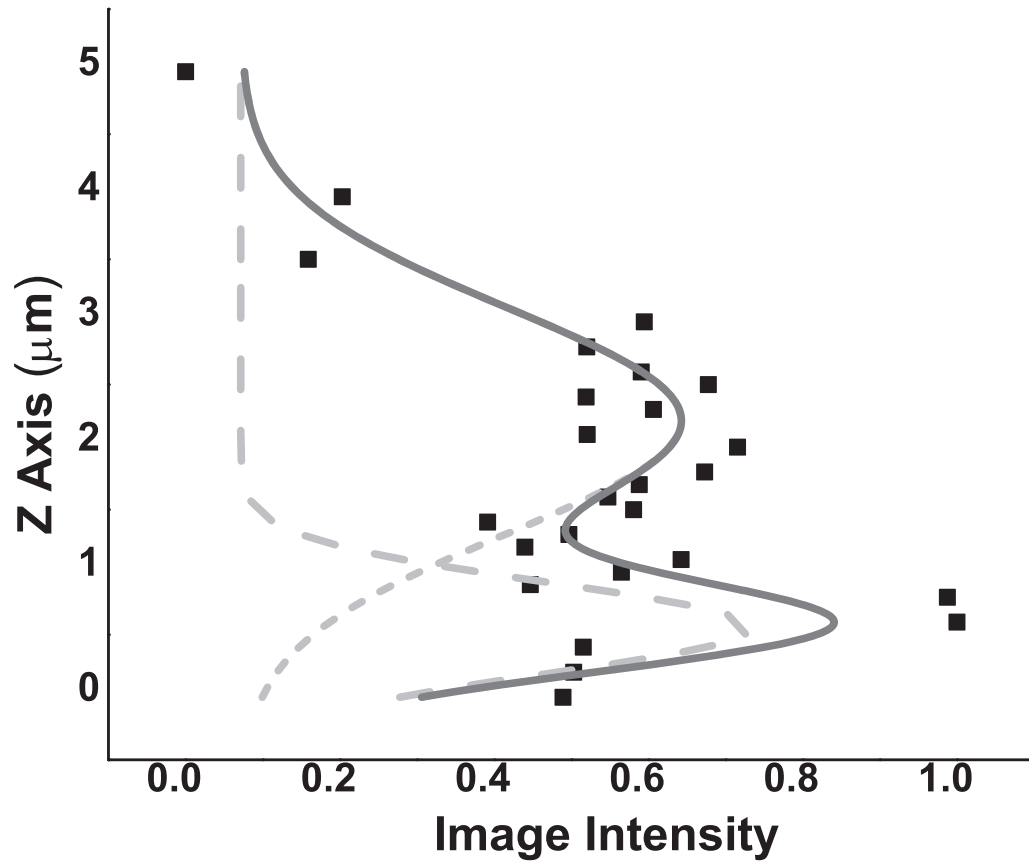


**Figure 4.3.** Averaged image intensities measured across the channel wall and liquid film. Gaussian fits, combined with peak analysis, detected the wall and liquid film surface in this excessively noise intensity plot. The dashed lines represent the individual Gaussian curving fitting functions, and the solid line is the combination of the two fits.



between the detected interface location and the channel wall location found during calibration. Actual film thicknesses are determined after applying the refractive index correction from Equation 4.9 to the apparent film thickness.

### 4.3 Discussion

Experimentally obtained RSFC film thickness measurements are compared to the predicted film thicknesses of Equation 4.1 in Figure 4.4. Solid squares represent the measurements from the segmented flow experiments and empty squares represent the film deposition experiments. The gray band represents the accuracy range for the approximation, assumed to be  $\pm 20\%$  of the predicted value. RSFC film thickness measurement uncertainty has been added to the measured film thicknesses. Both sets of experimental data are within the the experimental uncertainty. Initial data taken with the RSFC film measurement technique demonstrates that the film thicknesses can be measure accurately. The discrepancy between the measured film thicknesses with the analytic model may be due to the lack of control when generating the two-phase flow. Compressible gas effects were evident during post processing, with bubbles undergoing acceleration during the measurements. This affect is realized with the large error bars in the Ca axis.

Images of interface reflection intensity are used to determine film thicknesses. The same images contain interference patterns which may be used to determine film curvature, facilitating simultaneous capture of local film thickness and dynamic response of the interface. The interference patterns shown in Figure 4.5 can be used to measure interfacial curvature.

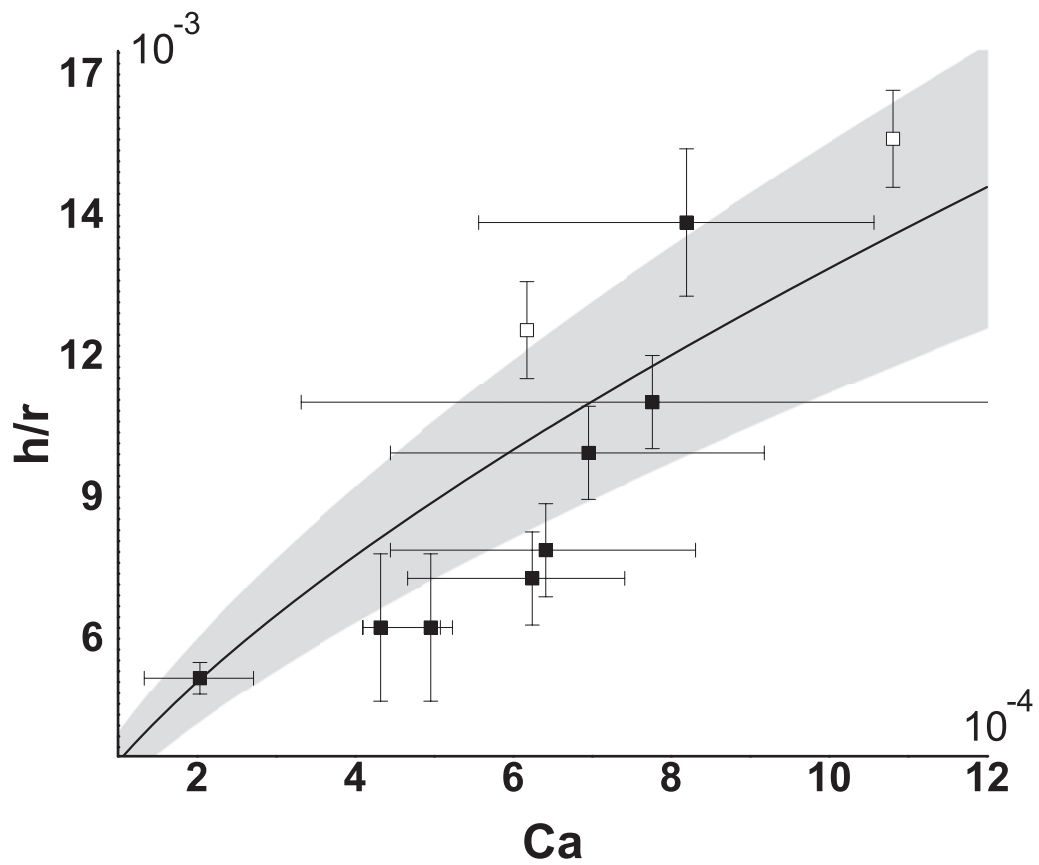


**Figure 4.4.** Comparison of experimental film thickness measurements (square symbols) with Bretherton film thickness approximation (solid line), Equation 4.1. The gray band represents the confidence interval of 20% for the film thickness approximation.

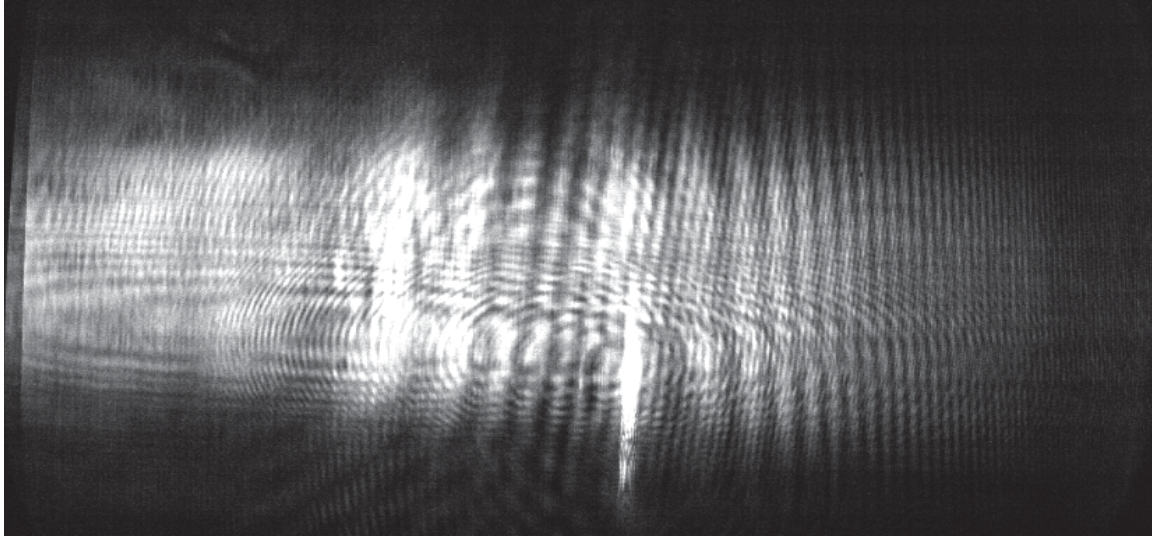


**Figure 4.5.** Image of the reflective response from a dynamic liquid film with flow from right to left. The decrease in interference wavelength from left to right indicate an increasing film thickness and increasing interface curvature.

## 4.4 Conclusion

Initial RSFC film thickness measurement results indicate that this technique is capable of detecting and measuring the dynamic response of the gas-liquid interface in microscale, two-phase flow. Measured distances of peak reflection intensity, coupled with statistical analysis, provides an accurate measurement of the film thicknesses within the uncertainty of the technique. The RSFC technique is capable of 0.5 micron  $Z$ -axis resolution and 5 ms response time. Temporal limitations are due primary to the limitation of the wide field imaging synchronization. Frame rates of 2000 fps are available and will be utilized in future experimental tests. Improving the two-phase flow generation will decrease the uncertainty in film thickness measurements between  $Z$ -axis locations. RSFC images contain interference patterns which could potentially provide instantaneous gas-liquid film profiles.

# 5. REFLECTANCE, SWEEP-FIELD CONFOCAL PARTICLE TRACKING VELOCIMETRY NEAR A MOVING CONTACT LINE

## 5.1 Introduction \*

Standard wide field microscopy images of curved, gas-liquid interfaces are distorted due to refraction. Light passing through the curved surface is refracted due to a change of refractive index between the liquid and gas phases, similar to a lens. For example, information near the gas-liquid interface is clearly distorted in Figure 5.1. Left of the curved surface is liquid (water) and the dark region is the gas phase. The image was formed by illuminating a plug water in a glass capillary using transmitted light. Bright sections of the image are formed as light passes through the test section with minimal refraction. Areas with large curvature, such as the meniscus, glass channel wall and liquid film, bend the light at angles too extreme for detection by the objective lens.

Image distortion affects the accuracy of flow field measurements near a moving

---

\* Portions for this chapter were submitted to PIV11, used with permission (Appendix A.2 Paper number PIV11-164 - Visualization of Flow Near a Steadily Advancing Meniscus

meniscus using imaging techniques like particle image velocimetry (PIV) and particle tracking velocimetry (PTV).[17] Predictive models of internal fluid dynamics near a moving contact line require complete flow fields for validation. Standard transmitted light imaging techniques are severely limited when imaging near the gas-liquid interface.

Motivated by this imaging need, a technique for imaging reflective particles near curved interface was developed using the reflectance, swept-field confocal (RSFC) imaging technique. The optical distortion caused by the gas-liquid interface was reduced through a combination of optical slicing and epi-illumination. Confocal optical slices removed out-of-focus information near by spatially filtering the excitation and emitted light. Epi-illumination excites particles below the curved surface preventing distortion caused by changes of refractive index at the gas-liquid surface.



**Figure 5.1.** Image of gas-liquid interface of a liquid plug in a microchannel. The interface acts as a lens that bends the light away from the optical path creating the dark region near the meniscus.

## 5.2 Background

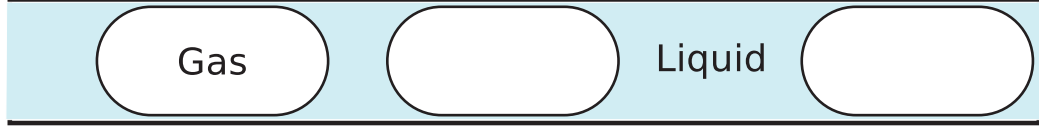


**Figure 5.2.** Schematic of the microscale, gas-liquid, segmented, two-phase flow. Segmented flow is defined by separate phases, a bubble and liquid slug, which may or may not have a continuous liquid film (pictured).

Microscale segmented flow is defined by a series of liquid plugs separated by gas bubbles, depicted in Figure 5.2. Segmented flow has been reported as bubble train, intermittent, bolus, or Taylor bubble flow.[1, 2, 60, 61] Microscale is defined by the length scale at which surface tension has a greater influence than gravity on the interfacial shape. The Bond number,  $Bo = \rho g L^2 / \sigma$ , relates the magnitude of gravitational forces to surface tension. Generally, the transition from macroscale to microscale for gas-liquid flow occurs when the  $Bo$  is much less than 1, classically defined as 0.1. Holding fluid properties constant, difference in density of the fluids ( $\rho$ ) and surface tension ( $\sigma$ ), the characteristic length ( $L$ ) determines the scale. Segmented flow was generated in test sections and with fluid pairs which were well within the microscale.

At the microscale, interface velocities are often reported using the non-dimensional ratio of viscous forces to surface tension. Capillary number,  $Ca$ , is defined as

$$Ca \equiv \frac{\mu V}{\sigma}$$

where,  $\mu$  is the dynamic viscosity of a single fluid of the pair,  $\sigma$  is surface tension of the fluid pairs, and  $V$  is the characteristic velocity of the fluid.  $Ca$  for each fluid in the two-phase flow should be considered because gas and liquid phases could have

different velocities and viscosities.[1] At small  $Ca$  the shape of the meniscus will remain spherical but viscous forces will begin to distort a gas-liquid interface as the  $Ca$  approaches  $10^{-2}$ . [25] As the  $Ca$  increases the interface flattens, creating a thicker liquid film surrounding the gas bubble. Images of a gas-liquid with a liquid  $Ca$  of  $10^{-2}$  and  $10^{-3}$  are presented in Figure 5.3. There exists a clear difference between the two images of the gas-liquid interface. Relative to each other, the smaller  $Ca$  meniscus has a crisp interface while the larger  $Ca$  is blurred with a visibly thicker liquid film.

Magnitudes of the  $Ca$  affect the internal flow profiles of segmented, two-phase flow. Flow fields within the liquid phase of segmented flow were theoretically predicted to be internally recirculated with a tread-like profile at  $Ca$  less than 0.25.[1]. Taylor reported the cutoff using  $m$ , the square root of Capillary number, Figure 5.4 contains the original predicted flow fields. Theoretically, three flow patterns are possible but only (a) and (b) have been experimentally observed.[48–50, 60–63] Taylor predicted a  $Ca$  greater than 0.25 would result in a complete bypass of the bubble. The development of the RSFC PTV technique is driven by the inability to measure internal liquid flow fields near the meniscus, contact line, and liquid film to validate predictive models of internal fluid dynamics. Additionally, there is a lack of available experimental data that provides a parametric investigation of slug length,  $Ca$ , wettability, and channel geometry on the fundamental flow patterns within the liquid phase near a moving meniscus.

### 5.2.1 Flow Visualization

Two common techniques for optically measuring internal liquid flows are particle image velocimetry (PIV) and particle tracking velocimetry (PTV). Both techniques

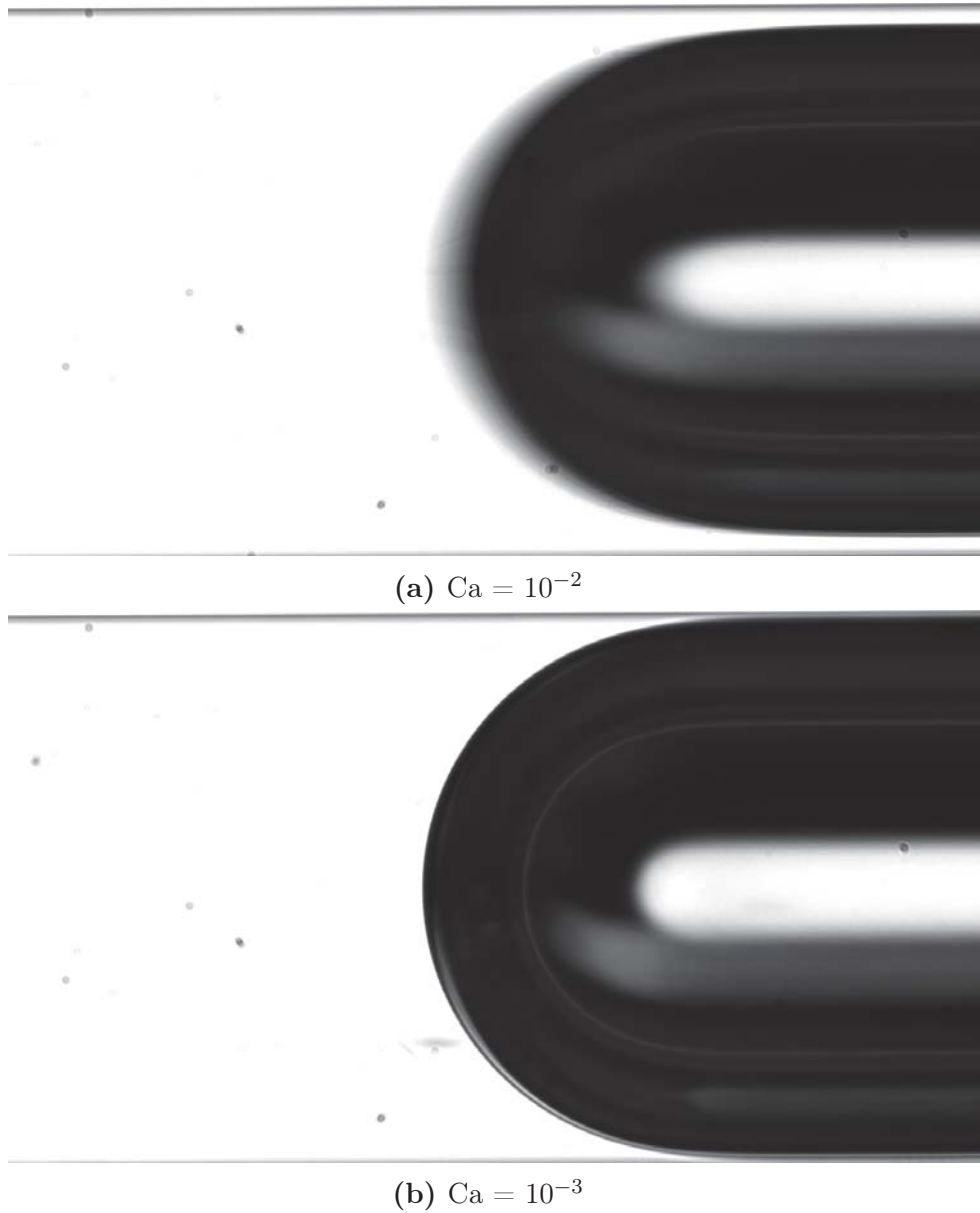


**Figure 5.3.** Centerline images of a moving gas-liquid interface at different  $Ca$  numbers. The gas-liquid interface distorts at  $Ca=10^{-2}$ , determined by the increase in liquid film and blurred interface. Images are formed with transmitted light and an index matched test section.



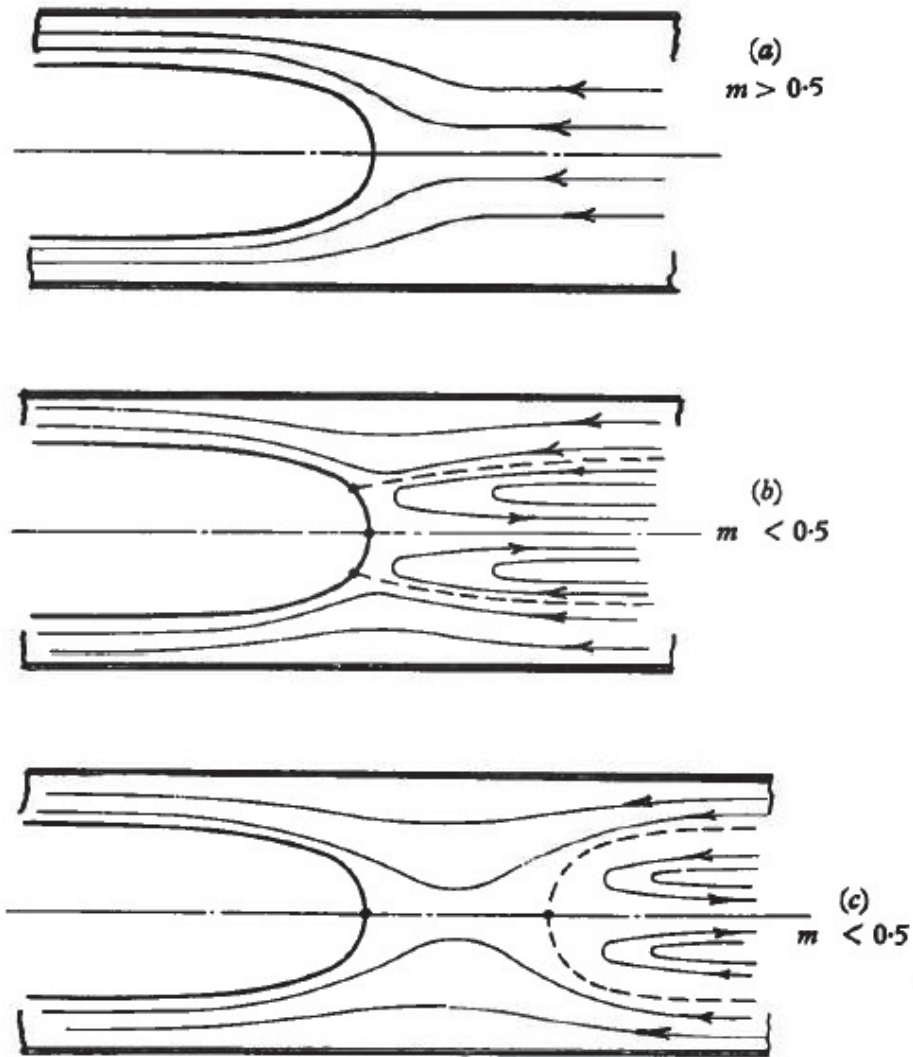


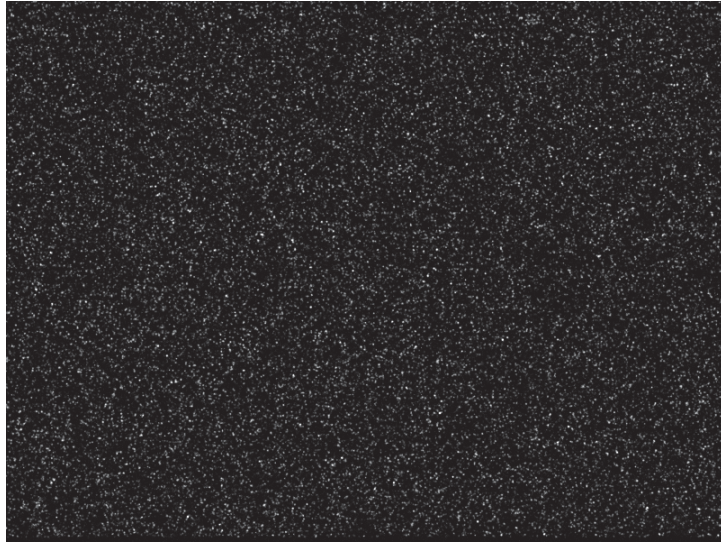
**FIGURE 3.** Rough sketch of possible streamlines.

**Figure 5.4.** Predicted flow profiles within the liquid phase of microscale, gas-liquid two-phase flow,  $m$  is the square root of the  $Ca$  number. Originally published in Taylor [1], used with permission, agreement in Appendix A.3

use small tracer particles to follow the liquid streamlines. Major differences in the techniques include particle density and algorithms for calculating particle velocities. Particle density differences are presented in Figure 5.5. PIV requires large particle densities for accurately measuring velocity vectors using cross-correlation between image pairs. Low particle densities of PTV allow individual tracking particles between frames for velocity measurements.

PIV provides instantaneous measurement of velocity profiles over a short period of time. Multiple image pairs are needed to construct non-steady state fluid dynamics. Velocity vectors are formed by partitioning the image into interrogation windows and performing cross-correlation between matching interrogation windows of an image pair.[64–66] Image pairs are formed by exposing a camera the end of the first frame and beginning of the second, a process termed frame straddling. Generally, a set of pulsed lasers provide the excitation which dramatically reduces particle shift during image acquisition. Particles are illuminated by a planar laser sheet oriented parallel with the image plane.  $\mu$ PIV is the application of PIV in sub-millimeter channels.[66, 67] Particles are excited using either volume illumination by an external laser source or epi-illumination through internal microscope optics. Due to the relative thickness of the illumination volume, out-of-focus (or out of plane) particles are also excited.[68, 69] Excitation out-of-focus particles increases background noise, which decreases the accuracy of cross-correlation.

By detecting and tracking individual particles, PTV physically measures the displacement of individual particles across multiple images.[70–75] Individual particle locations are recorded for each frame either manually or by automated computer algorithms.[70] Particles are linked between frames through a variety of algorithms, such as nearest neighbor and the relaxation method.[71, 74, 76] Accuracy of the link-



(a) PIV Image



(b) PTV Image

**Figure 5.5.** Sample images depicting the difference in particle density between PIV and PTV measurement techniques

ing schemes generally rely on knowing the particles size, location, and maximum displacement. For example, one of the earliest methods for particle tracking is the nearest neighbor linking scheme, depicted in Figure 5.6.[71] Each particle in the second image is given a probability of being the same particle from the first image for each particle within the circle formed by the maximum displacement  $R$ . Velocities are commonly determined by using dividing the linear distance between particle centroids by the time between image frames. A two-frame velocity calculation approach requires a small displacement and time step for accuracy. Other techniques use curve fitting multiple frames for sub-frame accuracy.

Particle tracking velocimetry linked flow fields of segmented flow to decrease the dependency of particle density near the moving interface and within the liquid film. Particles tend to accumulate at the gas-liquid interface resulting in a non-uniform particle spacing and potentially error in the PIV cross-correlation calculations.[49, 77]

Standard widefield images of liquid plugs cannot image near the moving contact line.[49, 75] Reflectance, swept-field confocal particle tracking velocity was developed in order to image particles and measure velocities near the moving meniscus. Confocal microscopy improves the signal to noise ratio of particle images by blocking out-of-focus light by spatially filtering the light through an aperture. Filtered light represent an optical slice or section containing only information from a finite thickness of the test section. A swept-field confocal microscope, uses a slit instead of a circular aperture for spatially filtering the out-of-focus light. The slit improves the speed of image formation and light sensitivity at the expense of optical slice thickness. A complete description of the swept-field confocal microscope is available in Chapter 3. Confocal microscopy has been used for flow visualization of microscale liquid flows. Confocal,  $\mu$ -PIV (CPIV) was performed in previous experiments involving both single and two-

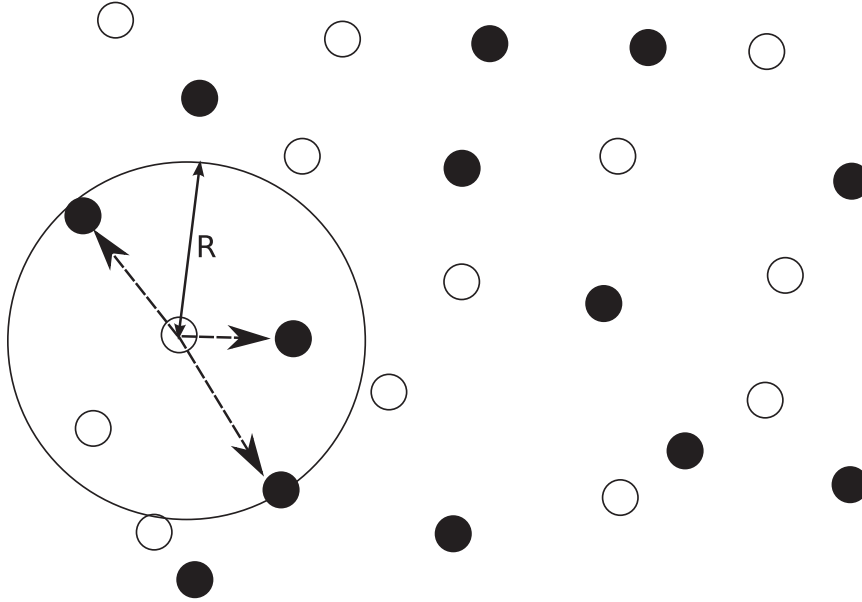


**Figure 5.6.** Individual particle locations of the first frame (hollow particles) are statistically linked to particles in the second image (solid). Particle displacement should be less than the mean distance between particles to reduce the number of linking combinations.

phase, gas-liquid flow.[47–51, 78, 79] Applications of the RSFC are not limited to internal two-phase flow but can be applied to coating and droplet movement, both of which contain similar internal flow patterns.[32, 80–83]

Reflecting particles were used for increased light sensitivity at the image plane. Fluorescence particles are well suited for slow gas/liquid flows due to an increased exposure time on camera sensor. To image faster gas/liquid flows, reflectance particles offer an advantage because the amount of light returning is proportional to excitation light intensity. Fluorescence response has a finite limit of available photon emission. Increasing excitation results in photo bleaching not increased photon emission. To image reflected light, the dichroic mirror in the swept-field confocal microscope was replaced with a 50/50 beam splitter. A deeper discussion on reflectance confocal imaging is found in Chapter 3 and 4.

### 5.3 Experimental Setup

Particle images near a moving meniscus were recorded using the reflectance, swept-field confocal (RSFC) microscope. Images were recorded using a one megapixel (1024 x 1024 px), 10-bit, Photron APX RS high speed camera. Camera frame rates were synchronized with confocal microscope exposure timing using a transistor-transistor-logic (TTL) 3.3 V signal originating from the confocal controller. An additional TTL signal triggered the start of image acquisition. A complete description of the imaging technique is written in Sections 3.3 and 4.2.

Segmented flow was approximated using a single slug propelled by a metal plunger. A liquid plug is deposited into a 490  $\mu$  Drummond Wiretrol round, borosilicate, glass capillary. The glass channel is mounted to a borosilicate slide and surrounded with glycerol. Each test section component had a refractive index (RI) of 1.474, equivalent to the third decimal point. Matching RIs improved the spherical aberrations caused by the various test section geometries. A planar, first interface reduced spurious reflections originating from the outer channel wall. A depth correction was required to adjust the measured depth because the objective was designed for imaging in an air medium. Using a small angle approximation and Snells law, the corrected depth is

$$\delta_{\text{actual}} = \frac{n_{\text{glass}}}{n_{\text{obj}}} \delta_{\text{measured}} \quad (5.1)$$

the actual depth,  $\delta_{\text{actual}}$ , is a function of the measured depth,  $\delta_{\text{measured}}$ , and the index of refraction of the objective medium,  $n_{\text{obj}}$ , and the test section,  $n_{\text{glass}}$ . The objective medium is air, resulting in final depth correction of 1.474  $\delta_{\text{measured}}$ . Ethylene glycol (RI=1.439) and glycerol (RI=1.474) were the working fluids, glycerol provided a

completely index matched test section. Reflecting particle  $4\mu\text{m}$  in diameter (TSI Inc.) were excited with a 488 nm or 643 nm laser and imaged using the 10x, 0.25 NA long working distance (LWD) objective.

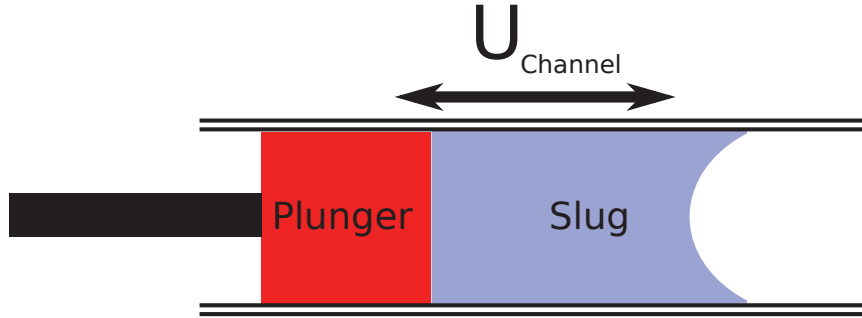


**Figure 5.7.** A plug within a microchannel is under a constant flow rate condition when the stage is moved relative to a stationary plunger.

A plunger pushed/pulled the liquid plug at a constant velocity, which maintained the constant flow rate condition. The plunger was rigidly attached to the objective frame of reference, while the test section traveled at the given speed. A schematic of the plunger and liquid plug assembly is provided in Figure 5.7. As the stage moved, the meniscus remained stationary relative to the microscope objective. Between images changes in the liquid meniscus are negligible but over the entire test run the movement in the frame of reference is significant. Liquid plugs decreased in size as thin films were deposited on the channel wall. The thickness of the deposited film is dependent on the Capillary number.[34] Changes in plug length were neglected for the preliminary data because PTV tracking was limited to a small succession of images.

### 5.3.1 Method of Particle Tracking

Particle tracking is performed using a standard three step process of: 1) Image enhancement, 2) particle detection, and 3) statistical linking of particles between frames.

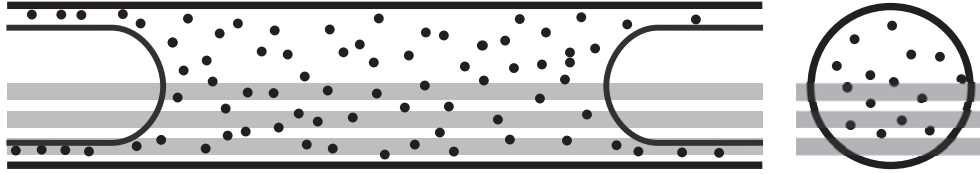


**Figure 5.8.** Confocal microscopy images particles with a finite optical slice thickness. Standard illumination is larger than the area-of-interest, increasing noise and decreasing velocity measurement accuracy. Horizontal lines represent depth that images were imaged.

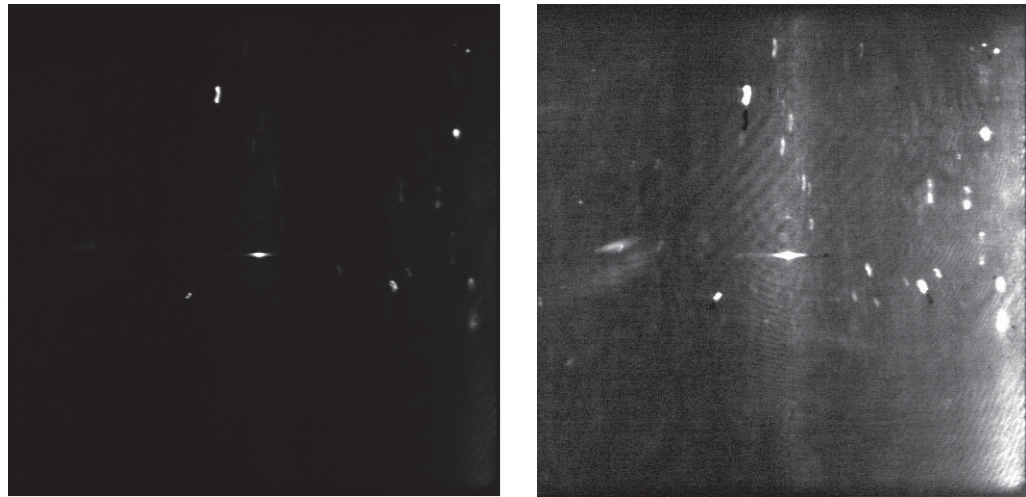
Operations were performed with MatLab using custom and open source algorithms. A variety of operations were performed on imported images for increased particle detection accuracy. Images were cropped to a desired area of interest(AOI) to remove non-essential image information. A segmentation filter removed the background noise, values of one or zero were assigned to pixels relative to a cutoff intensity. The segmented, intensity mask was applied to the original image for a final image with zero background and original intensity distribution for each particle. Initial particle locations were predetermined by grouped, interconnected pixels representative of individual particles. Centerpoint locations were approximated with a Gaussian intensity distribution for the particle intensity.

A nearest neighbor algorithm linked particles between frames.[71] Maximum particle displacement was measured by hand for each image set. Particle diameters and image scale were consistent between test runs. Velocities were calculated by dividing the measured particle displacement by the time between frames.



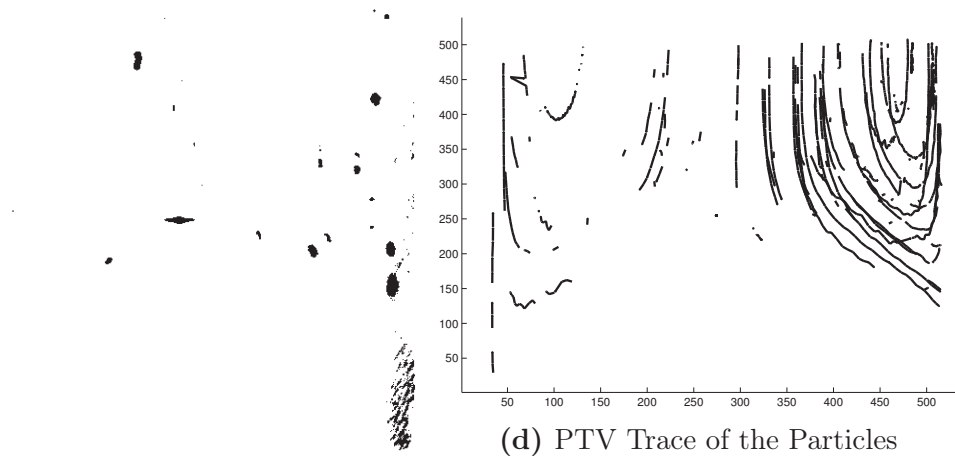
## 5.4 Flow Fields at the Centerline

Images of particles near a moving meniscus at the center line were recorded using the RSFC experimental setup. Ethylene glycol was the working fluid, surface tension was 47.7 mN/m and viscosity was 0.0178 kg/ms. Internal flow fields for an advancing meniscus at Ca numbers of  $4.5 \times 10^{-4}$  and  $9.1 \times 10^{-5}$  are presented in Figures 5.9 and 5.10, respectively. The menisci are slightly visible in both confocal particle images and was more evident in Figure 5.10a. Circulation at the meniscus are visible in both figures. This corroborated previously reported tread-like flow profiles.[49, 62, 84] Particle images recorded flow fields at the liquid meniscus which validated the ability of the RSFC technique for measuring near a curved, gas-liquid interface. The flow fields for the advancing meniscus do not contain information beyond the meniscus's axial location in the gas phase because the channels were dry.



(a) Original Image

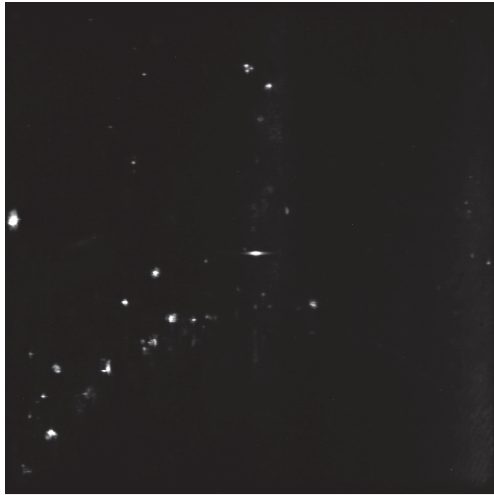
(b) Brightened Image



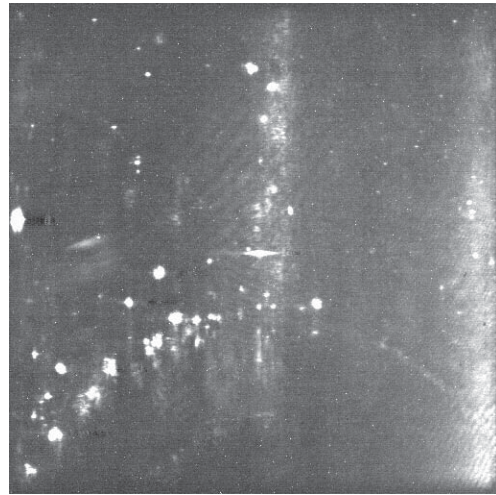
(c) Inverted Image

(d) PTV Trace of the Particles

**Figure 5.9.** Trace of a  $4\ \mu\text{m}$  reflective particles in a  $490\ \mu\text{m}$  round channel, under constant displacement advancing meniscus. The Ca number of the ethylene glycol is  $4.5 \times 10^{-4}$ . The raw image has been cropped, filtered, and inverted for better particle visualization. Images are  $490\ \mu\text{m}$  wide.



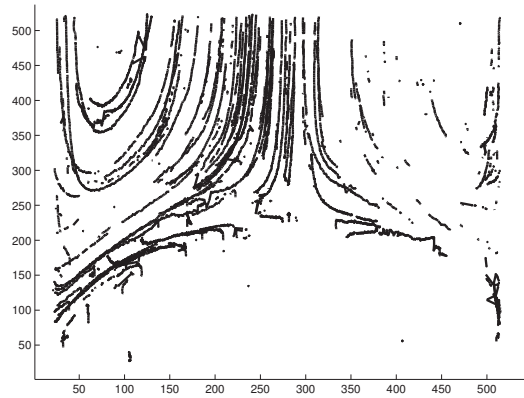
(a) Original Image



(b) Brightened Image



(c) Inverted Image

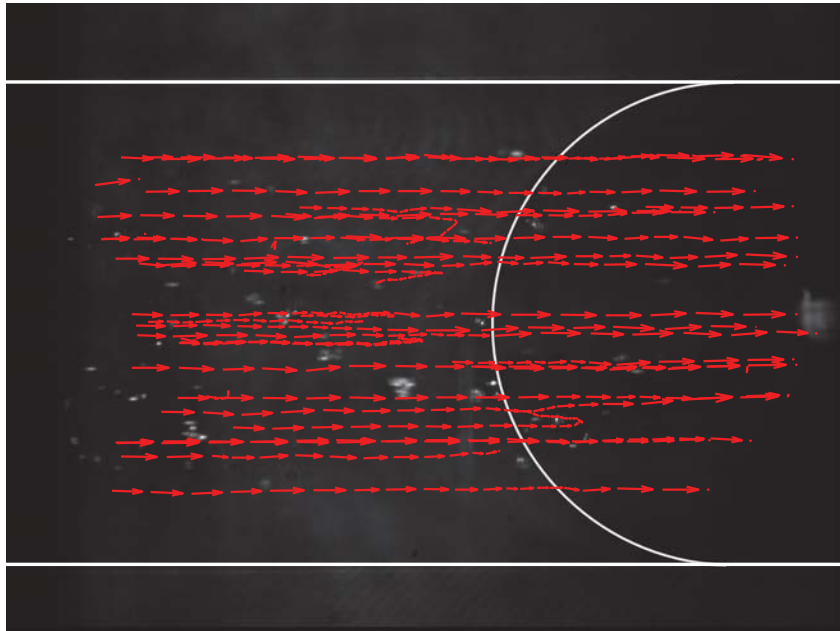


(d) PTV Trace of the Particles

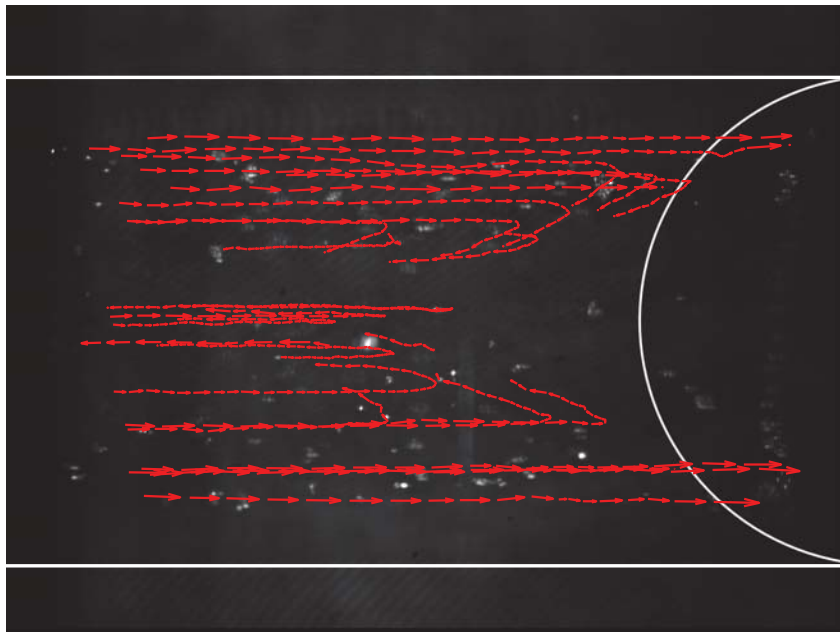
**Figure 5.10.** Trace of a  $4\ \mu\text{m}$  reflective particles in a  $490\ \mu\text{m}$  round channel, under constant displacement advancing meniscus. The Ca number of the ethylene glycol is  $9.1 \times 10^{-5}$ . The raw image has been cropped, filtered, and inverted for better particle visualization. Images are  $490\ \mu\text{m}$  wide

## 5.5 Flow Fields at Three Focal Depths

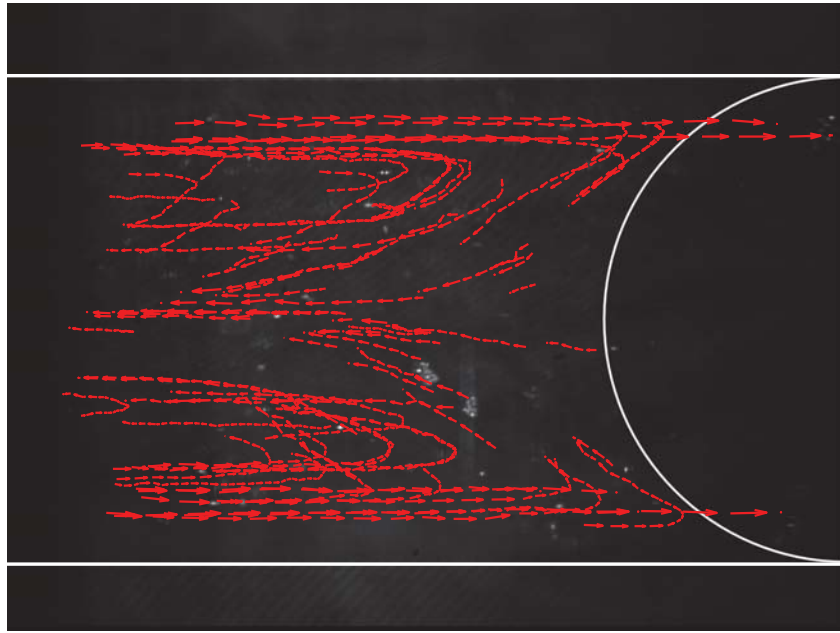
Flow fields of a single receding meniscus were measured at three optical slice locations using the RSFC imaging technique. Focal depths of 50, 100, 150  $\mu\text{m}$  were selected. Actual depths were approximately 75, 150, 225  $\mu\text{m}$  when accounting for the change in index of refraction. Measured flow fields are superimposed over the original image to highlight the particle displacement relative to the liquid meniscus. Near the channel wall, 75  $\mu\text{m}$ , flow fields measured the liquid velocity in deposited liquid film. Only a few particle paths are seen bending for circulation. At 150 $\mu\text{m}$  distance from the channel wall circulation is seen. Flow in the liquid film is seen on the outer edges of the glass capillary accounting for liquid deposition. At 225  $\mu\text{m}$ , near the centerline, the circulation is more pronounced than at 150 $\mu\text{m}$ . The ability to optically slice a liquid plug was demonstrated. Three dimensional flow field measurements are possible if finer step sizes between focal depths are used.



(a)  $75 \mu\text{m}$



(b)  $150 \mu\text{m}$



(c) 225  $\mu\text{m}$

**Figure 5.11.** Flow fields measured at different optical slice depths (a) 75 $\mu\text{m}$  (b) 150 $\mu\text{m}$  (c) 225 $\mu\text{m}$  relative to the bottom channel surface. Glycerol plug within a 490 $\mu\text{m}$  diameter channel being withdrawn at  $\text{Ca}=5.379\times 10^{-3}$ .

## 5.6 Combined Image Information

A single image presented in Figure 5.12 captured reflected light from particles, reflections from the gas-liquid interface and interference patterns caused by changes in film thickness near a particle and transition from flat film to meniscus. Interfacial reflections were used to measure liquid film thicknesses using the RSFC, see Chapter 4 and liquid surface morphology, see Chapter 6. Particles are suspended in both the liquid plug and the liquid film deposited by a receding liquid meniscus of glycerol at a  $Ca=5.379\times 10^{-3}$ . The RSFC imaging technique was capable of simultaneous measurement of particle images, liquid film measurements, and interfacial morphology measurements.

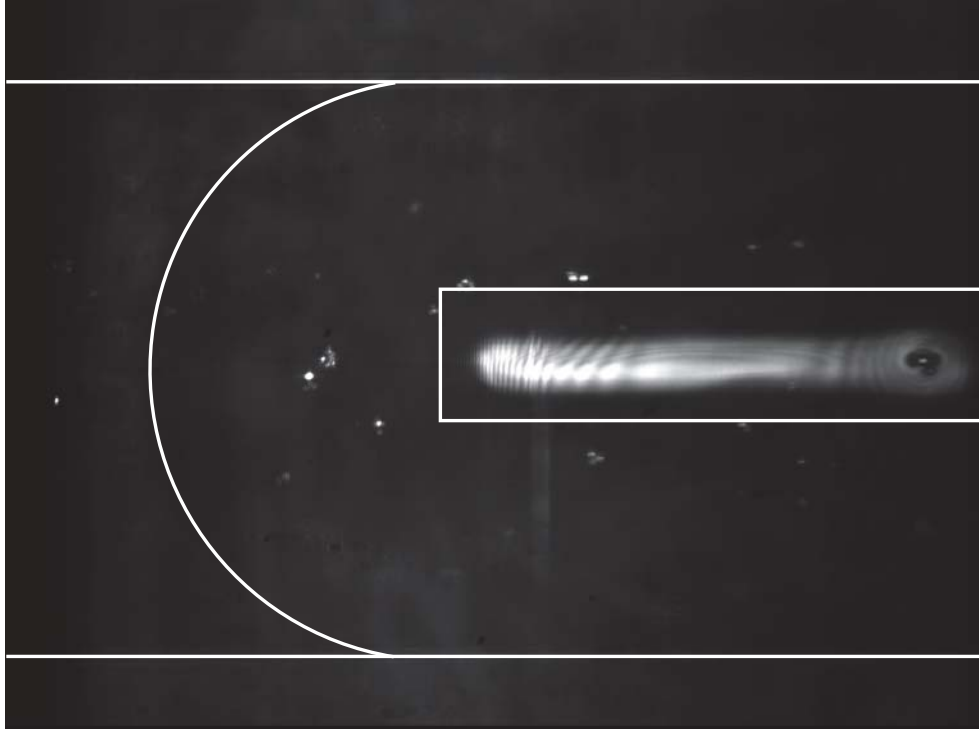


**Figure 5.12.** Single image from the Figure 5.11a data set. A plug of glycerol with  $4\mu\text{m}$  reflective particles near a moving meniscus imaged at  $75\ \mu\text{m}$  relative to the channel wall. The image contains particle reflections in the liquid phase and interference patterns caused by the change in liquid film thickness. Interference patterns are formed near the transition from flat film to meniscus and near a cluster of trapped particles.



## 5.7 Conclusions

Flow fields were measured at the centerline of an advancing liquid plug at two Capillary numbers using reflectance, swept-field confocal imaging and particle tracking velocimetry. Circulation and particle velocities near the meniscus were measured, qualitatively matching similar flow fields measured in previous research. The RSFC imaging technique was validated for measuring flow fields near a curved gas-liquid interface.

Particle images were recorded at three different focal depths near a receding meniscus. Optical slicing of a liquid plug removed the out-of-focus information from the plane of interest. Flow fields were unique at each focal depth. Flow within the deposited liquid film was measured near the wall. Circulation of different magnitudes were measured at the centerline and between the centerline and wall. The magnitude of circulation was different between focal depths. RSFC imaging was capable of measuring flow fields at different focal depths by optically slicing the liquid plug.

An image was presented which contained particle and interfacial reflections with interference patterns in the liquid film. Particle tracking velocimetry, liquid film thickness, and interfacial morphology can be used in combination during a single experiment. Combination imaging will provided a method for liquid behavior during coating and two-phase flows.

# 6. INTERFACIAL MORPHOLOGY

## MEASUREMENT WITH REFLECTANCE, SWEPT-FIELD CONFOCAL INTERFEROGRAMS

### 6.1 Introduction

Direct measurement of gas-liquid interfacial morphology is important for understanding the fundamental physics of liquid coatings, two-phase flow stability, dropwise evaporation and condensation, etc.[32, 34, 35, 83, 85, 86] Morphology of secondary structures on liquid films can affect the stability of gas-liquid two-phase flow. Direct measurement of these secondary flow structures using standard transmitted light techniques is frustrated by the light refracting from the curved gas-liquid interface and test section. Additionally, measured droplet curvature on solid substrates is related to physical properties such as surface tension and contact angle.[87]

Methods for measuring gas-liquid curvatures optically with and without interferometry have been developed using a wide range of imaging techniques.[46, 87–93] Thin films in round channels were measured in millimeter size channels using distances between constructive interference bands.[46] Confocal reflection intensity and

holographic interference patterns were able to measure macroscale, liquid film thickness and interfacial profiles of droplet impingement on a planar surface, the droplet flow rate was fast enough for the formation of a continuous liquid film.[90] This technique used a reference beam with an object beam to measure the liquid film profile. Similarly, macroscale thin film profiles were measured using an intensity distribution.[92, 93]

Interference patterns were created and recorded using using the RSFC imaging technique presented in previous chapters. Spacing of constructive and destructive bands are related to the change film thickness between the flat test section and gas-liquid interface. Planar, thin film interferometric analysis applied to the sloped interface demonstrated the ability of RSFC interferograms to measure changes in film thickness. A single interferogram of an image recorded during film thickness measurements, discussed in Chapter 4, measured the change in film thickness from the flat film to the liquid meniscus. Interference patterns originating from evaporating drops, just before complete droplet “dryout”, were analyzed to measure a droplet profile and slope of the gas-liquid interface. Single and two-color RSFC imaging techniques imaged the droplet evaporation. Two-color imaging created interference patterns using two independent monochromatic laser sources which produced unique interference patterns. Analysis of interference patterns created by a sloped coverslip verified that slope interfaces created the interference patterns recorded in the thin film and droplet evaporation tests.

## 6.2 Segmented Flow

RSFC images of liquid film thickness measurements of microscale, segmented two-phase flow contained interference patterns at transition between the flat film and meniscus. The experimental procedure was presented in Chapter 4. Gas bubbles are divided into regions of different geometric relationships depending on the relative, axial location.[34] The region between the meniscus and “flat” liquid film gradually increases in film thickness to match interfacial geometries, presented in Figure 6.1. The interference pattern for the transition between the leading meniscus and flat liquid film of a gas-bubble in segmented flow is presented in Figure 6.2. Images were formed with the RSFC imaging technique, a 20× objective lens and a 488 nm laser. The interference free, left side of the RSFC image represents the flat liquid film. Moving left to right, changes in film thickness are detected as bright bands which begin with large separations and gradually decrease in spacing. The gap spacing was proportional to and increase in film thickness. An intensity profile of the interference pattern along the white line in Figure 6.2 is plotted in Figure 6.3. Peak analysis of the intensity profile measured the distances between detectable peaks.

Changes in film thickness of the liquid film, depicted in Figure 6.2, was approximated using analysis for a planar thin film. Detected interference patterns were formed by the interaction of light reflected from the solid-liquid surface (inner channel wall) and gas-liquid interface (liquid film). The distance between the reflected light paths is determined with the optical path difference. The OPD for a planar thin film is

$$OPD = 2hn_{\text{film}} \cos(\theta_{\text{film}}) \quad (6.1)$$

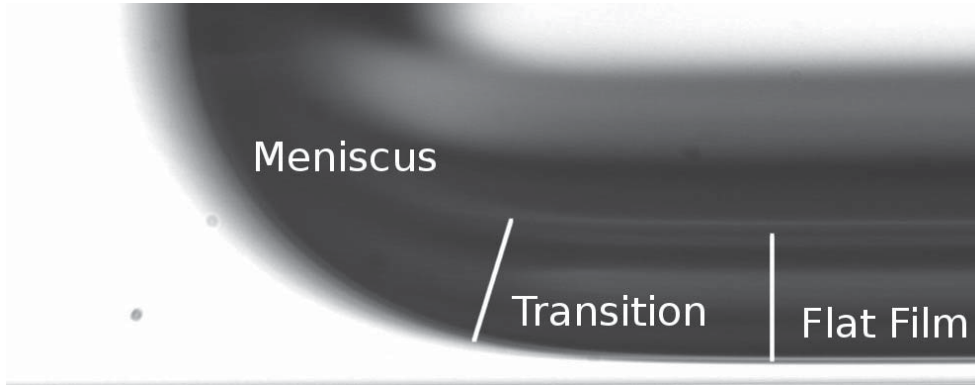


**Figure 6.1.** Simple schematic representing the three regions of an advancing gas-liquid interface; Meniscus, Transition and flat. Film thickness change between flat and meniscus was detected as interference patterns using the RSFC imaging technique.

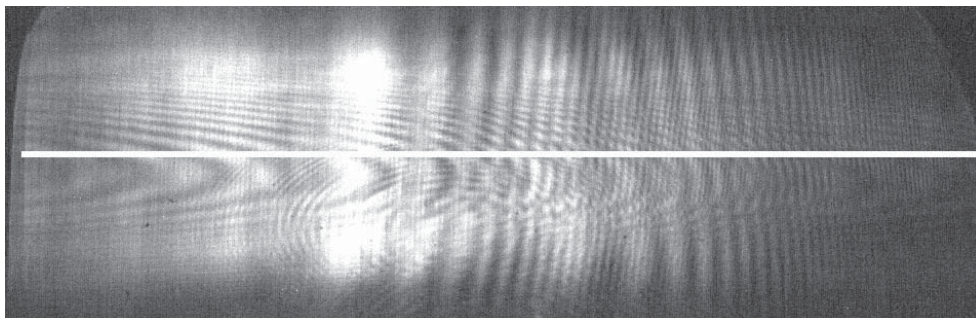


**Figure 6.2.** Interference pattern captured at the transition between flat film and liquid meniscus. An intensity profile along the white line is presented in Figure 6.3

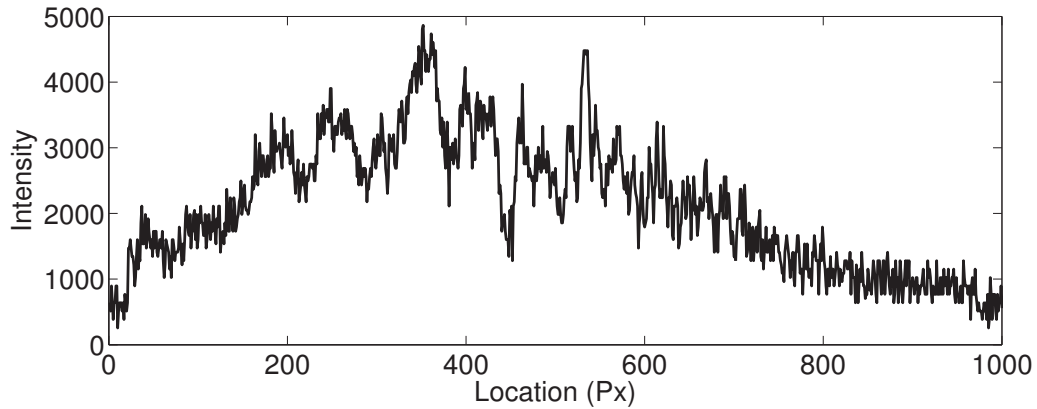


**Figure 6.3.** Image intensity across the length of the white line in Figure 6.2. Distances between peaks approximated the change in film thickness from the flat film to the meniscus.

where  $h$  is the film thickness,  $n$  the refractive index of the film and  $\theta$  is the acceptance angle of the objective within the film. The acceptance angle in the liquid film was determined with Snells law,  $NA = n_{\text{air}} \sin(\theta_{\text{air}}) = n_{\text{film}} \sin(\theta_{\text{film}})$ .

Constructive interference was spaced at  $m\lambda'$ , where  $m$  is the interference band number,  $0, 1, \dots, n$  and  $\lambda'$  is the wavelength of light in the film,  $\lambda' = \lambda/n_{\text{film}}$ . Interference band spacing is dependent on the phase of the reflected light. A phase shift of  $180^\circ$  occurs when light reflects from a transition between low refractive index (RI) and high RI,  $n_1 < n_2$ . The optical path through the test section to the gas-liquid interface was air to glass to liquid to air. Reflections occurred at the air-glass, glass-liquid, and liquid-gas interface. Interference patterns were formed by reflections at the glass-liquid and liquid-air interfaces. A phase shift does not occur because light is reflected from high RI to low RI at each transition.

Combining the constructive interference spacing with the planar, thin film OPD

yields a simple relationship for film thickness.

$$h = \frac{m\lambda_{film}}{2n_{film}\cos(\theta_{film})} \quad (6.2)$$

Film thickness,  $h$ , is a function of interference number,  $m$ , RI of water,  $n_{film}$ , and objective lens acceptance angle in the film,  $\theta_{film}$ .

Changes in Film thicknesses for the liquid film in Figure 6.2 were estimated assuming the first bright,  $m=0$ , occurred at the flat interface. Constructive interference numbers increase from left to right, starting at approximately 200 px in Figure 6.3. Calculated changes in film thickness is presented in Figure 6.4. The slope of the first 3 points is approximately 0.01 or 1% of over the length of the film. This validated the planar film approximation. The slope transitioned to a non-linear profile after the first three interference bands. This increase might be accounted for by the affect of the sloped interface on the interference band spacing. An OPD accounting for the curved surface is required to accurately predict the transition between flat film and meniscus. Initial results demonstrated interferograms of liquid film in segmented two-phase flow are related to the overall flow morphology of the liquid film.

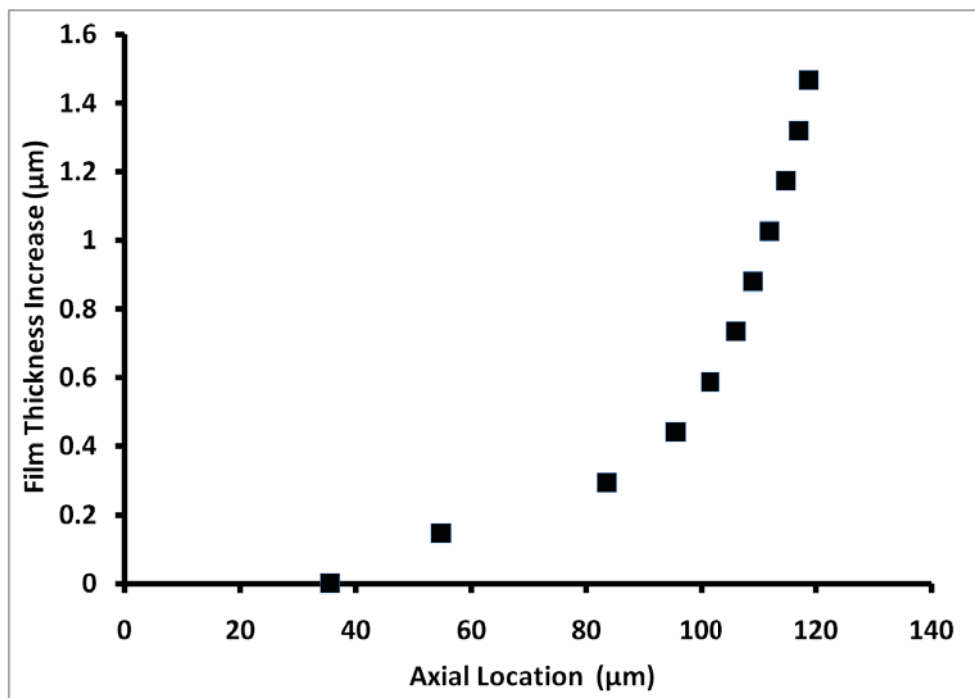
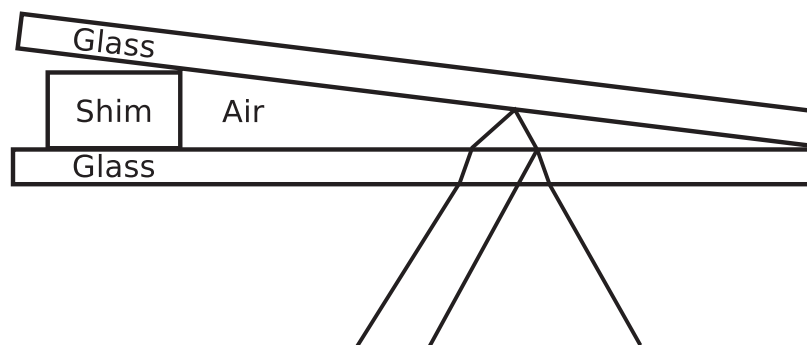


Figure 6.4. Change in film thickness from the flat film to the transition region in segmented flow.

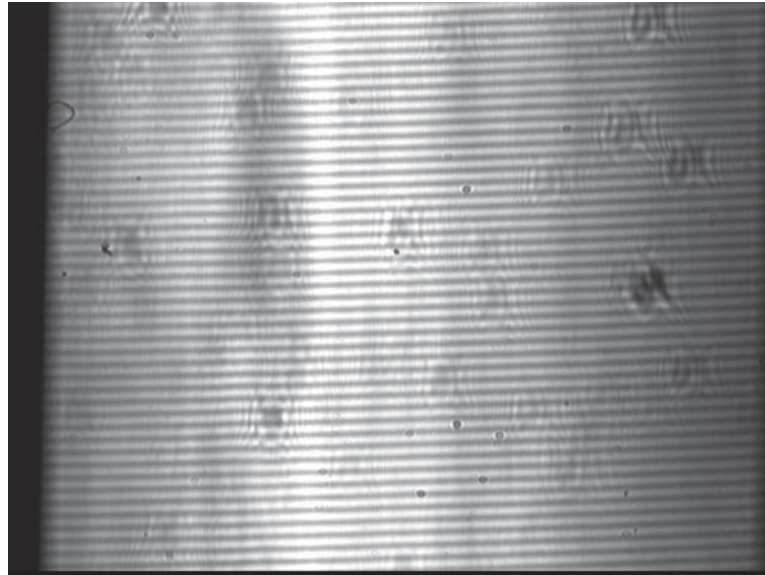


### 6.3 Sloped Interface

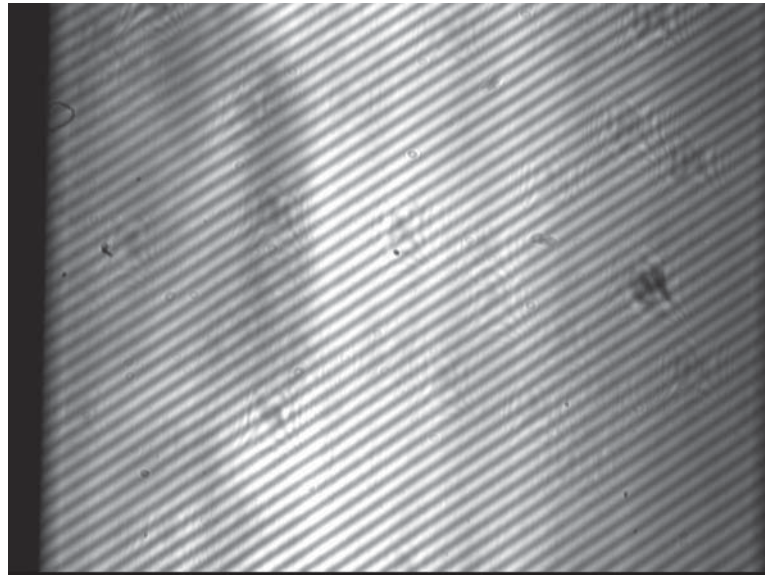
Interference patterns created by a sloped air-glass interface were recorded to corroborate the formation of interference patterns from a sloped gas-liquid interface. Images were recorded using the RSFC imaging technique,  $2\times 0.06$  NA objective and 643 nm laser. The sloped interface was created by a shim sandwiched between two cover slips, as depicted in Figure 6.5. Interference patterns for two different thickness shims are presented in Figure 6.6. Shims were  $80\ \mu\text{m}$  (Green) and  $190\ \mu\text{m}$  (Clear). The thickness of the shims created different coverslip slopes which were qualitatively compared to the distance between interference bands. Direction of the interference pattern was influenced by two-dimensional slope of the top glass cover slip. The rotated interference pattern in Figure 6.6b was a result of a non-uniform shim thickness. The slope of the glass coverslips were calculated through linear regression of the film thicknesses calculated with Equation 6.2 and the constructive interference gap thickness. Calculated gap thicknesses are presented in Figure 6.7. Slopes of the coverslips were  $9\times 10^{-3}$  and  $7\times 10^{-3}\ \mu\text{m}/\mu\text{m}$  for the Clear and Green shims, respectively. Comparison of coverslip slopes and interference band spacing qualitatively proved that interfacial shape was related to interferometric image information.



**Figure 6.5.** Light paths for interference patterns created by a sloped interface. Interference patterns were formed from light reflections at the Glass-Air and Air-Glass interfaces. The slope of the top coverslip is controlled by the thickness and location of the shim.



(a) Clear Shim



(b) Green Shim

**Figure 6.6.** Interference patterns formed by a sloped Air-Glass interface using the experimental setup depicted in Figure 6.5. Slopes were created with shims having thicknesses of (a) Clear  $190\ \mu\text{m}$  and (b) Green  $80\ \mu\text{m}$ . Images were formed using the RSFC imaging technique,  $2\times$  objective NA 0.06, and 643 nm laser. The slopes of the lines are  $9\text{E-}3$  and  $7\text{E-}3\ \mu\text{m}/\mu\text{m}$  for the Clear and Green shims, respectively.

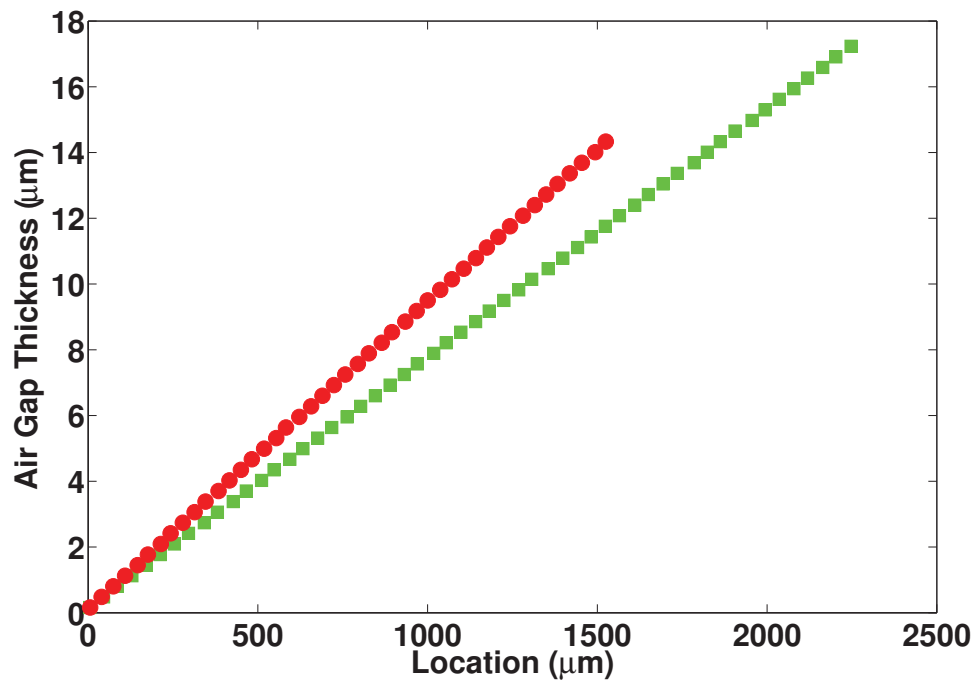


**Figure 6.7.** Film thickness measurement of the distance between a flat and sloped cover slip depicted in Figure 6.5. Coverslip slopes are related to the thickness of the shim. Red circles represent a Clear  $190 \mu\text{m}$  shim and a Green boxes represent Green  $80 \mu\text{m}$  shim

## 6.4 Monochromatic Imaging of Droplet Evaporation

RSFC images of an evaporating droplet of distilled water is presented in Figure 6.8. Images were taken with a  $2\times$ , 0.06 NA objective lens and 643 nm laser. During evaporation, images of the droplet may contain a variety of interference patterns. Initial images may not contain interference patterns depending on the height of the droplet. Once thin enough, concentric interference bands with a single or multiple radii of curvature are possible. During final stages of evaporation, interference patterns are no longer concentric.

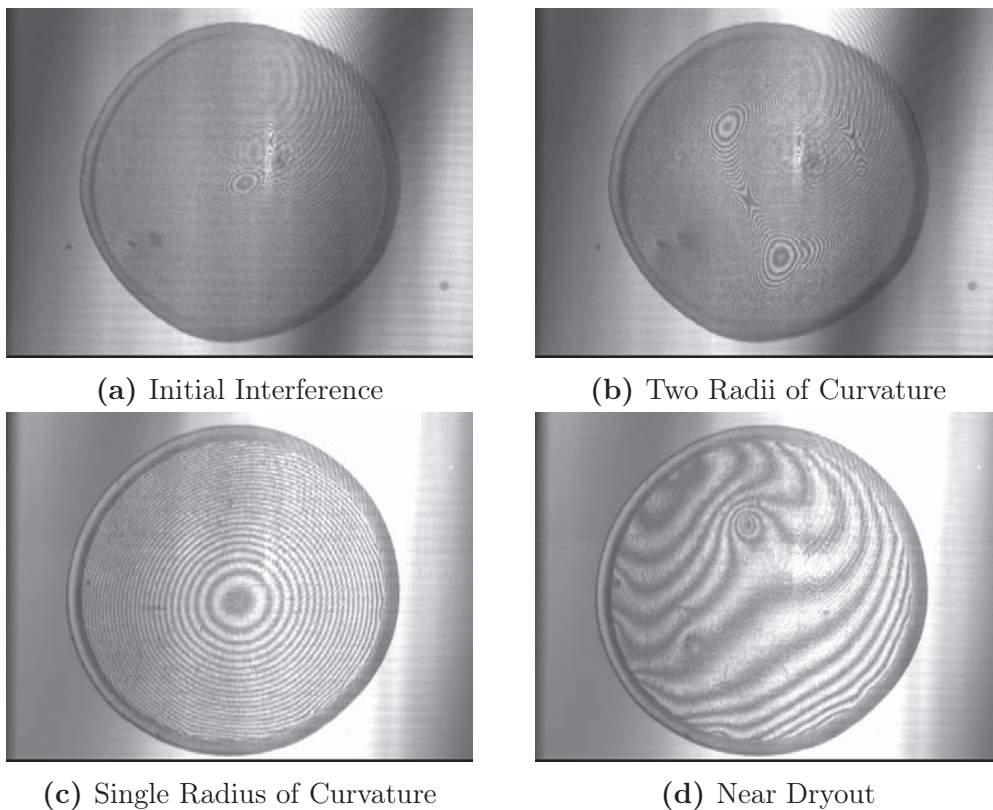
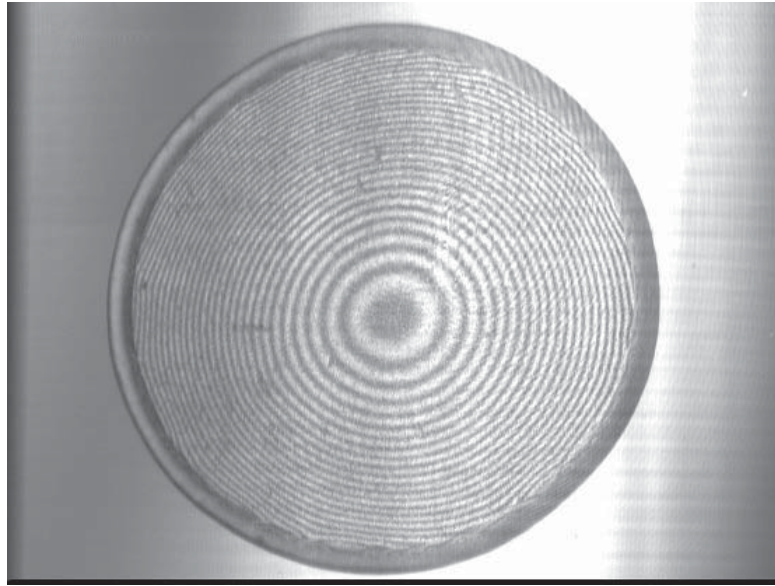


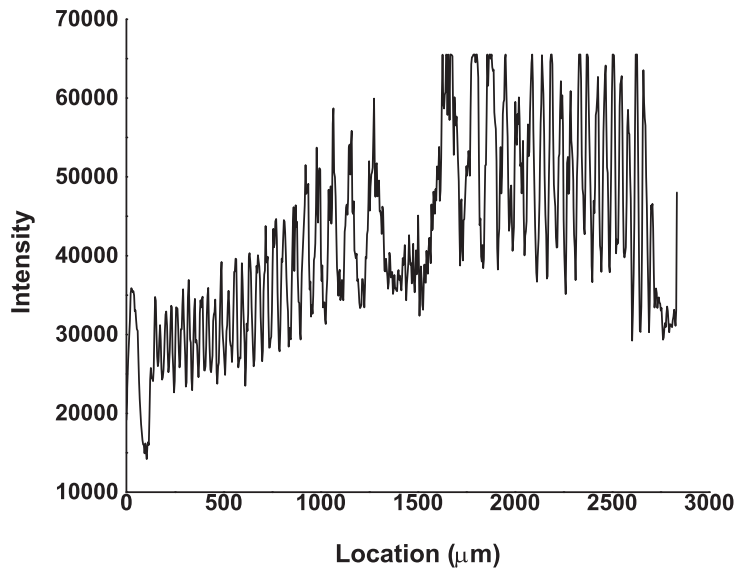
**Figure 6.8.** Droplet images representing different stages of evaporation. Images were taken with a  $2\times$ , 0.06NA objective lens and 643 nm laser. Drop diameters are approximately 2.8 mm.

To test the RSFC's ability to measure droplet shapes, a droplet with concentric interference patterns was analyzed. Figure 6.9 presents the image of the droplet with the interference pattern and the centerline intensity profile across the center of the drop. The droplet has narrow spacing between interference bands at the maximum radius, which increased in spacing moving closer to the drop center. An expansion of the interference band thickness represented a non-linear change in interfacial shape. Additionally, a thicker dark band on the outside of the liquid droplet represented a region which was too thin to measure with the combination of objective lens and laser wavelength.

Distances between constructive interference bands were measured using the intensity profile plotted in Figure 6.9b. Equation 6.2 predicts the change in film thickness for the left-side of the droplet. Calculations were relative to the outside radius of the droplet. The droplet profile resulting from the calculated film thickness is plotted Figure 6.10. The shape of the droplet was clearly captured using this technique. A curvature based OPD is required to increase the accuracy of the film thickness calculation. Accuracy can also be improved by incorporating droplet height and profile measurements to corroborate the droplet geometry. Additional experimental data using the RSFC imaging technique on evaporating droplets are presented in Lee Roy et al. [94] and Shin et al. [95] but without interference profile analysis.



(a) Droplet



(b) Intensity Profile

**Figure 6.9.** (a) Interference pattern formed in an evaporating droplet of distilled water on a borosilicate coverslip. (b) Pixel intensity profile across the centerline of the droplet.

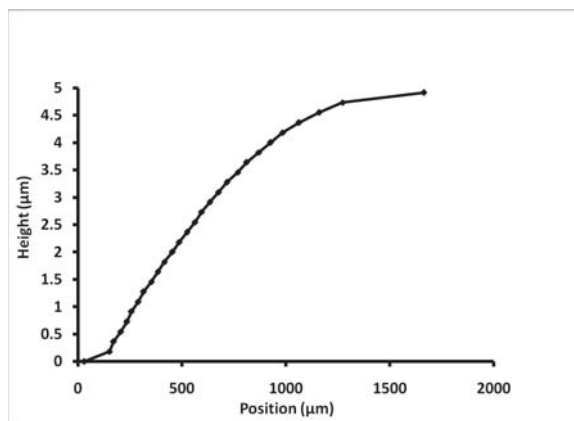


**Figure 6.10.** Shape of the evaporating droplet.

#### 6.4.1 Two-Color Droplet Evaporation

A second method for imaging interference patterns in evaporating droplets with the RSFC technique utilized a two-color excitation technique. Basic two-color imaging uses two monochromatic light sources to illuminate the sample with different excitation wavelengths. Emission wavelengths are not equal and pass through band pass filters separating the color channels. Wavelengths are chosen based on available fluorescent dyes and filter sets. For example, two-color imaging techniques have been successfully used for visualizing flow using PIV, PTV, and LIF.[51, 96–100]

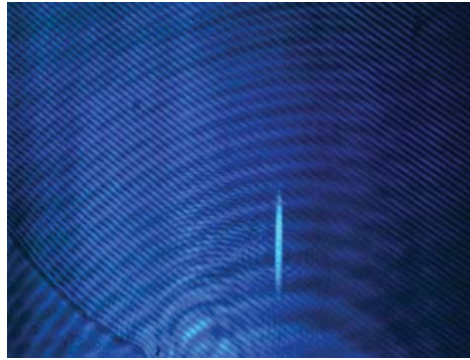
Images are generally recorded one of two ways. Using two monochromatic camera sensors excited by filtered emission light or exciting a single color camera chip.[51, 96] Multiple camera techniques suffer from complex alignment procedures required for accurate pixel to pixel correlations. A single color sensor suffers from decreased resolution caused by a Bayer pixel layout. A Bayer color sensor groups pixels in sets of four, 1 blue, 1 red and 2 green. This has the same affect on image resolution as 2x2 binning of a monochromatic sensor. To mitigate resolution and alignment uncertainty, a JAI AT-200 GE three sensor color camera was used during the two-



color droplet evaporation experiments. Two prisms filter the light base on red, green, and blue light to individual sensors. Sensors are aligned within a  $1/4$  pixel of the green sensor, resulting in a maximum  $1/2$  pixel shift between red and blue sensors.

A series of color image sets of droplet evaporation near the contact line are presented in Figure 6.11. Images were recorded with a  $20\times$ , 0.45 NA objective lens and 488 and 643 nm lasers. Lasers illuminated alternately every other camera exposure due to limitations in the RSFC laser launch. Image sets represent an arbitrary chosen time in evaporation to demonstrate the increased spacing of interference patterns as evaporation time increased. Time of evaporation increases from set 1 to set 3, images are chosen arbitrarily to demonstrate the technique. Thicknesses between interference bands increased as evaporation time increased, indicating a thinning of the droplet. Distances between constructive interference were measured using intensity profiles similar to Figure 6.12.

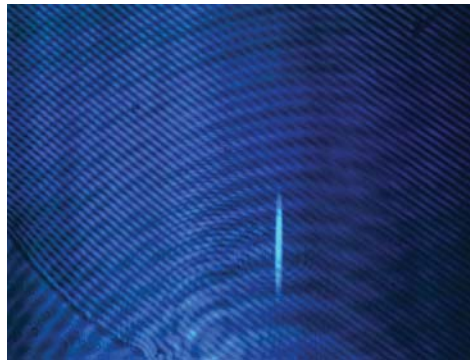
Film thicknesses for each set of interference patterns were approximated using the intensity profiles of the red images. The blue images contain additional interference patterns superimposed over the interference from the gas-liquid interface. The secondary interference patterns decreased the accuracy of the measurement technique with increased uncertainty in the location of the constructive interference bands. Film thicknesses of each set along the radius of the droplet are presented in Figure 6.13a. The film thicknesses begins from the outer most radius of the droplet. Slopes of the gas-liquid interface decreased with increased in gap distances. This result is expected because the interfacial shape should flatten out during increased evaporation time. A comparison of measured film thicknesses using both the blue and red lasers is presented in Figure 6.13b. Measured film thicknesses using the two-color imaging technique match. Improved accuracy of film thickness measurements



(a) Set 1: Blue



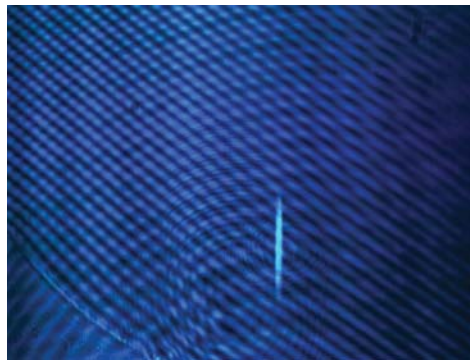
(b) Set 1: Red



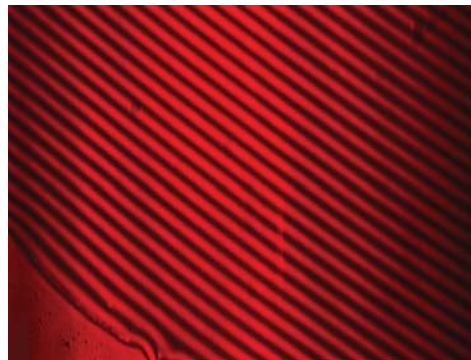
(c) Set 2: Blue



(d) Set 2: Red



(e) Set 3: Blue



(f) Set 3: Red

**Figure 6.11.** Sets represent images taken 1 frame apart, at a frame rate of 1 frame per second, total exposure of 2 fps. Droplets were distilled water on a borosilicate glass slide, imaged with a 20X objective and RSFC microscopy.

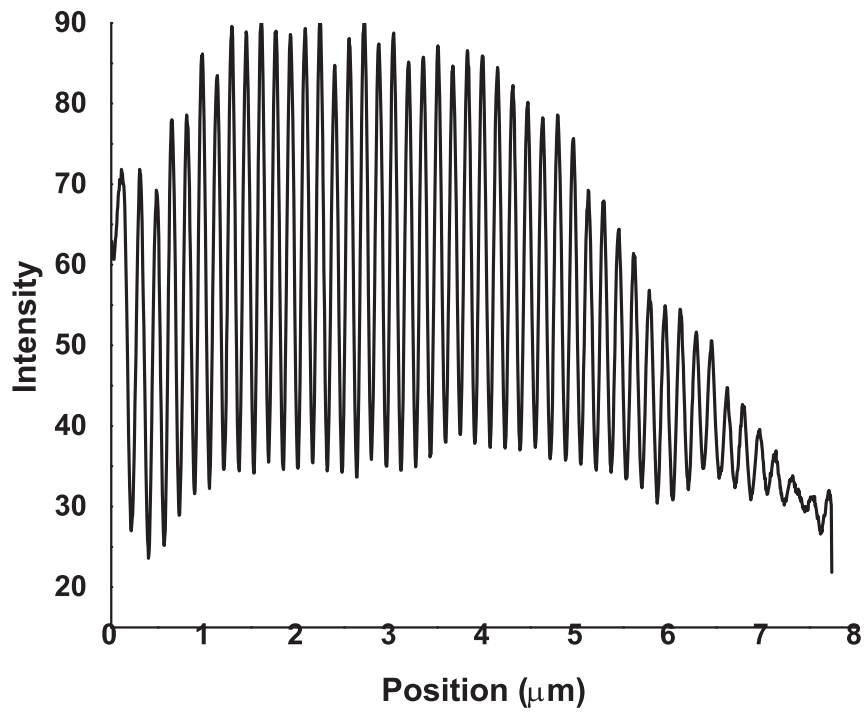
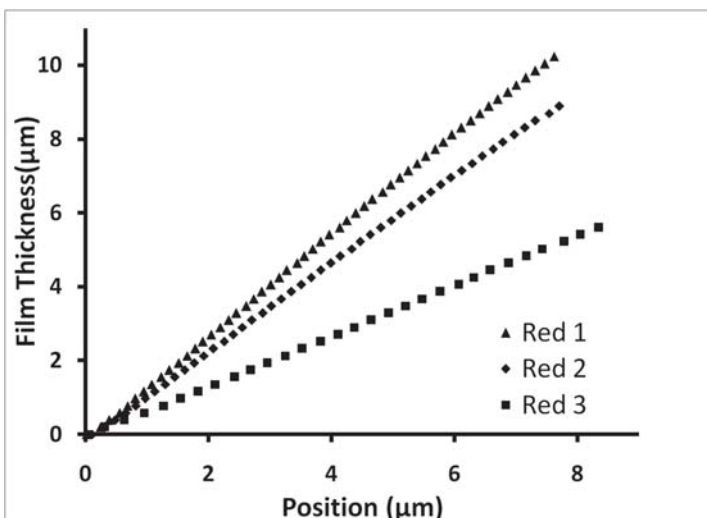
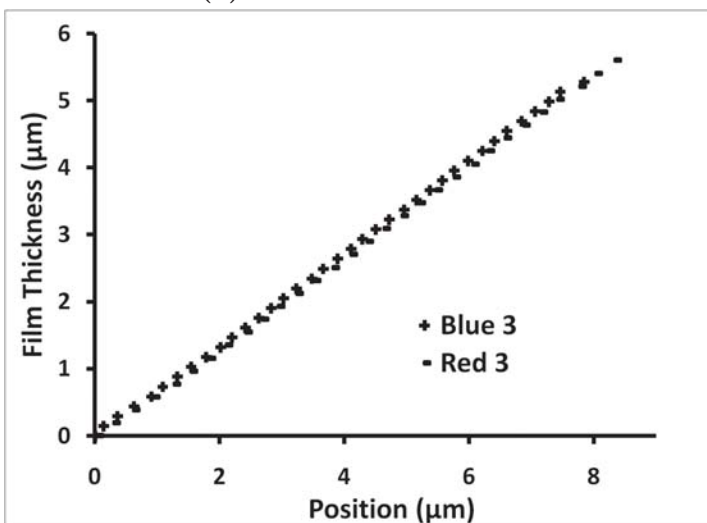


**Figure 6.12.** Intensity profile across a line segment perpendicular to the interference bands.

is expected by combining the solution of both colors. The two-color technique results in sub-wavelength measurement of the film thickness. Similar to the previous techniques, an improved OPD is required to increase the accuracy of the measurement technique.



(a) Combined Red Sets



(b) Blue and Red Comparison

**Figure 6.13.** (a) Film thickness calculations for the red images in Figure 6.11 (b) Comparison of film thicknesses for third set blue and red images

## 6.5 Conclusion

Interference patterns created by sloped gas-liquid interfaces were captured with the RSFC microscopy technique. Preliminary data suggests that analysis of the interference spacing will provide a direct measurement of film thickness profiles. The transition region near a moving meniscus of microscale, segmented, two-phase flow was estimated using planar, thin film interference analysis. The analysis was applied to interference patterns recorded during the final stages of droplet evaporation. Droplet profiles were estimated for whole droplets and magnified contact line regions. Interference patterns formed by a sloped coverslip verified that interference patterns formed during internal two-phase flow and droplet evaporation were created by the sloped gas-liquid interface. Increased accuracy for the the measurement technique requires development of an OPD which accounts for the curved interface.



## 7. CONCLUSIONS

This dissertation focused on the development of imaging techniques for optically measuring dynamic, gas-liquid interfaces and internal liquid fluid dynamics. Three imaging techniques were developed using a reflectance, swept-field confocal (RSFC) microscope. The confocal microscope was purchased, integrated, characterized and modified for imaging reflected light. Multiple pieces of additional hardware was integrated for synchronizing frame rates between the imaging devices and precision alignment of the test section and focal depth.

Liquid film thicknesses were measured using variations in recorded intensities of Fresnel reflections originating from the gas-liquid interface. Reflections were generated and recorded using the RSFC experimental setup. Comparison of peak intensity relative to the focal depth of the objective lens measured the relative liquid film thickness. A correction factor accounting for spherical aberration caused by the test section was developed. The apparent film thickness depth was corrected for the axial and radial components of the optical path. Measured liquid film thicknesses agreed with a classic liquid deposition thickness model. The RSFC film thickness measurement technique can be applied to a variety of internal and external two-phase flow morphologies, including two-phase flow, evaporation, and free surface flows.

Flow fields at the meniscus of a liquid plug were measured at different focal depths



including near the channel wall and the centerline. Reflectance particles were imaged using the RSFC imaging technique. Particle tracking velocimetry linked detected particles between frames and provided the velocity measurements. Internal circulation near the liquid meniscus was measured at the centerline of an advancing plug in a round test section. The flow fields match the predicted and experimentally obtained flow fields reported in literature. Flow fields at three focal depths were measured at a receding meniscus of a liquid plug. Near the wall, flow fields were straight, representative of the velocity within the liquid film. Half way between the wall and the centerline, the circulation was detected as well as the velocity in the liquid film. At the centerline, the flow fields contained fully developed circulation, qualitatively similar to the flow fields in the advancing plug flow. The RSFC imaging technique is capable of imaging near the liquid meniscus or curved interface and measuring flow fields across thin confocal optical slices.

RSFC images near a sloped gas-liquid interface contain interference patterns which are a direct measurement of the interfacial shape. Film thickness profiles for segmented two-phase flow and droplet evaporation were measured by relating film thickness to interference band spacing. Changes in film thickness for a liquid film in segmented two-phase flow was measured using interference patterns formed at the transition between the flat film and the meniscus. Spacing of the interference pattern measured a non-linear film thickness change, which qualitatively matched the interfacial shape recorded in wide field microscopy. Evaporating droplet profiles were measured using monochromatic and two-color RSFC imaging techniques. Whole droplets were imaged using monochromatic light. A droplet profile was generated using the film thickness approximation based on interference gap spacing. Two-color RSFC interference microscopy measured the slope at the outer edge of an evaporating droplet.

Film thickness slopes for three different time periods were calculated. Droplet slope decreased as evaporation time increased. Film thickness measurements for both colors were compared and are in good agreement with one-another.

Reflectance swept-field confocal experimental imaging techniques are capable of independent or simultaneous measurement of microscale, gas-liquid systems. Combined imaging could provide internal flow profiles, liquid film thickness and film morphology during a variety of microscale, fluids experiments. Images were acquired during RSFC PTV tests which contain particle and gas-liquid interfacial reflections. Interference patterns developed near the meniscus and at a trapped particle in the thin liquid film. The RSFC experimental setup has been validated for measuring liquid film thicknesses, flow fields within liquid phases, and gas-liquid interfacial morphology, individually or in combination.

Reflectance swept-field measurement techniques should be applied to a wide range of microscale fluid problems. Currently, RSFC film thickness measurement and interferometry techniques are being applied to liquid deposition in long channels and evaporation of nano-particle-doped distilled water droplets. Parametric studies of annular, unstable, and segmented two-phase flow involving the affects of geometry, wettability, and Ca number can be pursued with the RSFC imaging techniques. Internal flow flow fields and surface morphology during evaporation can be measured simultaneously.



## REFERENCES

- [1] G. I. Taylor. Deposition of a viscous fluid on the wall of a tube. *Journal of Fluid Mechanics*, 10(02):161–165, 1961.
- [2] I. Hassan, M. Vaillancourt, and K. Pehlivan. Two-phase flow regime transitions in microchannels: A comparative experimental study. *Microscale Thermophysical Engineering*, 9(2):165–182, 2005.
- [3] Abdelkader Salim, Mostafa Fourar, Jacques Pironon, and Judith Sausse. Oil-water two-phase flow in microchannels: Flow patterns and pressure drop measurements. *The Canadian Journal of Chemical Engineering*, 86(6):978–988, 2008.
- [4] GF Hewitt. *Measurement of two phase flow parameters*, volume 79. Academic Press, 1978.
- [5] Marvin Minsky. Microscopy apparatus, Dec 1961.
- [6] M. Minsky. Memoir on inventing the confocal scanning microscope. *Scanning*, 10(4):128–138, 1988.
- [7] W. B. Amos, J. G. White, and M. Fordham. Use of confocal imaging in the study of biological structures. *Appl. Opt.*, 26(16):3239–3243, Aug 1987.

- [8] JG White, WB Amos, and M Fordham. An evaluation of confocal versus conventional imaging of biological structures by fluorescence light microscopy. *J. Cell Biol.*, 105(1):41–48, 1987.
- [9] W.B. Amos and J.G. White. How the confocal laser scanning microscope entered biological research. *Biology of the Cell*, 95(6):335–342, 2003.
- [10] Charles J. Koester. Scanning mirror microscope with optical sectioning characteristics: applications in ophthalmology. *Appl. Opt.*, 19(11):1749–1757, Jun 1980.
- [11] Tatsuro Suzuki and Yoshiaki Horikawa. Development of a real-time scanning laser microscope for biological use. *Appl. Opt.*, 25(22):4115–4121, Nov 1986.
- [12] G. J. Brakenhoff, P. Blom, and P. Barends. Confocal scanning light microscopy with high aperture immersion lenses. *Journal of Microscopy*, 117(2):219–232, 1979.
- [13] SHINYA Inoué et al. Imaging of unresolved objects, superresolution, and precision of distance measurement with video microscopy. *Methods Cell Biol*, 30: 85–112, 1989.
- [14] J.B. Pawley. *Handbook of biological confocal microscopy*. Language of science. Springer, 2006. ISBN 9780387259215.
- [15] ErnstH.K. Stelzer. The intermediate optical system of laser-scanning confocal microscopes. In James B. Pawley, editor, *Handbook Of Biological Confocal Microscopy*, pages 207–220. Springer US, 2006. ISBN 978-0-387-25921-5.

- [16] Derek Toomre and James B. Pawley. Disk-scanning confocal microscopy. In James B. Pawley, editor, *Handbook Of Biological Confocal Microscopy*, pages 221–238. Springer US, 2006. ISBN 978-0-387-25921-5.
- [17] Jae Sung Park, Chang Kyoung Choi, and Kenneth D. Kihm. Optically sliced micro-piv using confocal laser scanning microscopy (clsm). *Experiments in Fluids*, 37(1):105–119, July 2004.
- [18] Alan R. Hibbs, Glen MacDonald, and Karl Garsha. Practical confocal microscopy. In James B. Pawley, editor, *Handbook Of Biological Confocal Microscopy*, pages 650–671. Springer US, 2006. ISBN 978-0-387-25921-5.
- [19] G. J. Brakenhoff. Imaging modes in confocal scanning light microscopy (cslm). *Journal of Microscopy*, 117(2):233–242, 1979.
- [20] G. S. Kino, T. R. Corle, and G. Q. Xiao. New types of scanning optical microscopes, 1988.
- [21] SW Paddock. Tandem scanning reflected-light microscopy of cell-substratum adhesions and stress fibres in swiss 3t3 cells. *J Cell Sci*, 93(1):143–146, 1989.
- [22] Akira ICHIHARA, Takeo TANAAMI, Katsumi ISOZAKI, Yumiko SUGIYAMA, Yasuhito KOSUGI, Kenta MIKURIYA, Michio ABE, and Isao UEMURA. High-speed confocal fluorescence microscopy using a nipkow scanner with microlenses for 3-d imaging of single fluorescent molecule in real time. *Bioimages*, 4(2):57–62, 1996.
- [23] R. Ho and Z. Shao. Axial resolution of confocal microscopes revisited. *Optik*, 88(4):147–154, 1991.

- [24] W. Galbraith. The optical measurement of depth. *Quarterly Journal of Microscopical Science*, s3-96(35):285–288, 1955.
- [25] Richard L. Hoffman. A study of the advancing interface. i. interface shape in liquid–gas systems. *Journal of Colloid and Interface Science*, 50(2):228 – 241, 1975.
- [26] A. Lipson, S.G. Lipson, and H. Lipson. *Optical Physics*. Cambridge University Press, 2010. ISBN 9780521493451.
- [27] M. Richter, P. Woias, and D. Weiß. Microchannels for applications in liquid dosing and flow-rate measurement. *Sensors and Actuators A: Physical*, 62(1-3): 480 – 483, 1997. Proceedings of Eurosensors X.
- [28] H.A. Stone, A.D. Stroock, and A. Ajdari. Engineering flows in small devices. *Annual Review of Fluid Mechanics*, 36(1):381–411, January 2004.
- [29] Volker Hessel, Holger Löwe, and Friedhelm Schönfeld. Micromixers—a review on passive and active mixing principles. *Chemical Engineering Science*, 60(8-9):2479 – 2501, 2005. 5th International Symposium on Mixing in Industrial Processes (ISMIP5).
- [30] N.T. Nguyen and S.T. Wereley. *Fundamentals and applications of microfluidics*. Artech House Publishers, 2006.
- [31] Aurthur E. Bergles. United States Activity in Two-Phase Flow. In Aurthur E. Bergles and Seiken Ishigai, editors, *Two-Phase Flow Dynamics*, pages 43–58. Hemisphere Publishing Corporation, Washington, 1981.

- [32] E B Dussan. On the spreading of liquids on solid surfaces: Static and dynamic contact lines. *Annual Review of Fluid Mechanics*, 11(1):371–400, 1979.
- [33] Fred Fairbrother and Alfred E. Stubbs. 119. studies in electro-endosmosis. part vi. the "bubble-tube" method of measurement. *J. Chem. Soc.*, pages 527–529, 1935.
- [34] FP Bretherton. The motion of long bubbles in tubes. *Journal of Fluid Mechanics*, 10(02):166–188, 1961.
- [35] Pascale Aussillous and David Quéré. Quick deposition of a fluid on the wall of a tube. *Physics of Fluids*, 12(10):2367–2371, 2000.
- [36] P.S. Hammond. Nonlinear adjustment of a thin annular film of viscous fluid surrounding a thread of another within a circular cylindrical pipe. *J. Fluid Mechanics*, 137:363–384, 1983.
- [37] R. W. Aul and W. L. Olbricht. Stability of a thin annular film in pressure-driven, low-Reynolds-number flow through a capillary. *J. Fluid Mechanics*, 215:585–599, 1990.
- [38] Cristiano Bigonha Tibiriçá, Francisco Júlio do Nascimento, and Gherhardt Ribatski. Film thickness measurement techniques applied to micro-scale two-phase flow systems. *Experimental Thermal and Fluid Science*, 34(4):463 – 473, 2010. ECI International Conference on Heat Transfer and Fluid Flow in Microscale.
- [39] G. F. Hewitt. Disturbance waves in annular two-phase flow. In *ARCHIVE: Proceedings of the Institution of Mechanical Engineers, Conference Proceedings*



1964-1970 (vols 178-184), Various titles labelled Volumes A to S, volume 184, pages 142–150. Professional Engineering Publishing - Archive, 1969.

- [40] E.T. Hurlburt and T.A. Newell. Optical measurement of liquid film thickness and wave velocity in liquid film flows. *Experiments in Fluids*, 21(5):357–362, 1996.
- [41] Tomoji Takamasa and Kenji Kobayashi. Measuring interfacial waves on film flowing down tube inner wall using laser focus displacement meter. *International Journal of Multiphase Flow*, 26(9):1493 – 1507, 2000.
- [42] Tatsuya Hazuku, Norihiro Fukamachi, Tomoji Takamasa, Takashi Hibiki, and Mamoru Ishii. Measurement of liquid film in microchannels using a laser focus displacement meter. *Experiments in Fluids*, 38(6):780–788, 2005.
- [43] Youngbae Han and Naoki Shikazono. Measurement of the liquid film thickness in micro tube slug flow. *International Journal of Heat and Fluid Flow*, 30(5):842 – 853, 2009. <ce:title>The 3rd International Conference on Heat Transfer and Fluid Flow in Microscale</ce:title> <xocs:full-name>The 3rd International Conference on Heat Transfer and Fluid Flow in Microscale</xocs:full-name>.
- [44] Youngbae Han and Naoki Shikazono. Measurement of liquid film thickness in micro square channel. *International Journal of Multiphase Flow*, 35(10):896 – 903, 2009.
- [45] Kenneth Kihm. *Near-field characterization of micro/nano-scaled fluid flows*. Springer, New York, 2011. ISBN 9783642204258.

- [46] Wali M. Nozhat. Measurement of liquid-film thickness by laser interferometry. *Appl. Opt.*, 36(30):7864–7869, Oct 1997.
- [47] Jae Sung Park, Chang Kyoung Choi, and Kenneth D. Kihm. Optically sliced micro-PIV using confocal laser scanning microscopy (CLSM). *Experiments in Fluids*, 37(1):105–119, July 2004.
- [48] Axel GÃijnter, Manish Jhunjhunwala, Martina Thalmann, Martin A. Schmidt, and Klavs F. Jensen. Micromixing of miscible liquids in segmented gas-liquid flow. *Langmuir*, 21(4):1547–1555, February 2005.
- [49] Kelly Black, Bruno Bradford, and Joseph Martel. A preliminary piv and analytical investigation of wall shear in micro channel slug flow. Number IMECE2007-42113, Seattle, Washington, USA, November 2007. ASME International Mechanical Engineering Congress and Exposition, Asme.
- [50] Rui Lima, Shigeo Wada, Ken ichi Tsubota, and Takami Yamaguchi. Confocal micro-piv measurements of three-dimensional profiles of cell suspension flow in a square microchannel. *Measurement Science and Technology*, 17(4):797, 2006.
- [51] M Oishi, H Kinoshita, T Fujii, and M Oshima. Confocal micro-piv measurement of droplet formation in a t-shaped micro-junction. *Journal of Physics: Conference Series*, 147:012061 (9pp), 2009.
- [52] Donata M. Fries, Franz Trachsel, and Philipp Rudolf von Rohr. Segmented gas-liquid flow characterization in rectangular microchannels. *International Journal of Multiphase Flow*, 34(12):1108 – 1118, 2008.

- [53] Milind Rajadhyaksha, Melanie Grossman, Dina Esterowitz, Robert H Webb, and R Rox Anderson. In vivo confocal scanning laser microscopy of human skin: Melanin provides strong contrast. *J Investig Dermatol*, 104(6):946–952, June 1995.
- [54] Milind Rajadhyaksha, Salvador Gonzalez, James M Zavislan, R Rox Anderson, and Robert H Webb. In vivo confocal scanning laser microscopy of human skin ii: Advances in instrumentation and comparison with histology1. *J. Invest Dermatol*, 113(3):293–303, September 1999.
- [55] Jeffrey S. Allen and Sang Young Son. High Speed Microscopic Visualization of Adiabatic Gas-Liquid Flow in Microchannels. In *The Eighteenth International Symposium on Transport Phenomena*, Daejon, Korea, August 27-30 2007.
- [56] Robert Klimek and Ted Wright. *Spotlight’s Image Analysis Software*. Glenn Research Center, Cleveland, Ohio, 21000 Brookpark Road, Cleveland, Ohio, January 2006. NASA/TM-2006-214084.
- [57] Pierre-Gilles Gennes, Françoise Brochard-Wyart, and David Quéré. Hydrodynamics of interfaces: Thin films, waves, and ripples. In *Capillarity and Wetting Phenomena*, pages 107–138. Springer New York, 2004. ISBN 978-1-4419-1833-8.
- [58] Neil J. Everall. Modeling and measuring the effect of refraction on the depth resolution of confocal raman microscopy. *Appl. Spectrosc.*, 54(6):773–782, Jun 2000.
- [59] Sidney A. Self. Focusing of spherical gaussian beams. *Appl. Opt.*, 22(5):658–661, Mar 1983.

- [60] J. Prothero and A.C. Burton. The physics of blood flow in capillaries: I. the nature of the motion. *Biophysical Journal*, 1(7):565 – 579, 1961.
- [61] T. C. Thulasidas, M. A. Abraham, and R. L. Cerro. Flow patterns in liquid slugs during bubble-train flow inside capillaries. *Chemical Engineering Science*, 52(17):2947 – 2962, 1997.
- [62] Colin King, Edmond Walsh, and Ronan Grimes. Piv measurements of flow within plugs in a microchannel. *Microfluidics and Nanofluidics*, 3(4):463–472, August 2007.
- [63] Steven T. Wereley and Carl D. Meinhart. Recent advances in micro-particle image velocimetry. *Annual Review of Fluid Mechanics*, 42(1):557–576, 2010.
- [64] Ronald J. Adrian. Particle-imaging techniques for experimental fluid mechanics. *Annual Review of Fluid Mechanics*, 23(1):261–304, 1991.
- [65] J Westerweel. Fundamentals of digital particle image velocimetry. *Measurement Science and Technology*, 8(12):1379–1392, 1997.
- [66] J. G. Santiago, S. T. Wereley, C. D. Meinhart, D. J. Beebe, and R. J. Adrian. A particle image velocimetry system for microfluidics. *Experiments in Fluids*, 25(4):316–319, September 1998.
- [67] C. D. Meinhart, S. T. Wereley, and J. G. Santiago. Piv measurements of a microchannel flow. *Experiments in Fluids*, 27(5):414–419, October 1999.
- [68] M. G. Olsen and R. J. Adrian. Out-of-focus effects on particle image visibility and correlation in microscopic particle image velocimetry. *Experiments in Fluids*, 29(7):S166–S174, December 2000.

- [69] C D Meinhart, S T Wereley, and M H B Gray. Volume illumination for two-dimensional particle image velocimetry. *Measurement Science and Technology*, 11(6):809–814, 2000.
- [70] A.A. Adamczyk and L. Rimai. 2-dimensional particle tracking velocimetry (ptv): Technique and image processing algorithms. *Experiments in Fluids*, 6(6):373–380, 1988.
- [71] Kazuo Ohmi and Hang-Yu Li. Particle-tracking velocimetry with new algorithms. *Measurement Science and Technology*, 11(6):603–616, 2000.
- [72] I.F. Sbalzarini and P. Koumoutsakos. Feature point tracking and trajectory analysis for video imaging in cell biology. *Journal of Structural Biology*, 151(2):182 – 195, 2005.
- [73] Sang Lee and Seok Kim. Advanced particle-based velocimetry techniques for microscale flows. *Microfluidics and Nanofluidics*, 6(5):577–588, May 2009.
- [74] A V Mikheev and V M Zubitsov. Enhanced particle-tracking velocimetry (eptv) with a combined two-component pair-matching algorithm. *Measurement Science and Technology*, 19(8):085401 (16pp), 2008.
- [75] Rui Luo and Ling Wang. Liquid flow pattern around taylor bubbles in an etched rectangular microchannel. *Chemical Engineering Research and Design*, 90(8):998 – 1010, 2012.
- [76] W. Brevis, Y. Niño, and G.H. Jirka. Integrating cross-correlation and relaxation algorithms for particle tracking velocimetry. *Experiments in Fluids*, 50(1):135–147, 2011.

- [77] Andrea W. Chow, Steven W. Sinton, Joseph H. Iwamiya, and Thomas S. Stephens. Shear-induced particle migration in couette and parallel-plate viscometers: Nmr imaging and stress measurements. *Physics of Fluids*, 6(8):2561–2576, 1994.
- [78] J. S. Park, K. D. Kihm, and J. S. Allen. Three-dimensional microfluidic measurements using optical sectioning by confocal microscopy: Flow around a moving air bubble in a micro-channel. *ASME Conference Proceedings*, 2002(36339): 217–222, 2002.
- [79] Rui Lima, Shigeo Wada, Shuji Tanaka, Motohiro Takeda, Takuji Ishikawa, Ken-ichi Tsubota, Yohsuke Imai, and Takami Yamaguchi. *In vitro* blood flow in a rectangular pdms microchannel: experimental observations using a confocal micro-piv system. *Biomedical Microdevices*, 10(2):153–167, April 2008.
- [80] M.J. Savelski, S.A. Shetty, W.B. Kolb, and R.I. Cerro. Flow patterns associated with the steady movement of a solid/liquid/fluid contact line. *Journal of Colloid and Interface Science* l, 176(1):117 – 127, 1995.
- [81] Ramon L. Cerro. Moving contact lines and langmuir - blodgett film deposition. *Journal of Colloid and Interface Science*, 257(2):276 – 283, 2003.
- [82] Javier Fuentes and Ramon L. Cerro. Flow patterns and interfacial velocities near a moving contact line. *Experiments in Fluids*, 38:503–510, 2005. 10.1007/s00348-005-0941-4.
- [83] E. B. Dussan V. The moving contact line: the slip boundary condition. *Journal of Fluid Mechanics Digital Archive*, 77(04):665–684, 1976.

- [84] M. N. Kashid, I. Gerlach, S. Goetz, J. Franzke, J. F. Acker, F. Platte, D. W. Agar, and S. Turek. Internal circulation within the liquid slugs of a liquid-liquid slug-flow capillary microreactor. *Industrial & Engineering Chemistry Research*, 44(14):5003–5010, July 2005.
- [85] P. G. de Gennes. Wetting: statics and dynamics. *Rev. Mod. Phys.*, 57(3):827–863, Jul 1985.
- [86] A.G. Egorov, K.G. Kornev, and A.V. Neimark. Meniscus motion in a prewetted capillary. *Physics of Fluids*, 15:3134, 2003.
- [87] Pierre-Gilles Gennes, Françoise Brochard-Wyart, and David Quéré. Capillarity and gravity. In *Capillarity and Wetting Phenomena*, pages 33–67. Springer New York, 2004. ISBN 978-1-4419-1833-8.
- [88] D. G. Goodall, G. W. Stevens, D. Beaglehole, and M. L. Gee. Imaging ellipsometry/reflectometry for profiling the shape of a deformable droplet as it approaches an interface. *Langmuir*, 15(13):4579–4583, 1999.
- [89] Régis Fondecave and Françoise Brochard Wyart. Polymers as dewetting agents. *Macromolecules*, 31(26):9305–9315, 1998.
- [90] J. Yang, L. C. Chow, M. R. Pais, and A. Ito. Liquid film thickness and topography determination using fresnel diffraction and holography. *Experimental Heat Transfer*, 5(4):239–252, 1992.
- [91] K. H. Guo, T. Uemura, and Wen-Jei Yang. Reflection-interference method to determine droplet profiles. *Appl. Opt.*, 24(16):2655–2659, Aug 1985.

- [92] Luis P. Thomas, Roberto Gratton, Beatriz M. Marino, and Javier A. Diez. Droplet profiles obtained from the intensity distribution of refraction patterns. *Appl. Opt.*, 34(25):5840–5848, Sep 1995.
- [93] Luis P. Thomas, Roberto Gratton, Beatriz M. Marino, and Juan M. Simon. Measurements of free-surface profile in transient flow with a simple light-slicing method. *Appl. Opt.*, 33(13):2455–2458, May 1994.
- [94] Chevres Lee Roy, Shin Dong Hwan, Hernandez Joseph, Choi Chang Kyoung, Allen Jeff, and Lee Seong-Hyuk. Fringe pattern visualization of contact lines during evaporation of nanofluid droplets. *Journal of Heat Transfer*, 135(8):080912–080912, July 2013.
- [95] Dong Hwan Shin, Joseph Hernandez, Seong Hyuk Lee, Jeffrey S. Allen, and Chang Kyoung Choi. Wettability changes and fringe patterns of contact lines due to the local aggregation effect nanofluids droplets during evaporation. In *8th International Conference on Multiphase Flow – ICMF 2013*, number ICMF-988, Jeju, Korea, May 2013.
- [96] S. Gogineni, L. Goss, D. Pestian, and R. Rivir. Two-color digital piv employing a single ccd camera. *Experiments in Fluids*, 25(4):320–328, 1998.
- [97] J. Sakakibara and R.J. Adrian. Measurement of temperature field of a rayleigh-bénard convection using two-color laser-induced fluorescence. *Experiments in Fluids*, 37(3):331–340, 2004.
- [98] V K Natrajan and K T Christensen. Two-color laser-induced fluorescent thermometry for microfluidic systems. *Measurement Science and Technology*, 20(1):015401, 2009.



- [99] M Naito, M Inoue, M Ichiyanagi, Y Sato, and K Hishida. Development of two-color digital holographic ptv for dispersed two-phase flow. *Journal of Physics: Conference Series*, 147(1):012054, 2009.
- [100] M Oishi, H Kinoshita, T Fujii, and M Oshima. Simultaneous measurement of internal and surrounding flows of a moving droplet using multicolour confocal micro-particle image velocimetry (micro-piv). *Measurement Science and Technology*, 22(10):105401, 2011.
- [101] Joseph E. Hernandez and Jeffrey S. Allen. Visualization of flow near a steadily advancing meniscus. In *9TH INTERNATIONAL SYMPOSIUM ON PARTICLE IMAGE VELOCIMETRY – PIV11*, Kobe, Japan, July 2011.

## APPENDICES



## A. COPYRIGHT AGREEMENTS

## A.1 Prairie Technologies

Copyright agreement for Figure 3.1



Joseph Hernandez <jehernan@mtu.edu>

---

## Copyright Permission

1 message

---

**Stephanie Keeney** <skeeney@prairie-technologies.com>  
To: Joseph Hernandez <jehernan@mtu.edu>  
Cc: Barb Tesch <btesch@prairie-technologies.com>

Mon, Jun 24, 2013 at 12:05 PM

Dear Joe,

Prairie Technologies, Inc. gives you, Joseph Hernandez, permission to use the images of the Prairie SFC, with appropriate attribution, in your thesis work.

Sincerely,

Stephanie Keeney

Stephanie Kostrna Keeney  
Prairie Technologies, Inc.  
3030 Laura Lane, Suite 140  
PO Box 620677  
Middleton, WI 53562

608.662.0022 ext. 157  
skeeney@prairie-technologies.com

## A.2 PIV11

Copyright agreement for reprinting portions of Hernandez and Allen [101] in Chapter 5

**Subject:** RE: PIV11 Permission Request  
**From:** JUN SAKAKIBARA <sakakiba@meiji.ac.jp>  
**Date:** 11/20/2013 11:36 PM  
**To:** 'Joseph Hernandez' <jehernan@mtu.edu>, <sakakiba@kz.tsukuba.ac.jp>

Dear Joseph,  
Yes, no problem.  
Jun

-----  
Jun SAKAKIBARA, PhD

Associate Professor  
Department of Mechanical Engineering  
Meiji University  
Higashimita 1-1-1, Tamaku, Kawasaki, 214-8571, Japan  
E-mail: [sakakiba@meiji.ac.jp](mailto:sakakiba@meiji.ac.jp)  
<http://www.isc.meiji.ac.jp/~sakakiba/index-e.html>  
Phone: 81-44-934-7369 / FAX: 81-44-934-7907  
Skype:jun\_sakakibara  
-----

-----Original Message-----

From: Joseph Hernandez [<mailto:jehernan@mtu.edu>]  
Sent: Thursday, November 21, 2013 1:33 PM  
To: [sakakiba@kz.tsukuba.ac.jp](mailto:sakakiba@kz.tsukuba.ac.jp)  
Subject: PIV11 Permission Request

Dr. Sakakibara,

I presented a paper PIV11-164 Visualization of Flow Near a Steadily Advancing Meniscus at PIV11. Will you grant me permission to use the paper for publication in my dissertation.

私は紙PIV11でPIV11-164"着 実に進んメニスカス近くの流れの可視化"を提示した。

あなたは私の論文誌に論文を使用する権限が付与されます。

[translate.google.com](http://translate.google.com)

Thank you,

Joseph Hernandez

Ph.D. Candidate  
Microfluidic and Interfacial Transport Laboratory Mechanical  
Engineering - Engineering Mechanics Michigan Technological University  
815 R.L. Smith Bldg.  
1400 Townsend Dr.  
Houghton, MI 49931  
906-487-4332

"Science is facts; just as houses are made of stones, so is science made of facts; but a pile of stones is not a house and a collection of facts is not necessarily science." --Henri Poincare



### A.3 Taylor1961

Copyright agreement for Figure 5.4

United States

**Total** **0.00 USD**

[Terms and Conditions](#)

#### TERMS & CONDITIONS

Cambridge University Press grants the Licensee permission on a non-exclusive non-transferable basis to reproduce, make available or otherwise use the Licensed content 'Content' in the named territory 'Territory' for the purpose listed 'the Use' on Page 1 of this Agreement subject to the following terms and conditions.

1. The permission granted is not valid until the Licensee has paid in full.
2. The License is limited to the permission granted and the Content detailed herein and does not extend to any other permission or content.
3. Cambridge gives no warranty or indemnity in respect of any third-party copyright material included in the Content, for which the Licensee should seek separate permission clearance.
4. The integrity of the Content must be ensured.
5. The License does extend to any edition published specifically for the use of handicapped or reading-impaired individuals.
6. The Licensee shall provide a prominent acknowledgement in the following format:  
author/s, title of article, name of journal, volume number, issue number, page references, , reproduced with permission.

If author's own material and free of charge then condition 1 to be removed.

Other terms and conditions: None

v1.0

**If you would like to pay for this license now, please remit this license along with your payment made payable to "COPYRIGHT CLEARANCE CENTER" otherwise you will be invoiced within 48 hours of the license date.**

**Payment should be in the form of a check or money order referencing your account number and this invoice number RLNK501148854.**

**Once you receive your invoice for this order, you may pay your invoice by credit card. Please follow instructions provided at that time.**

**Make Payment To:**  
Copyright Clearance Center  
Dept 001  
P.O. Box 843006  
Boston, MA 02284-3006

**For suggestions or comments regarding this order, contact RightsLink Customer Support:**  
[customercare@copyright.com](mailto:customercare@copyright.com) or +1-877-622-5543 (toll free in the US) or +1-978-646-2777.

**Gratis licenses (referencing \$0 in the Total field) are free. Please retain this printable license for your reference. No payment is required.**



## B. INCLUDED MATLAB CODE

### B.1 Confocal Design

```
##### Confocal slit calculations

clear,clc, close all

set(0,'DefaultFigureWindowState','docked')

set(0, 'DefaultFigurePaperOrient', 'landscape')

set(0,'DefaultAxesLineWidth',2,'DefaultAxesFontSize',30,'
    DefaultAxesFontName','times','DefaultTextFontSize',30,'
    DefaultAxesLineStyleOrder','-|---|:|-.')

markers=['+', 'o', '*', 'x', 's', 'd', '^', 'v', '>', '<', 'p', 'h'];
linecolors=['y', 'm', 'c', 'r', 'g', 'b', 'k', 'y', 'm', 'c', 'r', 'g', 'b', 'k'];
lines=get(0, 'DefaultAxesLineStyleOrder');

%% Slit width
M=[10,20,100];
NA=[0.25, .5, 1.25];
lambda=[633,543] ; % nm E-9 m
colors=['r', 'g'];
```

```

%optimum diameter
for i=1:length(lambda)
    for j=1:length(M)
D_opt(i,j)=.5*lambda(i)*10(-9)*M(j)/NA(j)*106 ; %in microns
    end
    if i==1
        figure
        hold on
    end

end
hold off
% plotting diamter
    plot(M,D_opt(1,:), 'rs-',M,D_opt(2,:), 'go-');
    legend(sprintf('s=%f', colors(1), lambda(1)), sprintf('s=%f', colors(2)
        , lambda(2)), 'Location', 'Best')
xlabel('Magnification');
xlim([0 110])
ylabel('Optimum Diameter (\mu m)');
ylim([10 30])
title('Diameter of Slit with varying excitation wavelength and
    magnification');

%% Optical Slice Calculations
% Using 2 different equations

```

```

% First equation is from page 225 eq 3 of "Handbook of Biological
    Confocal
% Microscopy" The second equation is from a zeis manual on confocal
% microscopy

K=.95
n=[1.1 1.33 1.45 1.6]
for i=1:length(lambda)

    for j=1:length(NA)
        for k=1:length(n)
dslice_1(i,j,k)=K*lambda(i)/(n(k)*(1-(1-(NA(j)/n(k))^2)^(1/2)))/1000; %
    micrometer, 1E-9 nm/1E-6 micrometer
dslice_2(i,j,k)=((.88*(lambda(i)/1000))/(n(k)-(n(k)^2-NA(j)^2)^(1/2))
    +(2^.5*n(k)*D_opt(i,j))/(NA(j)))^(1/2) ;

        % plotting with all fothe k variables and stepping through each i
        % and j, will have 2 plots (i), with multiple lines (j)
        dslice_plot1(j,k)=dslice_1(i,j,k)
dslice_plot2(j,k)= dslice_2(i,j,k)
        end
    end %end equation j loop

    for j=1:length(NA) %Starting first plot j loop
        if j==1
            figure
            hold on
        end
s1{j}=sprintf('%f',NA(j))

```

```

plot1(i,j)=plot(n,dslice_plot1(j,:))
set(plot1(i,j),'Marker',markers(j),'MarkerSize',15,'lineStyle','none
','MarkerEdgeColor',linecolors(j),'MarkerFaceColor',linecolors(j
))

    title(['Handbook of Biological Confocal \lambda =',
          num2str(lambda(i))])
ylabel('Optical Slice \mu m')
xlabel('Index of Refraction')
legend(s1)
end
hold off

for j=1:length(NA) % second plot loop
    if j==1
        figure

    end

    plot2(i,j)=semilogy(n,dslice_plot2(j,:))
set(plot2(i,j),'Marker',markers(j),'MarkerSize',15,'lineStyle','none
','MarkerEdgeColor',linecolors(j),'MarkerFaceColor',linecolors(j
))

    title(['Zeiss \lambda =', num2str(lambda(i))])
    ylabel('Optical Slice \mu m')
    xlabel('Index of Refraction')
    legend(s1)
    if j==1
        hold on
    end
end

```

**end**

**hold on**

**end**



## B.2 Confocal Axial Resolution

```
%% Lateral Resolution, Axial Resolution, and Optimal hole/slit
% for an optical slice of the confocal
%axial resolution from handbook of biological confocal microscopy third
%edition
% Axial Resolution page 225 equation 1
% Z resolution page 225 equation 3
% Optimal hole/slit page 225 equation 4
clear all
M=[10 20 40] ;
NA=[0.25 0.45 0.60] ; %20 x elwd Brightfield CFI A
Plan Fluor NA .45 wd 8.2-6.9 mm
%40 x elwd Brightfield CFI A Plan Fluor NA .60 wd
3.6-2.8 mm

n=[1 1.33 1.3825 1.474 ] ; %Air n=1,water=1.33,
borosilicate=1.474 (vitrocom)

lambda=[488E-9 643E-9] ; %488 blue, 643 red

% z resolution parameters
K=[0.67 0.95 ]; %k_hole = 0.37. slit=0.95

for j=1:length(NA);
for k=1:length(lambda);
```

```

for m=1:length(n)      ;
    for l=1:length(K);
        M_L=M(j)          ;           %_L is the loop variable
        NA_L=NA(j);
        lambda_L=lambda(k);
        n_L=n(m);

r_airy=0.61*lambda_L/NA_L *1E6; % equation 2, microns

D_opt=0.5*lambda_L*M_L/NA_L*1E6;           % equation 4, microns

FHWM_hole=K(1)*lambda_L/(n_L*(1-sqrt(1-(NA_L/n_L)^2)))*1E6 ;   % hole
    equation3 in microns,
FHWM_slit=K(2)*lambda_L/(n_L*(1-sqrt(1-(NA_L/n_L)^2)))*1E6 ;   % slit
    equation3 in microns,

row=m+length(n)*(k-1)+2*length(n)*(j-1) ;           % row=
    n+length(n)*(lambda-1)+length(n)*(M-1)
Table(row,1)=M_L          ;           % Magnification M
Table(row,2)=NA_L        ;           % NA
Table(row,3)=lambda_L*1e9;
Table(row,4)=n_L;
Table(row,5)=FHWM_hole;
Table(row,6)=FHWM_slit;
Table(row,7)=r_airy;
Table(row,8)= D_opt;

```

```
end
end
end
end
```

Table

```
% Table
% M NA Lambda n hole slit r_airy D_opt
% 20 .45 488 1
% 20 .45 488 1.33
% 20 .45 488 1.474
% 20 .45 488 1.52

% 20 .45 643 1
% 20 .45 643 1.33
% 20 .45 643 1.474
% 20 .45 643 1.52

% 40 .60 488 1
% 40 .60 488 1.33
% 40 .60 488 1.474
% 40 .60 488 1.52

% 40 .60 643 1
% 40 .60 643 1.33
% 40 .60 643 1.474
% 40 .60 643 1.52
```

### B.3 Confocal Axial Resolution - FWHM

```
% Full Width Half Maximum of the intensity of reflectance scanning for a
% confocal. I will be using the center of the image for the average
    intensity
% measurement.
% Joseph Hernandez
% 10-11-11
% Modified by David Deisenroth
% 11-24-13
%%
set(0, 'DefaultFigurePaperOrient', 'landscape')
clear , clc, close all
%% Declarations
fprintf('Current Directory is \n %s,\n is this the right directory for
    the data y/n', eval('cd'))
directorycheck=input('[n]', 's') ;

if isempty(directorycheck),    directorycheck = 'n'; end
if directorycheck == 'n', Directory_Name = uigetdir; cd(sprintf('%s',
    ...
    Directory_Name)); else Directory_Name=pwd; end

Directory = pwd;
Test_Date = 'Blue';
Test_Number = '10';

%Raw_Directory =
```

```

%sprintf('%s/Raw/%s/test%s',Directory,Test_Date,Test_Number) old method
Raw_Directory = [Directory filesep 'Raw' filesep Test_Date filesep 'test
    ' Test_Number];
Processed_Directory = [Directory filesep 'Processed' filesep Test_Date
    filesep 'test' Test_Number];

File_Format = 'tif';

fid=fopen([Raw_Directory filesep sprintf('test%s.txt',Test_Number)]);
Z_Location=-1* cell2mat(textscan(fid,'%f','delimiter',' ')); % z
    location location in microns starting from the initial scan, - sign
    is from the stage location
Scan_Number = length(Z_Location');

%% File Import

%Image_List = dir(sprintf('%s/*.%s',Raw_Directory,File_Format)); old
    method
%using fullfile for compatibility with windows
%Image_List_Names = vertcat(Image_List.name); integrated in the end of
    the
%Image_List_Full_Path
%Image_List_Full_Path =
%strcat({sprintf('%s/',Raw_Directory)},Image_List_Names); old method,
    using
%filesep from now on

```

```

Image_List = dir(fullfile(Raw_Directory,sprintf('*.%s',File_Format)));
Image_List_Full_Path = strcat({Raw_Directory},filesep, vertcat(
    Image_List.name));
Image_Number = length(Image_List_Full_Path);

%% Image Information

[Image_Info Image_X Image_Y Bit_Depth Color]=imageinformation(
    Image_List_Full_Path{1}); %Function imageinformation.m inputs from
    the workspace and outputs image information

%% Image Import and Window Size and Averaging of image intensity

prompt = {'yes (1) No (0)', 'X Distance From Center', 'Y Distance From
    Center'};
dlg_title = 'Bounding Box';
num_lines = 1;
def = {'0', '200', '200'};
Bounding_Box_Answers = inputdlg(prompt,dlg_title,num_lines,def);

%Bounding_Box = 0; %Use 0 for whole image or 1 for a smaller center
    defined below
Bounding_Box = str2double(Bounding_Box_Answers(1))

```

```

% Center of image , X_Center x Y_Center
%X_Center = 200 ; % pixels in the x direction for the center detection
%Y_Center =200; % pixels in the y direction for the center detection
X_Center = str2double(Bounding_Box_Answers(2))
Y_Center = str2double(Bounding_Box_Answers(3))

X_Center_Bound = (Image_X/2-X_Center/2):(Image_X/2+X_Center/2);
Y_Center_Bound = (Image_Y/2-Y_Center/2):(Image_Y/2+Y_Center/2);

Image_tmp = zeros(Image_X,Image_Y);
Images_Avg=zeros(1,length(Image_Number));

for i=1:Scan_Number
    Image_tmp = imread(Image_List_Full_Path{i}'); %Transpose the image
        because it reads in height first and not width
if Bounding_Box == 0
        Images_Avg(i) = mean(mean(Image_tmp(:, :))); %Whole image
else
        Images_Avg(i) = mean(mean(Image_tmp(X_Center_Bound,Y_Center_Bound)))
            ; %Partial image
end
end
Images_Avg_Normal = Images_Avg./max(Images_Avg);

%% Data Selection and Scaling

```

```

% shifting the data base on index of refraction and rough n ratio
plot(Z_Location, Images_Avg_Normal, 'b');
fprintf('Do you want to adjust for index of refraction change?')
directorycheck=input('[n]', 's') ;

if isempty(directorycheck),      directorycheck = 'n'; end
if directorycheck == 'n'
Data_Shifted = Z_Location

else Directory_Name=pwd;
[X1 Y1] = ginput(2);
Data_n_Start = min(find(Z_Location>=round(min(X1))))
Data_n_end =max(find(Z_Location<=round(max(X1))))
Data_Shifted = Z_Location
Data_Shifted (Data_n_Start:Data_n_end)=Data_Shifted (Data_n_Start:
    Data_n_end)+(Data_Shifted (Data_n_Start:Data_n_end)-min(X1))*1.474

hold on
plot(Data_Shifted, Images_Avg);
hold off
end

[X Y] = ginput(2);
Data_Start = find(Data_Shifted >= min(X), 1 );
Data_End = find(Data_Shifted <= max(X), 1, 'last' );
% Data_Start = find(Z_Location >= X(1), 1 );
% Data_End = find(Z_Location <= X(2), 1, 'last' );
plot(Data_Shifted(Data_Start:Data_End), Images_Avg(Data_Start:Data_End));

```



```

% Data
X_Data = Z_Location(Data_Start:Data_End);
Y_Data = Images_Avg(Data_Start:Data_End)';

% Normalizing Data
X_Norm_Slope = (1-0.01)/(max(X_Data)-min(X_Data)); %Slope of x data
    for scaling
X_Norm_Offset = 0.01-X_Norm_Slope*min(X_Data); %Offset for the
    x data

Y_Norm_Slope = (1-.01)/(max(Y_Data)-min(Y_Data)); %Slope of y data
    for scaling
Y_Norm_Offset = 0.01-Y_Norm_Slope*min(Y_Data); %Offset for the y data

X_Data_Scaled = X_Norm_Slope.*X_Data + X_Norm_Offset;
Y_Data_Scaled = Y_Norm_Slope.*Y_Data + Y_Norm_Offset;

plot(X_Data_Scaled,Y_Data_Scaled)

X_Line = linspace(0,1,500);

% Save Data from the Graphed
Data_Normaled = [X_Data_Scaled Y_Data_Scaled ];
dlmwrite([Processed_Directory filesep 'test' Test_Number '.txt'],
    Data_Normaled,'delimiter',' ','')

```

```

%% Gaussian Fit

% normfit [mu sigma] = normfit

% using this http://en.wikipedia.org/wiki/Gaussian\_function
% and http://terpconnect.umd.edu/~toh/spectrum/CurveFitting.html

% see dissertation write up

% lny = log(Images_Avg(Data_Start:Data_End));
% lnx = Z_Location(Data_Start:Data_End)';
% A = polyfit(lnx, lny, 2);
%
% a = A(1); %A(1) is the coefficient for the x^2 term
% b = A(2); %A(2) is the coefficient for the x term
% c = A(3); %A(3) is the coefficient for the last term
%
% sigma = sqrt(-1/(2*a)) ; %sqrt(-1/2 a)
% mu = b * sigma^2 ;
% A = exp(c + mu^2/(2*sigma^2));
%
% x = Z_Location;
% fit = A*exp(-(x-mu).^2/(2*sigma^2));
%
% figure,
% hold on
% plot(Images_Avg(Data_Start:Data_End), 'or')
% plot(fit(Data_Start:Data_End), 'b+')

```

```

%
% error = abs(max(Images_Avg_Normal)-max(fit))/max(Images_Avg);
%
% [mu1, sigma1] = normfit(Images_Avg_Normal);
% fit_norm = 1/(sigma1*sqrt(2*pi))*exp(-(x-mu1).^2/(2*sigma1));
%
% fwhm = 2*sqrt(2*log(2)); %*sigma

%% Gaus Amp from Origin Pro - Gauss Amplitude
%A = GA1
%xc = GA2
%w = GA3

Gauss_Amp = @(GA,x)GA(4) + GA(1).*exp(-0.5*((x-GA(2))./GA(3)).^2);
Gauss_Amp_IC = [1 .5 .5 min(Y_Data_Scaled) ];

Gauss_Amp_Fit = nlinfit(X_Data_Scaled,Y_Data_Scaled,Gauss_Amp,
    Gauss_Amp_IC);

figure
h=plot(X_Data_Scaled,Y_Data_Scaled);
line(X_Line, Gauss_Amp(Gauss_Amp_Fit, X_Line), 'Color','r','LineWidth'
    ,2); %Gaussian

set(gcf, 'PaperUnits', 'normalized');
set(gcf, 'PaperPosition', [0 0 1 1]);
axis([0,1.1,0,1.1])
xlabel('X^*', 'FontWeight', 'bold', 'FontSize', 25)

```

```

ylabel('Y^*', 'FontWeight', 'bold', 'FontSize', 25)
set(gca, 'FontSize', 16);
legend({'Dimensionless Raw Data', 'Gaussian',});
legend('Location', 'NorthWest')

print('-depsc2', '-loose', [Processed_Directory filesep 'test' Test_Number
    '_Gauss.eps']);
print('-dpdf', '-loose', [Processed_Directory filesep 'test' Test_Number '
    _Gauss.pdf']);
saveas(gcf, [Processed_Directory filesep 'test' Test_Number '_Gauss.fig'
    ]);

%% Lorentzian Function Cauchy-lorentz
%
%L(1) = A
%L(2) = w
%L(3) = xc
Lorentz = @(L,x)L(4) + (2*L(1)/pi).*(L(2)./(4*(x-L(3)).^2 + L(2).^2));

%Initial Conditions %standard starting values
X0 = 0.5 ;
A0 = 1 ;
W0 = 0.5 ;
Y0 = min(Y_Data_Scaled)
Lorentz_IC = [A0 W0 X0 Y0] ;

```

```

options=optimset('Display','on','Algorithm','levenberg-marquardt','
    ScaleProblem','Jacobian','TolFun',1e-12,'TolX',1e-12,'MaxFunEvals'
    ,10000,'MaxIter',10000);

Lorentz_Fit = lsqcurvefit(Lorentz,Lorentz_IC,X_Data_Scaled,Y_Data_Scaled
    ,[],[],options)
Lorentz_Fit2 = nlinfit(X_Data_Scaled,Y_Data_Scaled,Lorentz,Lorentz_IC);

figure
h=plot(X_Data_Scaled,Y_Data_Scaled);
line(X_Line, Lorentz(Lorentz_Fit, X_Line), 'Color','g','LineWidth',2); %
    lorentz

set(gcf,'PaperUnits','normalized');
set(gcf,'PaperPosition',[0 0 1 1]);
axis([0,1.1,0,1.1])
xlabel('X^*','FontWeight','bold','FontSize',25)
ylabel('Y^*','FontWeight','bold','FontSize',25)
set(gca,'FontSize',16);
legend({'Dimensionless Raw Data', 'Lorentz',});
legend('Location','NorthWest')

print('-depsc2','-loose',[Processed_Directory filesep 'test' Test_Number
    '_Lorentz.eps']);
print('-dpdf','-loose',[Processed_Directory filesep 'test' Test_Number '
    _Lorentz.pdf']);
saveas(gcf,[Processed_Directory filesep 'test' Test_Number '_Lorentz.fig
    ']);

```

```

% %% Weibull
% Weibull = @(w,x) w(3) .* (x ./ w(1)).^(w(2)-1) .* exp(-(x ./ w(1)).^w
    (2));
%
% % w(1) = lambda
% % w(2) = k
% Lambda0 = .2 ;
% K0= .5 ;
% sd=.2;
%
%
%
% %% Weibull_IC = [ Lambda0 K0 sd];
% %
% %% Weibull_Fit = lsqcurvefit(Weibull,Weibull_IC,X_Data_Scaled,
    Y_Data_Scaled,[],[],options);
% %% Weibull_Fit1 = nlinfit(X_Data_Scaled,Y_Data_Scaled,Weibull,
    Weibull_IC);
%
% figure
% h=plot(X_Data_Scaled,Y_Data_Scaled);
% line(X_Line, Weibull(Weibull_Fit, X_Line), 'Color','m','LineWidth',2);
% Weibull
%
% set(gcf,'PaperUnits','normalized');
% set(gcf,'PaperPosition',[0 0 1 1]);

```

```

% axis([0,1.1,0,1.1])
% xlabel('X^*', 'FontWeight', 'bold', 'FontSize', 25)
% ylabel('Y^*', 'FontWeight', 'bold', 'FontSize', 25)
% set(gca, 'FontSize', 16);
% legend({'Dimensionless Raw Data', 'Weibull',});
% legend('Location', 'NorthWest')
%
% print('-depsc2', '-loose', [Processed_Directory filesep 'test'
    Test_Number '_Weibull.eps']);
% print('-dpdf', '-loose', [Processed_Directory filesep 'test' Test_Number
    '_Weibull.pdf']);
% saveas(gcf, [Processed_Directory filesep 'test' Test_Number '_Weibull.
    fig']);
%

%% Plots of the graphs
figure
h=plot(X_Data_Scaled, Y_Data_Scaled);

X_Line = linspace(0,1,100);
hold on
line(X_Line, Gauss_Amp(Gauss_Amp_Fit, X_Line), 'Color','r','LineWidth'
    ,2); %Gaussian
line(X_Line, Lorentz(Lorentz_Fit, X_Line), 'Color','g','LineWidth',2); %
    lorentz
% line(X_Line, Weibull(Weibull_Fit, X_Line), 'Color','m','LineWidth',2);
    %Weibull

```

```

axis([0,1.1,0,1.1])
xlabel('X^*', 'FontWeight', 'bold', 'FontSize', 25)
ylabel('Y^*', 'FontWeight', 'bold', 'FontSize', 25)
set(gca, 'FontSize', 16);
legend({'Dimensionless Raw Data', 'Gaussian', 'Lorentz', 'Weibull'});
legend('Location', 'NorthWest')

print('-depsc2', '-loose', [Processed_Directory filesep 'test' Test_Number
    '.eps']);
print('-dpdf', '-loose', [Processed_Directory filesep 'test' Test_Number '
    .pdf']);
saveas(gcf, [Processed_Directory filesep 'test' Test_Number '.fig']);

%% Peak and X location

X_Slope_Unscaled = (max(X_Data)-min(X_Data))/(1-.01)      ;
X_Intercept_Unscaled = min(X_Data)-X_Slope_Unscaled*0.01  ;
Y_Slope_Unscaled = (max(Y_Data)-min(Y_Data))/(1-.01)      ;
Y_Intercept_Unscaled = min(Y_Data)-Y_Slope_Unscaled*0.01  ;

% Peak intensity found from xline
Y_Peak_Gauss_Amp_Found = max(Gauss_Amp(Gauss_Amp_Fit,X_Line));
Y_Peak_Lorentz_Found = max(Lorentz(Lorentz_Fit,X_Line));
% Y_Peak_Weibull_Found =real( max(Weibull(Weibull_Fit,X_Line)));

% Peak location found from xline

```



```

X_Peak_Gauss_Amp_Found = X_Line(Gauss_Amp(Gauss_Amp_Fit,X_Line) ==
    Y_Peak_Gauss_Amp_Found);
X_Peak_Lorentz_Found = X_Line(find(Lorentz(Lorentz_Fit,X_Line) ==
    Y_Peak_Lorentz_Found));
% X_Peak_Weibull_Found = X_Line(find(real(Weibull(Weibull_Fit,X_Line))
    == Y_Peak_Weibull_Found));

% Peak intensity found from xline
Y_Peak_Gauss_Amp_Found_Unscaled = Y_Peak_Gauss_Amp_Found*
    Y_Slope_Unscaled +Y_Intercept_Unscaled;
Y_Peak_Lorentz_Found_Unscaled = Y_Peak_Lorentz_Found*Y_Slope_Unscaled +
    Y_Intercept_Unscaled;
% Y_Peak_Weibull_Found_Unscaled = real(Y_Peak_Weibull_Found*
    Y_Slope_Unscaled +Y_Intercept_Unscaled);

% Peak location intensity found from xline
X_Peak_Gauss_Amp_Found_Unscaled = X_Peak_Gauss_Amp_Found*
    X_Slope_Unscaled +X_Intercept_Unscaled;
X_Peak_Lorentz_Found_Unscaled = X_Peak_Lorentz_Found*X_Slope_Unscaled +
    X_Intercept_Unscaled;
% X_Peak_Weibull_Found_Unscaled = real(X_Peak_Weibull_Found*
    X_Slope_Unscaled +X_Intercept_Unscaled);

[Y_Peak_Actual Y_Peak_Position] = max(Y_Data);
X_Peak_Actual = X_Data(find(Y_Data==max(Y_Data)));

```

```

%% FWHM
% FWHM will be the difference from the right to the left of the curve
% finding the values of x at x_0-parameter and x_0+parameter
% gaussian w is sigma in the above expressions so 2*sqrt(2*ln(2))*w is
    the
% fwhm or hwhm is sqrt(2*ln(2))*w
% lorentz 2*gamma is the fwhm or x0-gamma x0+gamma are the bounds

FWHM_Gaussian_Scaled = 2*sqrt(2*log(2))*Gauss_Amp_Fit(3);
FWHM_Lorentz_Scaled = Lorentz_Fit(2);

% Actual

figure
plot(X_Data_Scaled,Y_Data_Scaled)
hold on
Difference = (max(Lorentz(Lorentz_Fit, X_Line))+min(Lorentz(Lorentz_Fit,
    X_Line)))/2;
line([min(X_Data_Scaled) max(X_Data_Scaled)], [Difference Difference ]);
line(X_Line, Lorentz(Lorentz_Fit, X_Line), 'Color','g','LineWidth',2); %
    lorentz
zoom on; % use mouse button to zoom in or out
% Press Enter to get out of the zoom mode.

% CurrentCharacter contains the most recent key which was pressed after
    opening
% the figure, wait for the most recent key to become the return/enter
    key

```

```

waitfor(gcf,'CurrentCharacter',13)

zoom reset
zoom off

Points = ginput(2);
FWHM_Actual = Points(2)-Points(1);

% % Actual
% Y_Delta = max(Y_Data)+min(Y_Data);
% %X_Delta = max(X_Data)+min(X_Data);
% %X_Scaled = X_Delta.*X_Line;
% Y_Scaled = Y_Delta.*Y_Data_Scaled;
% figure
% plot(X_Data,Y_Data)
% hold on
% Difference = (max(Y_Data)+min(Y_Data))/2;
% line([min(X_Data) max(X_Data)], [Difference Difference]);
% line(X_Data, Lorentz(Lorentz_Fit, X_Data), 'Color','g','LineWidth',2);
%lorentz
% zoom on; % use mouse button to zoom in or out
% % Press Enter to get out of the zoom mode.
%
% % CurrentCharacter contains the most recent key which was pressed
% after opening
% % the figure, wait for the most recent key to become the return/enter
% key
% waitfor(gcf,'CurrentCharacter',13)

```

```

%
% zoom reset
% zoom off
%
% Points = ginput(2);
% FWHM_Actual = Points(2)-Points(1);

%% Data Save

save([Processed_Directory filesep 'test' Test_Number '.mat']);

%variables=(['FWHM_Actual' , 'FWHM_Lorentz_Unscaled' , '
    FWHM_Gaussian_Unscaled' ])

FWHM_Gaussian_Unscaled =FWHM_Gaussian_Scaled * X_Slope_Unscaled +
    X_Intercept_Unscaled;
FWHM_Lorentz_Unscaled =Lorentz_Fit(2) * X_Slope_Unscaled +
    X_Intercept_Unscaled

X_Delta = max(X_Data)-min(X_Data);
(FWHM_Actual*X_Delta)/100
FWHM_Lorentz_Unscaled/100
FWHM_Gaussian_Unscaled/100

```

```
save([Processed_Directory filesep 'test' Test_Number '.txt'],  
      FWHM_Actual' , 'FWHM_Lorentz_Unscaled' , 'FWHM_Gaussian_Unscaled', '-  
      ascii', '-double', '-tabs' ) ;
```

## B.4 Liquid Film Thickness Detection

```
% Data Analysis for film thickness measurements
% Joseph Hernandez
% 06-02-13
% Version 6 is changed from 5 by making the intensity plot points
% different colors based on the bubble number. It is particularly useful
% for processing the data from 7-17

%Version 7 is changed from 6 by instead of averaging all images, just 3
%images which are located approximately 1.5 diameters behind the leading
%meniscus

%Version 8_withcrop - added image output lines 390, added min and max ca
%output and fprintf to current directory

%Version 9 - bounding box and smoothing added 10-08-13

%% Initial
clear,clc,close all
set(0,'DefaultAxesFontSize', 20) %Large text size for prints
set(0,'DefaultTextFontSize', 20) %Large text size for prints
set(0,'DefaultFigurePaperOrientation','landscape', '
    DefaultFigurePaperPosition', [ 0.25 0.25 10.5 8 ] ) %Fill page
    with plot for saving and printing
%set(0,'DefaultFigureWindowStyle','docked') %windows dont popup
```

```

%% Defining test parameters either 1000um channel with water or 500um
    channel with cargille oil

prompt = {'Water with 100um channel (0) OR Cargille oil with 500um
    channel (1)'};
dlg_title = 'Test parameters';
num_lines = 1;
def = {'0'};
Parameters_Answer = inputdlg(prompt,dlg_title,num_lines,def);
Parameters_Answer = str2double(Parameters_Answer)

if Parameters_Answer == 0 %WATER
    Mu = 1*10(-3); %N*m/s2
    Sigma = 0.069; %N/m
    R = 0.0005; %m Tube radius
    rho = 998; %kg/m3 at 20 celcius
elseif Parameters_Answer == 1 % Cargille OIL
    Mu = 0.01896; %N*m/s2
    Sigma = 0.029467; %N/m
    R = 0.00025; %m Tube radius
    rho = 854; %kg/m3 at 20 celcius
end

%% Processed Directory
% folder should be the test run that is being processed

Data_Directory = uigetdir(pwd, sprintf('Pick Processed Folder Directory
    - Root Directory Data'));
cd(Data_Directory)

```

```

        Processed_Directory_List=dir(Data_Directory);
Dir_Check = strfind(strcat(Processed_Directory_List.name), '
        Processed');
if isempty(Dir_Check) == 1,mkdir('Processed');end
Processed_Directory = [ pwd filesep 'Processed' filesep ] ;

%% Test Log Import

% log file has the following data assembled in columns
% test #      position #      save rate      bubble #      HSC
%      bubble entrance frame      HSC bubble exit frame
% Pulnix entrance frame      Pulnix exit frame      velocity (cm/s)
%      R^2

Test_Log_Filename = ['log.txt'];
Test_Log_File = fopen(Test_Log_Filename);
Test_Log= textscan(Test_Log_File, '%f %f %.2f %f %f %f %f %f %.4f
%.4f ' , 'delimiter','\t');
fclose(Test_Log_File);

Test_Number      = Test_Log{1}; % Test Number array
Position_Number  = Test_Log{2}; % Position Number
Save_Rate        = Test_Log{3}; % Average Save Rate
Bubble_Number    = Test_Log{4}; % Bubbler number for that position

```



```

HSC_Entrance    = Test_Log{5}; % High speed camera entrance frame
                    for the bubble
HSC_Exit        = Test_Log{6}; % High speed camera exit frame for
                    the bubble
Pulnix_Entrance = Test_Log{7}; % Pulnix entrance frame for the
                    bubble
Pulnix_Exit     = Test_Log{8}; % Pulnix exit frame for the bubble
Velocity        = Test_Log{9}; % Velocity cm/s
R_Square        = Test_Log{10}; % R squared value for the velocity
                    fit
Ca = Velocity*(Mu/(100*Sigma)); %Ca convert velocity to m/s
Re = (Velocity/100)*R*2*rho/Mu; %Reynolds number
We = Re.*Ca;

if Parameters_Answer == 0 %WATER
    Frames_Skip_Raw = ((750e-6)./(Velocity/100))*200; %average velocity
                    multiplied by 750um (1.5 diameters from front of leading
                    meniscus) multiplied by camera speed to number of frames
    Frames_Skip = round(Frames_Skip_Raw);
    for k = 1:length(Frames_Skip)
        if HSC_Exit(k) - HSC_Entrance(k) <= Frames_Skip(k)+4
            Frames_Skip(k) = round( (HSC_Exit(k) - HSC_Entrance(k))/3)
        end
    end
elseif Parameters_Answer == 1 % Cargille OIL
    Frames_Skip = zeros(1,length(Test_Number))
end

```

```

%% Load Calibration
% Folder name for calibration data is "reference point" file with step
  size is "reference steps.txt"
Prompt_Cal = {'Calibration data?'};
DLG_Title_Parameters_Cal = 'Calibration data? y/n';
Default_Parameters_Cal = {'y'};
options.Interpreter='tex';
options.Resize = 'on'
Parameters_Input_Str_Cal = inputdlg(Prompt_Cal,DLG_Title_Parameters_Cal
  ,1,Default_Parameters_Cal,options);
% Cal = eval( [ '[' , cell2mat(Parameters_Input_Str_Bubbles(1)), ']' ] )
  % cell2mat converts cell string to numbers with comma seperating
  them, eval converts it to a double array
% Bubbles_Ca = str2double(cell2mat(Parameters_Input_Str_Bubbles(2)))
close all

if strcmp(Parameters_Input_Str_Cal,'y')

%Calibration_Folder = uigetdir(pwd,sprintf('Pick the Calibration
  Directory')) % can change if name stays the same
Calibration_Folder = 'reference point';
Calibration_List_Filename = ['reference steps.txt']
Calibration_List_File = fopen(Calibration_List_Filename)
Calibration_List= double(cell2mat(textscan(Calibration_List_File, '%f %f
  ', 'delimiter','\t')));
Calibration_Z = Calibration_List(:,2);

fclose(Calibration_List_File)

```

```

%% Height Calibration

Calibration_Image_List_Raw = dir([Calibration_Folder filesep '*.tif']) ;
    %dir will get the file list into a structure need to find just the
    names
Calibration_Image_List = vertcat(Calibration_Image_List_Raw.name); %
    vertically concatenate the names for use later

Calibration_Image_List = strvcat(Calibration_Image_List_Raw.name);
test = sortrows(Calibration_Image_List);

[Image_Info Image_X Image_Y Bit_Depth Color]=imageinformation([
    Calibration_Folder filesep Calibration_Image_List(1,:)]); %Function
    imageinformation.m inputs from the workspace and outputs image
    information

%select first image for selecting ginput

%Temp_Calibration_Image = imread([Calibration_Folder filesep
    Calibration_Image_List(1,:)]);
%[Temp_Calibration_Crop, Crop_Rect] = imcrop(Temp_Calibration_Image);

```

```

##### ADDED FOR SELECTING DATA#####
prompt = {'yes (1) No (0)', 'X Distance From Center', 'Y Distance From
        Center'};
dlg_title = 'Bounding Box';
num_lines = 1;
def = {'0', '150', '250'};
Bounding_Box_Answers = inputdlg(prompt,dlg_title,num_lines,def);

%Bounding_Box = 0; %Use 0 for whole image or 1 for a smaller center
        defined below
Bounding_Box = str2double(Bounding_Box_Answers(1))

% Center of image , X_Center x Y_Center
%X_Center = 200 ; % pixels in the x direction for the center detection
%Y_Center =200; % pixels in the y direction for the center detection
X_Box = str2double(Bounding_Box_Answers(2))
Y_Box = str2double(Bounding_Box_Answers(3))

% Image_tmp = zeros (Image_X, Image_Y);
% Images_Avg=zeros (1,length(Calibration_Image_List));

for i=1:length(Calibration_Image_List(:,1))

```

```

Temp_Calibration_Image = imread([Calibration_Folder filesep
    Calibration_Image_List(i,:)]); %Transpose the image because it
    reads in height first and not width
if Bounding_Box == 0
    Calibration_Average_Intensity(i) = mean(mean(Temp_Calibration_Image)
        );%Whole image
else
    if i==1
        Temp_Calibration_Image_Center = imread([Calibration_Folder
            filesep Calibration_Image_List(length(Calibration_Image_List
                (:,1))/2 ,:)]); % middle image for more robust image
            processing
        imagesc(Temp_Calibration_Image_Center,[2^10.-1 2^11-1])
        colormap('gray')
        [X_Center Y_Center]= ginput(1)
        close
        X_Center_Bound = round(X_Center-X_Box/2):round(X_Center+X_Box/2);
        Y_Center_Bound = round(X_Center-Y_Box/2):round(X_Center+Y_Box/2);
        end
        Calibration_Average_Intensity(i) = mean(mean(Temp_Calibration_Image(
            X_Center_Bound,Y_Center_Bound))); %Partial image
    end
end
%
% for i=1:length(Calibration_Image_List(:,1))
%     Temp_Calibration_Image = imread([Calibration_Folder filesep
%         Calibration_Image_List(i,:)]);
%     Temp_Calibration_Crop = imcrop(Temp_Calibration_Image,Crop_Rect);

```

```

% Calibration_Average_Intensity(i) = mean(mean(
    Temp_Calibration_Image)); %Partial image
% end

%clear Temp_Calibration_Image %Temp_Calibration_Image % clearing
    Memory

Calibration_Average_Intensity_Normal = Calibration_Average_Intensity./
    max(Calibration_Average_Intensity);

figure
plot(Calibration_List(:,2),Calibration_Average_Intensity_Normal,'rs-')
xlabel('Calibration Position (\mu m)')
ylabel('Intensity' )
title('Calibration')

%% Gaussian
%A = GA1
%xc = GA2
%w = GA3
%Y0 = GA4

Gauss_Amp = @(GA,x)GA(4) + GA(1).*exp(-0.5*((x-GA(2))./GA(3)).^2);
Gauss_Amp_IC = [1 5 5 min(Calibration_Average_Intensity_Normal)/2 ];

```

```

Gauss_Amp_Fit = nlinfit(Calibration_List(:,2)',
    Calibration_Average_Intensity_Normal,Gauss_Amp,Gauss_Amp_IC);

%% Lorentzian Function Cauchy-lorentz
%L(1) = A
%L(2) = w
%L(3) = xc
Lorentz = @(L,x)L(4) + (2*L(1)/pi).*(L(2)./(4*(x-L(3)).^2 + L(2).^2));

X0 = 5 ;
A0 = 1 ;
W0 = 5 ;
Y0 = min(Calibration_Average_Intensity_Normal)/2
Lorentz_IC = [A0 W0 X0 Y0] ;

options=optimset('Display','on','Algorithm','levenberg-marquardt','
    ScaleProblem','Jacobian','TolFun',1e-12,'TolX',1e-12,'MaxFunEvals'
    ,10000,'MaxIter',10000);

Lorentz_Fit = lsqcurvefit(Lorentz,Lorentz_IC,Calibration_List(:,2)',
    Calibration_Average_Intensity_Normal,[],[],options)
Lorentz_Fit2 = nlinfit(Calibration_List(:,2)',
    Calibration_Average_Intensity_Normal,Lorentz,Lorentz_IC)

%% Plot the lines
figure
h=plot(Calibration_List(:,2),Calibration_Average_Intensity_Normal,'rs-')
    ; %Plot original data

```

```

X_Line = linspace(0,max(Calibration_List(:,2)),500); %Make a data set
        that spans the z-axis range

line(X_Line, Gauss_Amp(Gauss_Amp_Fit, X_Line), 'Color','g','LineWidth'
      ,2); %Gaussian
line(X_Line, Lorentz(Lorentz_Fit, X_Line), 'Color','b','LineWidth',2); %
      lorentz

legend('Intensity Data','Gaussian','Lorentz','Location','SouthEast')
title('Intensity vs. Postition Fit')

save(sprintf('%sCalibration Fit %d.mat',Processed_Directory,Test_Number
            (1)))
print(gcf, '-depsc2',sprintf('%sCalibration Fit %d.eps',
        Processed_Directory,Test_Number(1))) %Save as an eps
saveas(gcf,sprintf('%sCalibration Fit %d.fig',Processed_Directory,
        Test_Number(1))) % save as a fig
print(gcf, '-dpdf',sprintf('%sCalibration Fit %d.pdf',
        Processed_Directory,Test_Number(1))) %Save as an eps

pause

Prompt_Z_Axis = {'Z Axis Location (\mu m)'};
DLG_Title_Parameters_Z_Axis = 'Using the figure what is your best
        approximation for the Z Axis Location ';
Default_Parameters_Z_Axis = {num2str(Lorentz_Fit(3))};
options.Interpreter='tex';

```



```

options.Resize = 'on'
Parameters_Input_Str_Z_Axis = inputdlg(Prompt_Z_Axis,
    DLG_Title_Parameters_Z_Axis,1,Default_Parameters_Z_Axis,options);
Z_Axis_Location_Cal = str2double(Parameters_Input_Str_Z_Axis)
end

%%%%%%%%%%%%%%%%%%%%%%%%%%%%%%%%%%%%%%%%%%%%%%%%%%%%%%%%%%%%%%%%%%%%%%%%

%% Position Location Import
Postion_Filename = 'positions.txt'
Positions_File = fopen(Postion_Filename)
Positions = cell2mat(textscan(Positions_File,'%f %f'))    %position is
    in microns

%% Test Log Import

% log file has the following data assembled in columns
% test #      position #      save rate      bubble #      HSC
    bubble entrance frame      HSC bubble exit frame
% Pulnix entrance frame      Pulnix exit frame      velocity (cm/s)
    R^2

% loop for legend
for i=1:length(Test_Number)
Test_Number_Legend{i,1} = sprintf('# %d: Position %d, Bubble %d',i,
    Position_Number(i), Bubble_Number(i))

```

```

end

figure
cc='rgbcmykrgrbcmykrgrbcmykrgrbcmykrgrbcmykrgrbc ...
mykrgrbcmykrgrbcmykrgrbcmykrgrbcmykrgrbcmykrgrbcmykrgrbcmykrgrbcmykr'
    % for different colors
ss = '+o*xsd^v<ph+o*xsd^v<ph+o*xsd^v<ph+o*xsd^v<ph+o*xsd^v<ph+o*xsd^v<
    <ph+o*xsd^v<ph+o*xsd^v<ph+o*xsd^v<ph+o*xsd^v<ph+o*xsd^v<ph+o*xsd^
    v<ph+o*xsd^v<ph+o*xsd^v<ph+o*xsd^v<ph+o*xsd^v<ph' %Diffrent
    symbols
hold on

j=1
for i=1:length(Test_Number)    %Plotting in a loop for easier viewing
    plot(i,Ca(i), 'Marker', ss(j), 'MarkerEdgeColor', cc(j), 'Linestyle
        ', 'none')

    if(i < length(Test_Number) )
if (Position_Number(i) < Position_Number(i+1))
    j=j+1
end
end

end

legend(Test_Number_Legend')
xlabel('Bubble Number')

```

```
ylabel('Ca')
```

```
grid on
```

```
save(sprintf('%sBubble v Ca %d.mat',Processed_Directory,Test_Number  
(1)))
```

```
print(gcf, '-depsc2',sprintf('%sBubble v Ca %d.eps',  
Processed_Directory,Test_Number(1))) %Save as an eps
```

```
saveas(gcf,sprintf('%sBubble v Ca %d.fig',Processed_Directory,  
Test_Number(1))) % save as a fig
```

```
print(gcf, '-dpdf',sprintf('%sBubble v Ca %d.pdf',  
Processed_Directory,Test_Number(1))) %Save as an eps
```

```
pause
```

```
%% setup up a choice for the data
```

```
% Thin Film Locations
```

```
Prompt_Bubbles = {'Bubble Numbers to Use'};
```

```
DLG_Title_Parameters_Bubbles = 'Bubble List, use Legend';
```

```
Default_Parameters_Bubbles = {'1,2,3'};
```

```
options.Interpreter='tex';
```

```
options.Resize = 'on'
```

```
Parameters_Input_Str_Bubbles = inputdlg(Prompt_Bubbles,
```

```
DLG_Title_Parameters_Bubbles,1,Default_Parameters_Bubbles,options);
```

```

Bubbles = eval( [ '[' , cell2mat(Parameters_Input_Str_Bubbles(1)), ']' ]
    ) % cell2mat converts cell string to numbers with comma seperating
    them, eval converts it to a double array
    %Bubbles_Ca = str2double(cell2mat(Parameters_Input_Str_Bubbles(2)))
close all

%Velocity_Avg = Bubbles_Ca*Sigma/Mu; %velocity based on average
    capillary number of bubble sample
%Frames_Skip_Raw = (750e-6/Velocity_Avg)*200; %average velocity
    multiplied by 750um (1.5 diameters from front of leading meniscus)
    multiplied by camera speed to number of frames
%Frames_Skip = round(Frames_Skip_Raw);

%% Getting Position Images

%%%%%%%%%%%%%%%%%%%%%%%%%%%%%%%%%%%%%%%%%%%%%%%%%%%%%%%%%%%%%%%%%%%%%%%%%% ADDED FOR SELECTING DATA%%%%%%%%%%%%%%%%%%%%%%%%%%%%%%%%%%%%%%%%%%%%%%%%%%%%%%%%%%%%%%%%%%%%%%%%%%
prompt = {'Bounding Box','Y Distance From Center','X Distance From
    Center','Smoothing','Smoothing Value'};
dlg_title = 'Bounding Box and Smoothing yes (1) No (0)';
num_lines = 1;
def = {'1','200','200','1','7'};
Bounding_Box_Answers = inputdlg(prompt,dlg_title,num_lines,def);

%Bounding_Box = 0; %Use 0 for whole image or 1 for a smaller center
    defined below
Bounding_Box_Data = str2double(Bounding_Box_Answers(1))

```

```

% Center of image , X_Center x Y_Center
%X_Center = 200 ; % pixels in the x direction for the center detection
%Y_Center =200; % pixels in the y direction for the center detection
X_Box_Data = str2double(Bounding_Box_Answers(2))
Y_Box_Data = str2double(Bounding_Box_Answers(3))

Smoothing = str2double(Bounding_Box_Answers(4))
Smoothing_Value = [str2double(Bounding_Box_Answers(5)) str2double(
    Bounding_Box_Answers(5))]

for i= Bubbles %Bubbles %for loop only using the bubble number
    supplied
    % Need to import all of the bubble images for the test them average
    the
    % intensities for them them compare to over tests

    Temp_Image_Folder = sprintf('pos %d%SHSC%s',Position_Number(i),
        filesep,filesep) % getting temp folder information
    Temp_Image_Folder_List = dir([Temp_Image_Folder '*.tif' ]) % dir
        finds the files in the directory matching the attribute *.tif

```

```

if i==Bubbles(1)
Temp_Image_Filepath = [Temp_Image_Folder Temp_Image_Folder_List(
    HSC_Entrance(i)).name]; % First image of the for the first
    bubble for cropping
Temp_Image = imread(Temp_Image_Filepath);
close all
k=1
end

Ca_Bubbles(k) = Ca(i);
Re_Bubbles(k) = Re(i);
We_Bubbles(k) = We(i);
%Frames_Skip_Bubbles(i) = Frames_Skip(i);

for j=HSC_Entrance(i)+ Frames_Skip(i) : HSC_Entrance(i)+Frames_Skip(
    i)+2
    Temp_Image_Filepath = [Temp_Image_Folder Temp_Image_Folder_List
        (j).name];
    Temp_Image_1 = uint32(imread(Temp_Image_Filepath));

    %Smoothing
    if Smoothing ==1

    H = fspecial('average', Smoothing_Value);
    Temp_Image_1 = imfilter(Temp_Image_1,H);
    end

```

```

% Bounding Box
if Bounding_Box_Data ==1
    if i==Bubbles(1) & j==HSC_Entrance(i)+
        Frames_Skip(i)  %initialize the ginput
        for first bubble only
    imagesc(Temp_Image_1,[2^12.-1 2^13-1])
    colormap('gray')
    [X_Center Y_Center]= ginput(1)
    close
    X_Center_Bound = round(X_Center-X_Box_Data
        /2) :round(X_Center+X_Box_Data/2);
    Y_Center_Bound = round(X_Center-Y_Box_Data
        /2) :round(X_Center+Y_Box_Data/2);
    end
    Temp_Image_1=Temp_Image_1(X_Center_Bound,
        Y_Center_Bound); % redefine temp image
end

if j==HSC_Entrance(i)+Frames_Skip(i)  % This loop initializes
the directory and the first file to be added together
    Position_Directory_List=dir('output 3 image')
    Dir_Check = strfind(strcat(Position_Directory_List.name),
        sprintf('pos %d', Position_Number(i)))
    if isempty(Dir_Check) == 1,mkdir(sprintf('output 3 image%
        spos %d', filesep, Position_Number(i)));end

Temp_Image_2 = Temp_Image_1;

```

```

else

    Temp_Image_2=imadd(Temp_Image_2,Temp_Image_1);
    end

% Saving Loop
if Bounding_Box_Data==1 % changing filename for indicating
    box
    Save_Path = sprintf('output 3 image%spos %d%sbox-%s',filesep
        ,Position_Number(i),filesep,Temp_Image_Folder_List(j).
        name)
        imwrite(uint16(Temp_Image_1),Save_Path,'tiff')
elseif Smoothing==1
    Save_Path = sprintf('output 3 image%spos %d%smooth-%s',
        filesep,Position_Number(i),filesep,
        Temp_Image_Folder_List(j).name)
        imwrite(uint16(Temp_Image_1),Save_Path,'tiff')
elseif Smoothing==1 && Bounding_Box_Data==1
    Save_Path = sprintf('output 3 image%spos %d%smoothbox-%s',
        filesep,Position_Number(i),filesep,
        Temp_Image_Folder_List(j).name)
        imwrite(uint16(Temp_Image_1),Save_Path,'tiff')
else
    Save_Path = sprintf('output 3 image%spos %d%s%s',filesep,
        Position_Number(i),filesep,Temp_Image_Folder_List(j).
        name)
    copyfile(Temp_Image_Filepath,Save_Path)
end
end

```



```

Temp_Image_Final = uint16(Temp_Image_2./uint32(3));
% Temp_Image_Final_Crop = imcrop(Temp_Image_Final,Crop_Rect);

Image_Intensity(k) = mean(mean(Temp_Image_Final));
Z_Axis_Location(k) = Positions(Position_Number(i),2);
k=k+1
end

% loop for legend
for i=1:length(Bubbles)
Intensity_Legend{i,1} = sprintf('# %d: Position %d, Bubble %d',i,
    Position_Number(i), Bubble_Number(i))
end

%Bubble_Number = double(Bubble_Number);
j=1
figure
hold on
% for i=1:length(Bubbles) %Plotting in a loop for easier viewing
%
% if Bubble_Number(Bubbles(i))==1
% cc(j) = 'r';
% ss(j) = '+';
% elseif Bubble_Number(Bubbles(i))==2
% cc(j) = 'g';
% ss(j) = 'o';

```



```

    Ca_Avg = mean(Ca_Bubbles);
    Ca_Min = min(Ca_Bubbles);
    Ca_Max = max(Ca_Bubbles);
    Bretherton_Film_Thickness = R*0.643*(3*Ca_Avg)^(2/3) %Bretherton
        model film thickenss
    Re_Avg = mean(Re_Bubbles);
    We_Avg = mean(We_Bubbles);

    %legend(Test_Number_Legend')
    xlabel('Location (\mu m)')
    ylabel('Intensity')
    title(sprintf('Location vs. Intensity Ca = %d',Ca_Avg))

    %% Data Saving

    %Save Name
    if Bounding_Box_Data ==0
        Save_Name_Data = sprintf('%stest %d - Ca = %s',Processed_Directory,
            Test_Number(1),Ca_Avg)
    else
        Save_Name_Data = sprintf('%sBox-test %d - Ca = %s',
            Processed_Directory,Test_Number(1),Ca_Avg)
    end

```

```

fid = fopen(sprintf('%s.txt', Save_Name_Data), 'w');
fprintf(fid, 'Avg Ca\t\tMin Ca\t\tMax Ca\t\tBretherton Film Thickness
\tAvg Re\t\tAvg We\t\tWall Location (um)\t\tBubbles\r\n');
fprintf(fid, '%e\t%e\t%e\t%e\t\t\t%e\t%e\t%e\t\t\t%e', Ca_Avg, Ca_Min,
Ca_Max, Bretherton_Film_Thickness, Re_Avg, We_Avg,
Z_Axis_Location_Cal, Bubbles);
fclose(fid);

disp(['Bretherton Film (m) = ' num2str(Bretherton_Film_Thickness)])

save(sprintf('%s.mat', Save_Name_Data))
print(gcf, '-depsc2', sprintf('%s.eps', Save_Name_Data)) %Save as an eps
saveas(gcf, sprintf('%s.fig', Save_Name_Data)) % save as a fig
print(gcf, '-dpdf', sprintf('%s.pdf', Save_Name_Data)) %Save as an eps

%% Selecting Data
figure;
f_selection = plot(Z_Axis_Location, Image_Intensity)

[X_Selection Y_Selection] = ginput(2)

X_Selection_Min = floor(min(X_Selection*10))/10; % Round to tenth
decimal
X_Selection_Max = ceil(max(X_Selection*10))/10;

```

```

Y_Selection_Min = floor(min(Y_Selection*10))/10;
Y_Selection_Max = ceil(max(Y_Selection*10))/10;

Z_Axis_Location_Selection = Z_Axis_Location(Z_Axis_Location>=
    X_Selection_Min&Z_Axis_Location<=X_Selection_Max);
Image_Intensity_Selection = Image_Intensity(Z_Axis_Location>=
    X_Selection_Min&Z_Axis_Location<=X_Selection_Max);

Image_Intensity_Selection_Normal = Image_Intensity_Selection./max(
    Image_Intensity_Selection);

save(sprintf('%s_Selection.mat', Save_Name_Data))

%%

clear Temp_Image Temp_Image_Final Temp_Image_Crop

```

## B.5 Intensity Check

```
%% checking the intensity of a channel reflection to determine where the  
    box should  
  
% Using 8-28-13 test 1    location 11.6 pos 15    using images 735  
% importing to  
  
clc, clear, close('all')  
  
cd('F:\Joe H\Thin Film Measurement\Intensity Check')  
  
  
im_1 = imread('pos 15000735.tif');  
  
  
figure;  
f_1 = imshow(im_1, [4 2^14-1])  
  
  
im_reduced = im2double(im_1(1:10:end, 1:10:end));  
%% 3d Plotting  
  
%Meshing  
[x y]= size(im_reduced);  
X = 1:x;  
Y = 1:y;  
[xx,yy]=meshgrid(Y,X);
```

```

figure; f_mesh=mesh(xx,yy,im_reduced);
colorbar

%%%%
im_segmented = (im_reduced>.65*max(max(im_reduced))).*im_reduced;

figure; f_segmented = mesh(xx,yy,im_segmented);

% smoothed
% myfilter = fspecial('gaussian',[3 3], 0.5);
% im_smoothed = imfilter(im_reduced,myfilter,'replicate');

H = fspecial('average', [7 7]);

im_smoothed = imfilter(im_reduced,H);
figure
figure; f_smoothed = mesh(xx,yy,im_smoothed);

im_segmented_smoothed = (im_smoothed>.85.*max(max(im_smoothed))).*
    im_smoothed;

figure; f_segmented_smoothed = mesh(xx,yy,im_segmented_smoothed);
figure; f_segmented_smoothed_surface = surface(xx,yy,
    im_segmented_smoothed);

```

**pause**

```
[xbound ybound] = ginput(2)
```

```
deltax = (xbound(2)-xbound(1))*10
```

```
deltay = (ybound(1)-ybound(2))*10
```



## B.6 RS-232 Focus Control

```
% Rs-232 Control
% Joseph Hernandez
% 10-20-11

clear all, clc, close all, fclose('all')

Date = '09-18-13' ;
Test = '1' ;

%Scan setup      %% for the waveplate it is 300 um plusminus 30 nm

Delta_Z = 30000
Z_Step = '150' ; % 1000 is equal to 1 micron, check this, if comp is 0
            and

Steps = round(Delta_Z /str2num(Z_Step))

% Steps = 80;

fprintf('Current Directory is \n %s,\n is this the right directory for
        the data y/n', eval('cd')) % confocal data
directorycheck=input('[n]', 's') ;

if isempty(directorycheck),      directorycheck = 'n'; end
```

```

if directorycheck == 'n', Directory_Name = uigetdir; cd(sprintf('%s',
    ...
    Directory_Name)); else Directory_Name=pwd; end

Directory = pwd;
Raw_Directory = [ Directory filesep 'Raw' filesep Date filesep 'test'
    Test filesep] ;
Processed_Directory = [ Directory filesep 'Processed' filesep Date
    filesep 'test' Test filesep] ;

%Check if folders exist if not create them

if exist([Directory filesep 'Raw' filesep Date filesep]) ~=7 %Raw data
    date folder
    mkdir( [Directory filesep 'Raw' filesep Date filesep])
end
if exist([Directory filesep 'Processed' filesep Date filesep]) ~=7; %
    Processed data date folder
    mkdir( [Directory filesep 'Processed' filesep Date filesep])
end
if exist(Raw_Directory)~=7;
mkdir(Raw_Directory)
end
if exist(Processed_Directory)~=7;
mkdir(Processed_Directory)
end

%%
% Serial port Setup

```

```

Port = 'COM1' ;
Baud = 9600 ;
Terminator = 'CR' ;

TTL_OUT = '0' ;

% Open the serial port
s = serial(Port);
set(s, 'BaudRate', Baud)
set(s, 'Terminator', Terminator)
set(s, 'Terminator', {'CR', 'CR'});

fopen(s)

%Check Comp 0 is required for macro and the appropriate scale
Comp = query(s, 'comp')

if strcmp(Comp, '1')
fprintf(s, 'comp 0')
end

query(s, sprintf('ssz 5'))
query(s, sprintf('C %s', Z_Step))
query(s, sprintf('saz 25'))
query(s, sprintf('smz 25'))
%% Capture Loop

```

```

j=1;
Position = zeros(1,Steps);
for i = 1:Steps
    if i ==1
        % Zero = query(s, 'z');
        flushoutput(s)
        flushinput(s)

        end

tmp = query(s, 'Pz')
    Position(i) = str2num(tmp);
    pause(.1)
    flushoutput(s)
    flushinput(s)
    pause(0.1)

% while j<=10

%Take the image, triggering the Pulnix camera with the ttl ports,
TTLON = query(s,sprintf('ttl %s 1',TTL_OUT)) ; %Turn the ttl port on
pause(.3)
TTL OFF = query(s,sprintf('ttl %s 0',TTL_OUT)) ; %Turn the ttl port
    off
    %pause(.3)
    % pause(2)
    % j=j+1
%end
%j=1

```

```

Down = query(s, 'd') ;    % D step down but for the inverted the D is
    up

pause(2)
i
end
fclose(s)

%%
tmp1 = sprintf('%stest%s.txt', Raw_Directory, Test)
dlmwrite(sprintf('%stest%s.txt', Raw_Directory, Test), Position, 'delimiter'
    , ', ')
save(sprintf('%stest%s.mat', Raw_Directory))
%csvwrite(tmp1, Position)

% fclose(s)

[s, fs] = wavread('C:\WINDOWS\Media\Windows XP Startup.wav');
sound(s, fs);

```

## B.7 Particle Tracking

```
%%% New PTV Code adaptation of previous ptv code made into functions for
%%% clarification.
%%% Joseph Hernandez
%%% 06-07-11

%set(0, 'DefaultFigureWindowStyle', 'docked') % set for docked images

set(0, 'DefaultFigurePaperOrient', 'landscape')

clear , clc, close all

%% Initialize

Data_Path Data_Directory = uigetdir(pwd, sprintf('Pick Data Directory'))
    );   %%% Fix

% fprintf('Current Directory is \n %s, \n is this the right directory for
    the data y/n', eval('cd'))
% directorycheck=input('[n]', 's') ;
%
% if isempty(directorycheck),      directorycheck = 'n'; end
% if directorycheck == 'n', Directory_Name = uigetdir; cd(sprintf('%s',
    ...
```

```

%     Directory_Name)); else Directory_Name=pwd; end

%% Read Config

%configread %Function configread.m no inputs, global outputs

%% Defining Paths
Absolute_Path=Directory_Name(1:end-(4+length(Directory))); %removing
the image directory and making the absolute path by subtracting the
raw/ (4) and the length of the of the directory name
Processed_Directory=sprintf('%sProcessed/', Absolute_Path);
Raw_Directory=sprintf('%sRaw/', Absolute_Path);
Processed_Directory_List=dir(Processed_Directory);
Dir_Check = strfind(strcat(Processed_Directory_List.name), Directory
);
if isempty(Dir_Check) == 1, mkdir(sprintf('../..../Processed/%s',
Directory));end

%% Image Informations
[imageinfo x_orig y_orig bitdepth color]=imageinformation(First_Image);
%Function imageinformation.m inputs from the workspace and outputs
image information

Directory

%% Cropping Files

```

```

cropping(File_Format,Absolute_Path ,Processed_Directory,Raw_Directory,
    Directory)

% USING THE IMAGES IN THE PROCESSED FOLDER FROM HERE ON OUT BUT KEEPING
    THE
% CONFIG FILE IN THE RAW FOLDER FOR NOW.  USE COPYFILE TO COPY IT OVER
    IF
% NEEDED

%% Removing bad images
Working_Directory = sprintf('%s%s/',Processed_Directory,Directory);
Image_List = dir(sprintf('%s*.%s',Working_Directory,File_Format));
Image_List_Names = vertcat(Image_List.name);
Image_List_Full_Path = strcat({sprintf('%s',Working_Directory)},
    Image_List_Names);
Time = 0:1:(length(Image_List_Full_Path)-1);
% remove='b';
% while remove ~= 'n' && 'y'
%     clear remove
% remove=input('Do you want to check for bad images [n]','s');
% if isempty(remove), remove=('n');end
% end
%
%
% rms=zeros((length(Image_List_Names)-1),1);
% for i=1:(length(Image_List_Names)-1)
%     im1=imread(Image_List_Names(i,:));
%     im2=imread(Image_List_Names(i+1,:));

```



```

%   im2im1=double(im2)-double(im1);
%   [m n]=size(im2im1);
%   rms(i)=sqrt(sum((im2(:) - im1(:)).^2)) / sqrt(sum(im1(:).^2)); %
from http://www.mathworks.com/matlabcentral/newsreader/view_thread
/243138
%   %'A primer on wavelets and their scientific applications' by James
S Walker (2nd edition, pp 141-144).
%   if i==1, rmscheck=rms(1) ;end
%   if rms(i)>1.4*rmscheck
%       % delete(sprintf('%s%s',Working_Directory,Image_List_Names(i
+1,:))
%       % break
%
%   end
%
% end
%
%% Graythresholding Level

graytmp=imread(sprintf('%s',Image_List_Full_Path{1}));

[level graytmp]= thresh_tool(graytmp);

bitdepth_expanded=2^bitdepth-1; %expands the bitdepth for the im2bw
calc
level_normalized=level/bitdepth_expanded;

```

```

%% Starting the PTV tracking

th = max(max(graytmp))/3; %from old code

% th: the minimum brightness of a pixel that might be local maxima.
% (NOTE: Make it big and the code runs faster
% but you might miss some particles. Make it small and you'll get
% everything and it'll be slow.)
clear graytmp

sz_1 = 7;
% sz: if your data's noisy, (e.g. a single particle has multiple local
% maxima), then set this optional keyword to a value slightly larger
% than the diameter of your blob. if
% multiple peaks are found withing a radius of sz/2 then the code will
% keep
% only the brightest. Also gets rid of all peaks within sz of boundary

for i=1:length(Image_List_Full_Path)
tmp=imread(sprintf('%s',Image_List_Full_Path{i}));
graytmp=im2bw(tmp,level_normalized);
tmp_pkfnd=pkfnd(double(graytmp),th,sz_1);
%eval(['pk_',num2str(i) '=tmp_pkfnd;']);
pk(i) = {tmp_pkfnd};

end

```

```

fprintf('image peaks found \n')

%% Centroid Finding
%add if statement to go interactive for the first image and reevaluate
    or
%maybe if from 2:end

for i = 1:length(Image_List_Full_Path)
    %mx=eval(['pk_',num2str(i)]) ;           % mx: locations of local maxima to
        pixel-level accuracy from pkfnd.m
    mx = pk{i};
    sz_2 =25;
    % sz: diameter of the window over which to average to calculate the
        centroid.
    %     should be big enough
    %     to capture the whole particle but not so big that it captures
        others.
    %     if initial guess of center (from pkfnd) is far from the centroid,
        the
    %     window will need to be larger than the particle size.
    RECCOMENDED
    %     size is the long lengthscale used in bpass plus 2.

    in = 0 ; %interactive mode 1 or 0

    cn{i} = cntrd(double(graytmp),pk{i},sz_2,in);

    % making the trackable file x y t concated vertically

```

```

% ;      For the input data structure (positionlist):
% ;      (x)      (y)      (t)
% ;      pos = 3.60000      5.00000      0.00000
% ;      15.1000      22.6000      0.00000
% ;      4.10000      5.50000      1.00000
% ;      15.9000      20.7000      2.00000
% ;      6.20000      4.30000      2.00000

% cn_tmp=eval(['cn_',num2str(i)]);      % temporary cn file for position
matrix
%time_tmp=ones(length(eval(['cn_',num2str(i)])),1) * Time(i) ;      %
producing the time step matrix to add to the pk matrix , i need to
made an array with n number of cells of the same number, which is
equal to the time step
Time_Cn{i}=ones(length(cn{i}),1)*Time(i);
%poslist_tmp=horzcat(cn_tmp(:,1),cn_tmp(:,2),time_tmp) ;      %
simple matrix operation that adds a vector on horizontally
poslist{i}=horzcat(cn{i}(:,1),cn{i}(:,2),Time_Cn{i});

% horzcat(eval(['cn_',num2str(i)](:,1)))

%vertical catanate for total position list
if i==1
poslist_total=poslist{i};
else
poslist_total=vertcat(poslist_total,poslist{i});
end

```

```

end
poslist_total(any(isnan(poslist_total),2),:)=[] % removing missing
        number rows, NaN is the culprit taken from 'User Guide/Data Analysys
        /Missing Data'
fprintf('position matrix found')

%% Track
max_dist=4 ; %maxdist is the maximum distance that a
        particle can travel in px, could be input by paramete

% ; param.mem: this is the number of time steps that a particle
        can be
% ; 'lost' and then recovered again. If the particle
        reappears
% ; after this number of frames has elapsed, it will be
% ; tracked as a new particle. The default setting is zero.
% ; this is useful if particles occasionally 'drop out' of
% ; the data.
% ; param.dim: if the user would like to unscramble non-
        coordinate data
% ; for the particles (e.g. apparent radius of gyration for
% ; the particle images), then positionlist should
% ; contain the position data in positionlist(0:param.dim
        -1,*)
% ; and the extra data in positionlist(param.dim:d-1,*). It
        is then
% ; necessary poslist_totalto set dim equal to the
        dimensionality of the

```

```

% ;          coordinate data to so that the track knows to ignore the
% ;          non-coordinate data in the construction of the
% ;          trajectories. The default value is two.
% ;          param.good: set this keyword to eliminate all trajectories
with
% ;          fewer than param.good valid positions. This is useful
% ;          for eliminating very short, mostly 'lost' trajectories
% ;          due to blinking 'noise' particles in the data stream.
% ;          param.quiet: set this keyword to 1 if you don't want any
text

%default values
% memory_b=0; % if mem is not needed set to zero
% goodenough = 0; % if goodenough is not wanted set to zero
% dim = dd - 1;
% quiet=0;

param.mem = 1 ;
param.good = 0 ;
param.dim = 2; % default 'dd - 1' so dd = length(xyzs(1,:)); so
length(poslist_final(1,:)) = 3 so dd-1 = 2
param.quiet = 0;

trck=track(poslist_total,max_dist); %Tracking with the georgetown
algorithm

```

```

%% Plotting Scales
% x location 1st column
% y location 2nd column
% time scale is in 3rd column
% point numbers are in the 4th column,
%quiver(x,y,u,v)
%using quiver, plots at points x,y with magnitude u,v

for i = 1:length(Image_List_Full_Path)
if i==1
    figure
    hold on
end
    tmp=trck(find(trck(:,4)==i),:);    % finding the particle positions
        for vector plotting
for j=1:length(tmp(:,1))-1
    x_tmp=tmp(j,1);
    y_tmp=tmp(j,2);
    u_tmp=(tmp(j+1,1)-tmp(j,1))/(tmp(j+1,3)-tmp(j,3));
    v_tmp=(tmp(j+1,2)-tmp(j,2))/(tmp(j+1,3)-tmp(j,3));
lh=quiver(x_tmp,y_tmp,u_tmp,v_tmp);
    set(lh,'linewidth',2);
        set(lh,'color',[0,0,0]);
end
end
%    set(lh,'linewidth',4);
%    set(lh,'color',[1,0,0]);

```

```

Processed_Image_Info=imfinfo(sprintf('%s',Image_List_Full_Path{1}));
X_Processed=Processed_Image_Info.Width;
Y_Processed=Processed_Image_Info.Height;
axis([1 X_Processed 1 Y_Processed])
hold off
q=get(0, 'Handle');
save(sprintf('%s/%s.mat',Working_Directory,Directory), 'poslist_total', '
    trck', 'q');
print('-depsc2', '-loose', sprintf('%s/%s.eps',Working_Directory,Directory
    ));
%save(sprintf('~\Documents\Research\Confocal\Confocal Data\Processed\s/
    test\s/%s.mat',Date,Test,savename), 'poslist', 'trck', 'q', '-append');
    % append for all data

```



## B.8 RS-232 PTV

```
% Rs-232 Control
% Joseph Hernandez
% 10-20-11

clear all, clc, close all, fclose('all')

Date = '03-07-12' ;
Test = '1' ;

% negative x is the positive flow because of references
Travel_Wet = 10000; %Distance to travel for prewetting, .01 microns
Travel_Data = 4000; % distance to travel for data collection
Stage_Speed = 1; %SMS setting

fprintf('Current Directory is \n %s,\n is this the right directory for
    the data y/n', eval('cd')) % confocal data
directorycheck=input('[n]', 's') ;

if isempty(directorycheck), directorycheck = 'n'; end
if directorycheck == 'n', Directory_Name = uigetdir; cd(sprintf('%s',
    ...
    Directory_Name)); else Directory_Name=pwd; end

Directory = pwd;
```

```

Raw_Directory = [ Directory filesep 'Raw' filesep Date filesep 'test'
    Test filesep] ;
Processed_Directory = [ Directory filesep 'Processed' filesep Date
    filesep 'test' Test filesep] ;

%Check if folders exist if not create them

if exist([Directory filesep 'Raw' filesep Date filesep]) ~=7 %Raw data
    date folder
    mkdir( [Directory filesep 'Raw' filesep Date filesep])
end
if exist([Directory filesep 'Processed' filesep Date filesep]) ~=7; %
    Processed data date folder
    mkdir( [Directory filesep 'Processed' filesep Date filesep])
end
if exist(Raw_Directory)~=7;
mkdir(Raw_Directory)
end
if exist(Processed_Directory)~=7;
mkdir(Processed_Directory)
end

%%
% Serial port Setup
Port = 'COM1' ;
Baud = 9600 ;
Terminator = 'CR' ;

TTL_OUT = '0' ;

```

```

% Open the serial port
s = serial(Port);
set(s, 'BaudRate', Baud)
set(s, 'Terminator', Terminator)
set(s, 'Terminator', {'CR', 'CR'});

fopen(s)

%Check Comp 0 is required for macro and the appropriate scale
Comp = query(s, 'comp')

if strcmp(Comp, '1 ')
fprintf(s, 'comp 0')
end

% query(s, sprintf('ssz 5', Z_Step))
% query(s, sprintf('C %s', Z_Step))
query(s, sprintf('saz 25'))
%query(s, sprintf('smz 25', Z_Step))
query(s, sprintf('sms %1.0f', Stage_Speed ))

%% Capture PTV

query(s, 'z')

```

```

%try wrting a macro to it
query(s, 'macro')

%query(s, sprintf('g, -%1.0f, 0', Travel_Wet)) % prewet
%query(s, 'm') %back to zero
query(s, sprintf('g, %1.0f, 0', Travel_Data))
query(s, sprintf('ttl %s 1', TTL_OUT)) ; %Turn the ttl port on
query(s, 'm') %back to zero
pause(1)
query(s, sprintf('ttl %s 0', TTL_OUT)) ; %Turn the ttl port off
query(s, 'macro')

flushinput(s)

fclose(s)
instrreset

%%
%tmp1 = sprintf('%stest%s.txt', Raw_Directory, Test)
%dlmwrite(sprintf('%stest%s.txt', Raw_Directory, Test),, 'delimiter', ',')
save(sprintf('%stest%s.mat', Raw_Directory))
%csvwrite(tmp1, Position)

fclose(s)

```